COMPUTATIONAL ANALYSIS OF GAP EFFECTS ON THE SURFACE OF REENTRY SPACE VEHICLES

Luis Thiago Lucci Correa Paolicchi

Master Thesis at Post-Graduation Course in Space Engineering and Technology/Combustion and Propulsion, advised by Dr. Wilson Fernando Nogueira Santos, approved in December 23, 2010

URL of the original document:
<http://urlib.net/ 8JMKD3MGP7W/394K2HS >

INPE

São José dos Campos

2011

COMPUTATIONAL ANALYSIS OF GAP EFFECTS ON THE SURFACE OF REENTRY SPACE VEHICLES

Luis Thiago Lucci Correa Paolicchi

Master Thesis at Post-Graduation Course in Space Engineering and Technology/Combustion and Propulsion, advised by Dr. Wilson Fernando Nogueira Santos, approved in December 23, 2010

URL of the original document:
<http://urlib.net/ 8JMKD3MGP7W/394K2HS >

INPE

São José dos Campos

2011

Aprovado (a)   pela Banca Examinadora
em cumprimento ao requisito exigido para
obtenção do Título de *Mestre*   em

Engenharia e Tecnologia
Espaciais/Combustão e Propulsão

Dr.   Wilson Fernando Nogueira dos
Santos

_____
Presidente / Orientador(a) / INPE / Cachoeira Paulista - SP

Dr.   Fernando Fachini Filho

_____
Membro da Banca / INPE / Cachoeira Paulista - SP

Dr.   Helcio Francisco Villa Nova

_____
Convidado(a) / UFABC / Santo André - SP

Aluno (a):   *Luis Thiago Lucci Correa Paolicchi*

São José dos Campos, 23 de dezembro de 2010

"I have no concisely idea about what God is,
 what I know is that the Universe seems too
 much perfect to be work by chance"

Luis Thiago Lucci Corrêa Paolicchi

To my family, Luís André, Maria Célia and Michelle.

ABSTRACT

A computational investigation was performed with the purpose to examine the impact of gaps on the flowfield structure and aerodynamic properties on the surface of reentry space vehicles, under conditions of rarefied hypersonic flow. The calculations were performed with a robust computer code that takes into account for the effects of thermodynamic non-equilibrium. A detailed description of the impact on the flowfield properties - velocity, density, pressure and temperature - as well as on the aerodynamic surface quantities - number flux, heat transfer, pressure and skin friction - is presented at the vicinity of the gaps due to variations in the length-to-depth (L/H) ratio. For the conditions investigated in the present account, the analysis showed that the recirculation region inside the gaps for transition flow regime differs from that for the continuum flow regime, where the number of vortices inside the gap is not a function of the H/L ratio. In contrast, for the aerodynamic surface quantities acting on the gap surface, it was found that the pressure and heat loads presented the maximum values along the gaps downstream faces, more precisely at the shoulder of the gaps. In addition, these loads are much larger than those attained in a smooth surface.

x

ANÁLISE COMPUTACIONAL DO EFEITO DE FILETES NA SUPERFÍCIE DE VEÍCULOS ESPACIAIS NA REENTRADA

RESUMO

Uma investigação computacional foi realizada com o objetivo de examinar o impacto de descontinuidades na estrutura do escoamento e propriedades aerodinâmicas na superfície de veículos espaciais na reentrada, em condições de escoamento hipersônico rarefeito. Os cálculos foram realizados com um código computacional robusto que leva em conta os efeitos de não equilíbrio termodinâmico. Uma descrição detalhada do impacto sobre a estrutura do escoamento - velocidade, massa específica, pressão e temperatura -, bem como sobre as propriedades aerodinâmicas – fluxo molecular, transferência de calor, pressão e atrito - é apresentado na proximidade dos filetes devido a variações na razão do comprimento pela profundidade (L/H). Para as condições investigadas no presente trabalho, a análise mostrou que a região de recirculação no interior do filete para o regime de transição difere daquele para o regime do contínuo, onde o número de vórtices dentro do filete não é uma função da relação (H/L) . Em contraste, para as propriedades aerodinâmicas que atuam sobre a superfície do filete, verificou-se que as cargas de pressão e calor apresentaram os valores máximos ao longo das faces a jusante do filete, mais precisamente no ombro dos filetes. Além disso, essas cargas são muito maiores do que aqueles obtidas em uma superfície lisa livre de descontinuidade.

LIST OF FIGURES

LIST OF TABLE

LIST OF SYMBOLS

a	speed of sound, *m/s*
C_f	skin friction coefficient, $\tau_w / (\frac{1}{2}\rho_\infty U_\infty^2)$
C_h	heat transfer coefficient, $q_w / (\frac{1}{2}\rho_\infty U_\infty^3)$
C_p	pressure coefficient, $p_w - p_\infty / (\frac{1}{2}\rho_\infty U_\infty^2)$
$\boldsymbol{c}$	molecular velocity vector, *m/s*
c_r	relative speed, *m/s*
d	molecular diameter, *m*
e	specific energy, *J/kg*
F_N	simulated molecules, -
F_n	intermolecular force, *N*
f	fraction of molecules reflected diffusely, -
H	gap depth, *m*
Kn	Knudsen number, -
L	gap length, *m*
L	characteristic length, *m*
M	Mach number, -
m	mass, *kg*
N	number of simulated molecules, -
N_f	number flux, -
n	number density, m^{-3}
P	collision probability, -
p	pressure, N/m^2
q	heat flux, W/m^2
R	gas constant, *J/Kmol*
Re	Reynolds number, -
R_f	random function, -
T	temperature, *K*
U_∞	freestream velocity, *m/s*

u	tangential velocity, *m/s*
v	normal velocity, *m/s*
V_c	volume of the cell, *m³*
X	dimensionless length, x/λ_∞
x,y	cartesian axes in physical space
Y	dimensionless height, y/λ_∞, -
Y'_H	dimensionless height, $(y+H)/H$, -
Z	relaxation collision number, -

Greek Symbols

α	angle of attack, degree
ζ	degree of freedom, -
κ	constant in the inverse power law model, -
λ	mean free path, *m*
μ	dynamic viscosity, *kg/m.s*
ρ	density, *kg/m³*
σ	collision cross section, *m*
τ	relaxation time, *s*
τ_c	mean collision time, s
$\square$	average probability of energy exchange, dimensionless
$\dot{r}$	dr/dt, *m/s*
$\ddot{r}$	d²r/dt², *m/s²*
Δt	time step, *s*

Subscripts

d	refers to downstream surface
i	refers to incident molecule
m	refers to center of mass
O	refers to overall energy

R	refers to rotational energy
r	refers to reflected molecule
ref	reference value
T	refers to translational
u	refers to upstream surface
V	refers to vibrational energy
w	wall conditions
∞	freestream conditions

CONTENTS

1. INTRODUCTION

1.1 Motivation

Separated and/or reattached supersonic/hypersonic flows have received considerable attention in the last decades. This growing interest is intimately connected with their frequent occurrence on the surfaces of high-speed aerodynamic structures. Many problems of physical interest involve separation and/or reattachment flows, which can occur in a variety of ways. For example, the maximum lift of an airfoil is limited by the occurrence of separation. Separated regions can also occur in an overexpanded rocket nozzle, behind a blunt base, on the leeward side of an object inclined at large angle of attack, by an oblique shock wave incident on the boundary layer, etc.

An interesting class of problems involving separated and/or reattached flows arises when discontinuities or imperfections, such as protuberances, steps, notches, cavities or gaps are present on the surface of reentry hypersonic vehicles. The presence of these discontinuities or imperfections in modern aerodynamics configurations occurs as a desired or undesired design feature. As an illustrative example, the thermal protection system (TPS) of the experimental Crew Rescue Vehicle X-38 requires gaps between the TPS tiles (HINDERKS; RADESPIEL, 2006), as displayed in Figure 1.1. Gaps between the tiles are necessary in order to account for the thermal expansion of the structure to which the TPS tiles are attached. Similarly, a larger part of the TPS of the Space Shuttle Orbiter consists of reusable surface insulation tiles, as illustrated in Figure 1.2. Usually, the majority of the TPS tiles consists of silica foam with 6 x 6 inches square, with variable depth that depends on the tile location on the Orbiter. In principle, the flow is very complex in the gaps between tiles, since hot gases may flow into the gaps and cause an increase in the heating rate to the tile sidewall and the underlying aluminum structure (SCOTT; MARAIA, 1979).

1

Figure 1.1 - X-38 Nosecap
Source: Adapted from Hinderks and Radespiel (2006).

Figure 1.2 - Drawing illustrating the tile configuration of the Space shuttle Orbiter.

It is firmly established that reentry hypersonic vehicles are exposed to extreme flight conditions with heavy thermal and mechanical loads acting on the surface of the

vehicles during their mission. The mechanical loads acting on the surface of the vehicles are integrated over the entire configuration in order to define the aerodynamic forces and moments (drag, lift and pitching moment). In addition, the distribution of the thermal loads to the surface of the vehicles is part of the process to design the TPS (BERTIN; CUMMINGS, 2006). Unfortunately, the accident of the Space Shuttle Orbiter Columbia, during its reentry from orbit on February 1, 2003, has been a reminder of how severe the aerothermodynamic environment is for a vehicle traveling at hypersonic speeds. According to the final report of the Columbia Accident Investigation Board (CAIB), a piece of insulating foam produced a breach in the TPS of the leading edge of the left wing. It is believed that this small breach in the TPS provided a path for the hot gases, which reached the interior of the left wing during the severe aerothermodynamic environment in the reentry trajectory of the Columbia during its mission STS-107 (BERTIN; CUMMINGS, 2006).

Similar to the accident of the Space Shuttle Orbiter Columbia, a piece of foam insulation was released from the external tank of the Space Shuttle Endeavour during the vehicle ascent in its mission STS-118 in August 2007 (PALMER et al., 2009). The impact of the foam in the TPS tile caused a defect like a cavity, 0.076m long by 0.051 m wide, designated as damage site D-118-RPM-600_2-001, as illustrated in Figure 1.3. The photograph shown in Figure 1.3 was produced during the damage site inspection performed when the Orbiter Endeavour was docked to the International Space Station (ISS). A group of analysts, scientists at the NASA Ames and NASA Langley Research Centers, known as the Damage Assessment Team (DAT), performed computational fluid dynamic (CFD) simulations, in order to provide insight into the flow structures and flow physics in the interior of the cavity, during the STS-118 mission. Based on the detailed CFD solutions generated by the DAT, it was decided not to perform a spacewalk to repair the damage site but rather to fly Space Shuttle Endeavour back to Earth with the damage site. Fortunately, the Space Shuttle Endeavour successfully reentered the Earth`s atmosphere and landed on August 21, 2007.
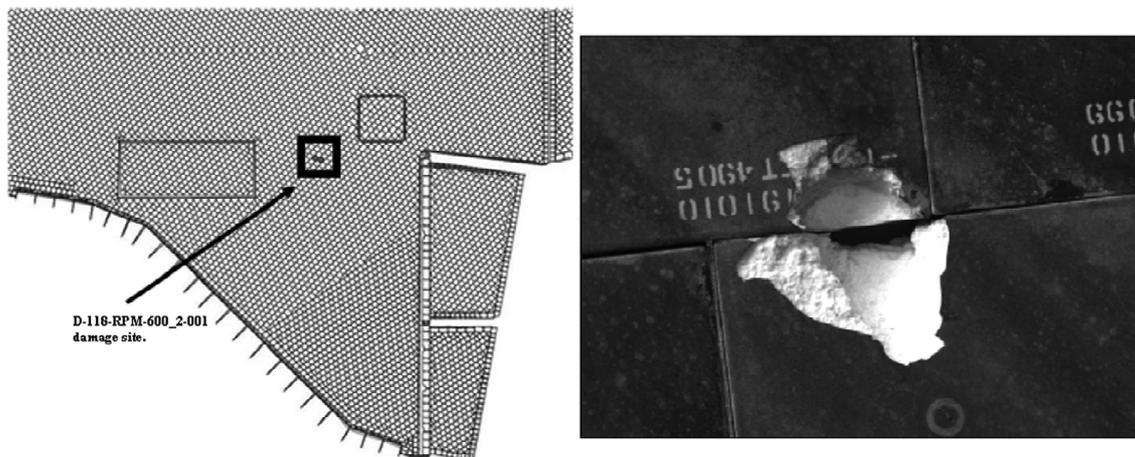
Figure 1.3 - Drawing illustrating the (a) location and (b) the on-orbiter photograph of D-118-RPM-600_2-001 damage site (adapted from Palmer et al., 2009).

These examples highlight the importance of investigation of discontinuities or imperfections on the hypersonic vehicle surface. Cavities, gaps or steps present on the surface may introduce regions of increased local heating. In this fashion, in advanced studies of hypersonic reentry vehicles, a great understanding of the factors that affect local heating rate becomes imperative, and an accurate determination of the aerodynamic and thermal loads is a necessary requirement for an optimal design of reentry vehicles.

1.2 Reentry Flow Regimes

Hypersonic flow is best defined as that regime where certain physical phenomena become progressively more important as the Mach number is increased to higher values (ANDERSON JR, 1989). Some of these flow phenomena, such as strong shock waves, viscous interactions, high temperature, or entropy layer may become important at Mach numbers less than or greater than 5. As a result, the definition of where the onset of hypersonic flow begins is an approximation.

Usually, these complex physical phenomena take place during the ascent phase of space vehicles towards their orbit and during the descent phase from their orbit to the ground.

4

The descent phase in which space vehicles enter the part of the upper atmosphere with a significant density is denoted by reentry. In this phase, space vehicles undergo not only different velocity regimes, hypersonic, supersonic and subsonic, but also different flow regimes, free molecular flow, transition and continuum. Therefore, the vehicle flight trajectories transverse a wide range of Mach, Reynolds and Knudsen numbers.

During the descent phase, important physical interactions arise between the vehicle and the environment around the space vehicle. At the highest altitudes, the interaction of the vehicle with the atmospheric air is characterized by the free molecular flow. In this regime, the molecules of the environment collide with the vehicle surface, interact with the surface and are reflected from the surface. However, collisions of reflected molecules with incoming molecules from the freestream are not frequently in this flow regime. As a result, they are ignored.

As the space vehicle enters a little deeper into the dense atmosphere, the mean free path between incoming atmosphere molecules decreases, and collisions between molecules reflected from the vehicle surface and the molecules incoming from the freestream can no longer be ignored. As a result, the flow in this condition defines the transition flow regime, i.e., transition between the collisionless flow regime and the continuum flow regime. In the transition flow regime, the contribution of aerodynamic forces and heat flux to the vehicle surface start increasing rapidly with decreasing altitude, causing large changes in the aerodynamic characteristic of the vehicle when compared with those observed in the free molecular flow.

As the space vehicle continues to enter into the atmosphere, it finally reaches the continuum flow regime. In this regime, the flow around the space vehicle is treated by a macroscopic model that considers the air as a continuum, and the description of the flow is made in terms of spatial and temporal variations of the primary properties, such as velocity, pressure, density and temperature.

The basic criterion that determines the flow regimes – collisionless, transition or continuum – is given by the Knudsen number as follows,

$$Kn = \frac{\lambda}{l} \tag{1.1}$$

where λ is the mean free path traveled by molecules between collisions and l is a characteristic length of the problem. A flow is defined in the continuum regime when the Knudsen number tends to zero. In this situation, molecules are considered to be so densely packed that the mean free path is insignificant compared with the flow dimensions. On the other hand, a flow is defined in the free molecular flow as the Knudsen number goes to infinity. Figure 1.4 presents the classification of flow regimes as a function of the local Knudsen number.
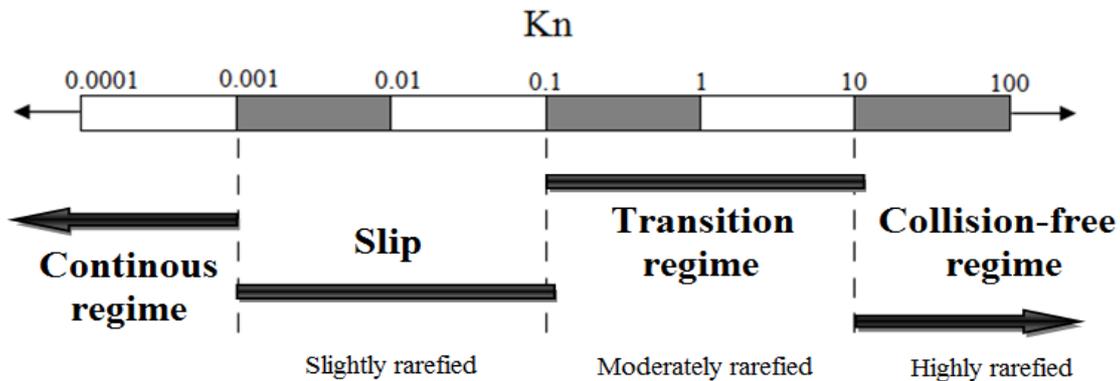
Figure 1.4 - Flow regimes as a function of the Knudsen number.

For flows around reentry space vehicles in the range from 120 to 60 Km of altitude, the molecular mean free path λ may be of the order of the dimensions related to the discontinuities or imperfections on the vehicle surfaces. In such a circumstance, the Knudsen number, which indicates the degree of flow rarefaction, may be in the range of the transition flow regime, i.e., between the continuum regime and the collisionless regime. The dimensions of the discontinuities or imperfections on the surface, the depth H and the length L for cavities or gaps are usually on the order of 3 to 6 mm (EVERHART et al., 2006; GAI S.; MILTHORPE, 1995). Therefore, as a base of

6

comparison, for 90, 80, 70, and 60 km of altitude, the molecular mean free path λ is 26.03, 4.11, 0.929, and 0.265 mm, respectively. As a result, for H (or L) of 3 mm, the global Knudsen number is the order of 8.67, 1.37, 0.31, and 0.088, for altitudes of 90, 80, 70 and 60 km, respectively. By considering H (or L) of 6 mm, the global Knudsen number is reduced by half. In this scenario, the Knudsen number is in the transitional flow regime, usually defined by the range $0.1 < Kn < 10$. In the transitional flow regime, concepts of the continuum hypothesis can not be applied and the molecular structure of the gas must be considered.

1.3   Review of Previous Work

There is nowadays a rather extensive literature – mostly, but not entirely, experimental - dealing with the aerodynamic characteristics of protuberances (MAZAHERI; WOOD, 2009), distortions (BERTRAM; WIGGS, 1963; BERTRAM et al., 1967), steps (BOGDONOFF; KEPLER, 1995; GADD, 1957; GAI; MILTHORPE, 1995; GROTOWSKY; BALLMANN, 2000; JAKUBOWSKI; LEWIS, 1973; NESTLER et al., 1969; PULLIN; HARVEY, 1977; ROM; SEGINER, 1964), cavities (CHARWAT et al., 1961a; CHARWAT et al., 1961b; EMERY et al., 1967; EVERHART, 2009; EVERHART; GREENE, 2010; EVERHART el al., 2006; HAHN, 1969; HIGDON, 1985; JACKSON et al., 2001; MORGENSTER JR; CHOKANI, 1994; NESTLER, 1982; PALMER et al., 2009; ROM; SEGINER, 1964) or gaps (BERTIN; GOODRICH, 1980; CHARBONNIER; BOERRIGTER, 1993; DUNAVANT; THROCKMORTON, 1974; HIGDON, 1985; HINDERKS; RADESPIED, 2006; HINDERKS et al., 2004; PETLEY, 1984; PITTS; MURBACH, 1982; SCOTT; MARAIA, 1979; SMITH el al., 1983; TRAINEAU, 2005). In general, these research studies have been conducted in order to understand the physical aspects of a subsonic, supersonic or hypersonic flow past to these types of surface discontinuities or imperfections. Given the larger number of papers in this area, this introduction will focus on the more limited subject of two-dimensional flows over cavities and gaps.

Charwat et al. (CHARWAT et al., 1961a; CHARWAT et al., 1961b) performed a comprehensive study of a low supersonic cavity flow, $M_\infty \sim 3$, postulated and verified the existence of an alternate emptying and filling process in the cavity. Local heat flux to the cavity floor was investigated. Their heat transfer measurements were made by steady-state technique utilizing an estimate recovery temperature.

Nestler et al. (NESTLER et al., 1969) conducted an experimental investigation on cavities and steps in a hypersonic turbulent flow. For the flow conditions investigated, they found that the pressure distributions in the cavity presented a typical behavior of closed cavity flow in the sense that the flow expands into the cavity, reattaches to the floor, and separates as it approaches the downstream corner.

Everhart et al. (EVERHART et al., 2006) investigated experimentally the effect of a pressure gradient on the local heating disturbance of rectangular cavities in a hypersonic flow conditions using a Mach 10 tunnel. This experimental study showed that for open cavities, pressure gradient have a minimal effect on the average floor augmentation. Conversely, for closed cavities, pressure gradient increased the average heating by a factor of 50% above the zero gradient conditions, which was approximately 0.3. An assessment of the maximum increasing on the end wall revealed no apparent effect for the short or open cavity. However the analysis was inconclusive for the long or closed cavity.

Based on the studies available in the current literature (EVERHART et al., 2006), the flow topology over cavities in the continuum flow regime may be generally identified by the length-to-depth (*L/H*) ratio. In this framework, for the range $1 < L/H < 10$, the cavity is defined by an open cavity; the mainstream flow does not enter the cavity directly, and the flow is stable. For $L/H > 14$, the cavity is known as closed cavity; the mainstream flow is able to enter into the cavity and to impinge on the floor, and the flow is also stable. For the range $10 < L/H < 14$, the cavity is known as transitional cavity, since the flow is unsteady and alternates between the two stable bounding

conditions. Finally, very short or deep cavity with *L/H* < 1 is known as gap. For this particular *L/H* range, the gap flow topology is usually defined by the development of a column of counter-rotating vortices within the gap caused by the main stream flow, where the number of vortices is approximately given by *H/L*. In addition, alternating hot spots are developed in the gap when the vortices directionally align and impinge on the gap sidewall. For completeness, Figure 1.5 illustrates the flow topology in a gap.
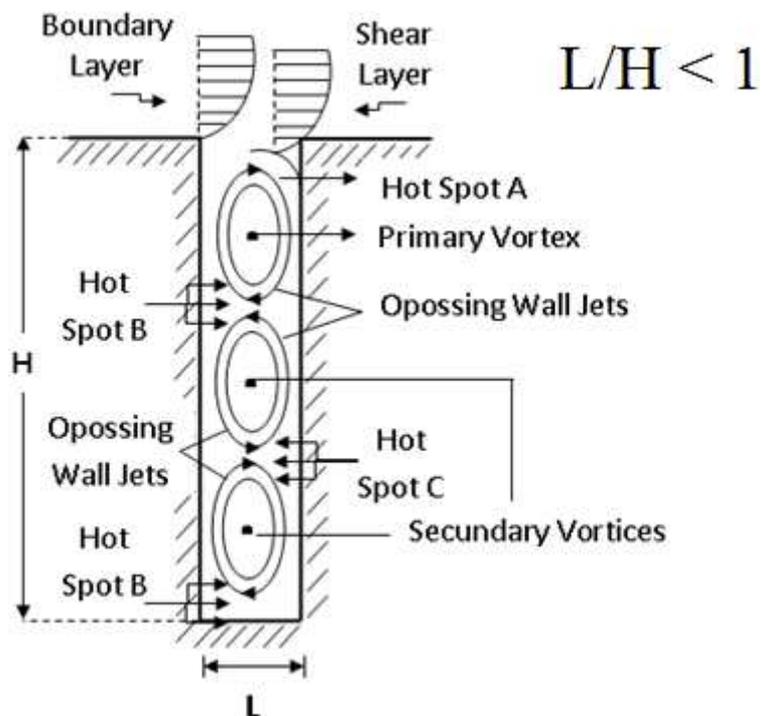
Figure 1.5 - Drawing illustrating the flowfield structure inside a gap.

Scott and Maraia (SCOTT; MARAIA, 1979) have investigated the heating rate distribution and the temperature response on the gap walls of protection tiles. The analysis showed that the hottest location measured in the gap was at 0.75 inch from the upstream transverse gap, and the heat flux distribution in the gap was not constant in time, since the convective heating rate depended on the wall temperature of the gap. In addition, they have demonstrated that the heating rate depended on the gap length.

Bertin and Goodrich (BERTIN; GOODRICH, 1980) measured heating rates by considering laminar and transitional flow (from laminar to turbulent flow) in slots (very narrow cavities) and gaps relative to shuttle tile installation. In general, the heating measurements were obtained with sparsely spaced discrete sensors that miss much of the three-dimensional nature of the surface heating profile or the important peak heating value.

Hinderks et al. (HINDERKS et al., 2004) have investigated the gap flow structure. They showed that exist a complex flow within the gap, consisting of a vortex superposed by an axial flow. The analysis showed that the heat flux transferred to the structure depends on the thermal state of the structure. Also, effects due to changes in the gap geometry caused by deformations in the gap structure demonstrated that deformations should be considered in the design analysis.

Traineau et al. (TRAINEAU, 2005) found that an increase in the angle of attack of 10 to 15 degrees for the same case studied, generated a 48% increase in pressure at the surface and 22% increase in heat transfer. They also showed that increasing the depth and length of the gaps caused a significant increase in temperature. Furthermore, studies have found that three-dimensional effects are important to the size of the vertical flow zone at the top of the gap, where the 3-D size is much smaller than that in 2-D.

1.4   Problem Definition and Scope of Current Work

The majority of the available research studies on surface discontinuities or imperfections pointed out in the previous subsection has gone into considering laminar or turbulent flow in the continuum flow regime. Nevertheless, there is little understanding of the physical aspects of a rarefied hypersonic flow past to these surface discontinuities related to the severe aerothermodynamic environment associated to a reentry space vehicle. In this fashion, the purpose of this dissertation is to investigate the impact of the surface discontinuities on the flowfield structure and on the aerodynamic

surface quantities of a hypersonic flow in the transition flow regime. In this work, the flowfield structure is defined by the distribution of the primary properties, such as velocity, density, pressure, and the kinetic temperature, adjacent to the vehicle surfaces. Aerodynamic surface quantities are identified by the heat flux, and the normal and tangential forces acting on the vehicle surface.

In the present account, surface discontinuities are modeled by gaps situated in a hypersonic flow in a sufficiently high altitude where the appropriate mean free path becomes large, as compared to the gap dimensions, for the use of continuum hypothesis but not large enough for applying free molecular concept. At high altitudes, and therefore, low density, the molecular collision rate is low and the energy exchange occurs under non-equilibrium conditions. In such a circumstance, the conventional continuum gas dynamics that are based on the concept of local equilibrium is inappropriate, and an approach based on molecular gas dynamics is required.

In order to assess the overall performance of these gaps, a parametric study related to the effects of the length-to-depth (L/H) ratio will be explored. In an attempt to assess such effects, a two-dimensional hypersonic gap flow will be investigated by employing the Direct Simulation Monte Carlo (DSMC) method.

The research behind the contributions of this work is described in detail in the remainder of this dissertation. In order to guide the reader, a breakdown of the purpose and contents of the following chapters is provided below.

Chapter 2:   In this chapter, a description of the appropriate computational method is presented. Particular emphasis is placed on the DSMC methodology, molecular model, collision model, internal degrees of freedom and boundary conditions.

Chapter 3: The computational procedure is explored in this chapter. It includes the simulation conditions, the definition of the geometry analyzed in this research as well as the important geometric parameters.

Chapter 4: This chapter outlines the procedure for the verification and validation process of the DSMC code employed in the simulations. These procedures are applied in a test case defined by a flat-plate. The DSMC code is validated with simulation of a hypersonic flow over a flat-plate and comparisons with previous experimental and numerical results.

Chapter 5: The purpose of this chapter is to present the computational results and discussion. In this chapter, the major features of the primary properties, velocity, density, pressure and kinetic temperatures, are discussed in details. Moreover, the aerodynamic surface quantities, number flux to the surface, heat transfer, pressure, and shear stress, expressed in a coefficient form, are carefully examined.

Chapter 6: The final chapter of this dissertation contains a summary of the results obtained throughout the course of this work, and the conclusions that were drawn from them. Recommendations are made regarding further computational work that should be undertaken on the topic of this dissertation.

2.   COMPUTATIONAL METHOD

2.1   Methods for Modeling Transition Flows

The study of physical phenomena in hypersonic flows has been a challenge that is directly related to the development of new aerospace technologies. Difficulties in the study of such flows are caused by problems related to the effects of gases at high temperatures, which strongly influence the forces present in the flow (pressure, shear stress), energy flux (radiative and convective heating) and mass flow (ablation). These problems become even more complex with a reduction in the flow density. Difficulties of experimental devices for hypersonic flows of high enthalpy and low density, where several physical and chemical processes are relevant, have stimulated the development of various numerical methods to simulate these flows. As a result, there are currently several numerical methods that are accurate and capable of solving problems of rarefied hypersonic flow. The choice of the appropriate method will depend on the degree of rarefaction of the flow, the characteristic length of the problem, and the presence of the real gas effects.

Flows are characterized by a variety of dimensionless quantities. For the purpose of this work, the Reynolds number, Re, the Mach number, M, and the Knudsen number, Kn, are the most important. The degree of rarefaction of a flow is usually expressed by the Knudsen number defined by Equation 1.1. Since the mean free path λ is inversely proportional to the flow density, then it should be noted that it is not density alone that determines rarefaction, but its relation to some characteristic dimension of the geometry. The conventional continuum flow assumption is valid when the overall Knudsen number tends to zero. In this flow regime, one can disregard its microscopic structure and consider only its macroscopic properties such as density, velocity or temperature. In the opposite limit, the overall Knudsen number tending to infinity, the flow regime corresponds to the free molecular flow. In this case, intermolecular collisions may be neglected and particle collisions with the body surface play the determining role. The range defined by $0.1 < Kn < 10$ is referred to as the transition

flow regime, where not only gas-surface collisions but also intermolecular collisions are important. In the transition flow regime, viscosity, heat conduction, relaxation, diffusion and chemical processes are important. The velocity distribution functions may be non-Maxwellian, thus resulting in strong thermal nonequilibrium.

In order to circumvent the problem of how to select l for large or complex systems, a local Knudsen number is used instead of that based on the overall dimension. In this way, the local Knudsen number is the ratio of the local mean free path to the scale length of any macroscopic gradient, which is given by the following expression,

$$l = \frac{\varphi}{\left|\frac{\partial \varphi}{\partial x}\right|}$$

(2.1)

where φ may be the density, velocity, pressure or temperature.

Ranges of validity of the conventional mathematical formulations as a function of the local Knudsen number are illustrated in Figure 2.1.

In the macroscopic model or continuum flow model, the general expressions of the fundamental conservation principles that govern the motion of gases are valid for all flow regimes. However, they do not form a closed set of equations. The application of the conservation equations requires additional information concerning the shear stresses and heat flux expressed in terms of the lower-order macroscopic quantities. The Euler equations for inviscid flow assume that the flow is in local thermodynamic equilibrium with the velocity distribution everywhere equal to the local Maxwellian equilibrium distribution. This is the limiting case as the Knudsen number tends to zero. The continuum flow model, expressed by the Navier-Stokes equations, may be assumed to be valid when the Knudsen number is very small in comparison with unity. In this case, the velocity distribution function departs from the Maxwellian distribution. However,

14

the departure is still sufficiently small for the Chapman-Enskog theory (CHAPMAN; COWLING, 1970) for the transport coefficients to be valid.

DISCRETE PARTICLE OR MOLECULAR MODEL	BOLTZMANN EQUATION			COLLISIONLESS BOLTZMANN EQUATION
CONTINUUM MODEL	EULER EQUATIONS	NAVIER-STOKES EQUATIONS	CONSERVATION EQUATIONS DO NOT FORM A CLOSED SET	

0 ←———   0.01   0.1   1   10   100   ———→ ∞

INVISCID LIMIT   LOCAL KNUDSEN NUMBER   FREE-MOLECULE LIMIT
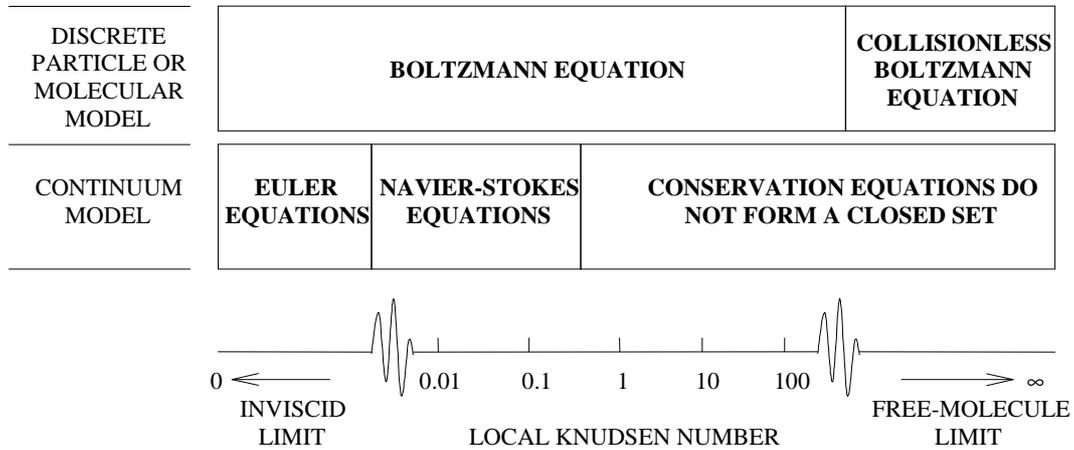
Figure 2.1 - Regimes of applicability of the conventional mathematical models as a function of the local Knudsen number.
Source: Bird (1994).

Extensive studies done by Boyd, Chen and Candler (BOYD et al., 1995) have pointed out that the departure from the Maxwellian distribution becomes important when the local Knudsen number $Kn > 0.05$, indicating that both the Chapman-Enskog theory and the Navier-Stokes equations cease to be valid. One alternative approach to this problem of the failure of the Navier-Stokes equations is to perform the Chapman-Enskog expansion to higher order to obtain the Burnett equations (BURNETT, 1936). Each level of approximation implies a different distribution function that deviates from the Maxwellian distribution. Interest in the use of Burnett equations, based on the second order of the Chapman-Enskog expansion for calculating rarefied hypersonic flows, increased in the last decades (COMEAUX et al., 1995; FISCKO; CHAPMAN, 1988; FISCKO; CHAPMAN, 1989; KEON-YOUNG Y. et al., 2001; LEE, 1994; LUMPKIN III; CHAPMAN, 1992; TANNEHILL; EISLER, 1976; VELASCO et al., 2008 ZHONG et al., 1993) However, their applications face additional difficulties related to the correct formulation of the boundary conditions and linear instability of these equations to short-wave disturbances. Furthermore, the Burnett equations increase the order of the differential equations that govern momentum and heat transport in the gas.

15

These equations are more difficult to solve numerically, and fail when the degree of rarefaction is sufficiently high. Finally, the Burnett equations can also lead to second-law impossibilities in certain situations, such as a negative dissipation function or a heat flux in an isothermal gas (COMEAUX et al., 1995). Cheng and Emanuel (CHENG; EMANUEL, 1995) present a detailed description of the use of Burnett equations for rarefied hypersonic flows.

In the microscopic model or molecular flow model, the gas is treated as a collection of molecules whose positions and velocities are individually tracked. Such a system requires solution of the Boltzmann equation (CERCIGNANI, 1988). Solutions of the Boltzmann equation are readily obtained in the free molecular limit as the Knudsen number tends to infinity. However, analytical difficulties are faced at finite Knudsen numbers. The Boltzmann equation is an integro-differential equation with the velocity distribution function as the only dependent variable. In contrast, the Navier-Stokes equations have the flow velocity and macroscopic thermodynamic properties as dependent variables. The reduction in the number of dependent variables is made at the expense of increasing the number of independent variables from those of physical space to those of phase space. In this way, an one-dimensional steady flow of a monatomic gas has an axially symmetric velocity distribution function so that the problem is three-dimensional in phase space.

Analytical solutions are generally limited to flows involving a simple molecular model, one independent macroscopic variable and small disturbances. In addition, rarefied hypersonic flow problems often involve physical effects, such as chemical reactions and thermal radiation, which have not yet been incorporated into the Boltzmann formulation. Consequently, the mathematical difficulties associated with the direct solution of the Boltzmann equation have stimulated the development of physically-based numerical methods. The Boltzmann equation may be solved numerically by the following approaches: molecular dynamics method (ALDER; WAINWRIGHT, 1957; ALDER; WAINWRIGHT, 1958), test-particle method (HAVILAND; LAVIN, 1962;

16

HAVILAND; LAVIN, 1965), direct numerical integration method (YEN, 1971; YEN, 1984) and the Direct Simulation Monte Carlo method (BIRD, 1976; BIRD, 1994). For the purpose of this dissertation only the Direct Simulation Monte Carlo method will be discussed, since it has become a powerful tool for practical calculations.

2.2   Direct Simulation Monte Carlo (DSMC) Method

The Direct Simulation Monte Carlo (DSMC) method is a particle-based numerical modeling technique pioneered by Bird (BIRD, 1976; BIRD, 1994). It is a numerical scheme for solving the nonlinear Boltzmann equation for a hard sphere. The DSMC method is based on the physical concepts of rarefied gases and on physical assumptions that form the basis for the phenomenological derivation of the Boltzmann equation. However, it is not derived from the Boltzmann equation itself. As both are based on the classical kinetic theory, the DSMC method is subject to the same restrictions as the Boltzmann equation. This requires the assumption of molecular chaos and the restriction to dilute gases. It is worthwhile to mention that a recent study (ALEXANDER; GARCIA, 1995) has demonstrated a potential extension of the DSMC method to dense gases. The relationship between the DSMC method and the Boltzmann equation was investigated by Bird (BIRD, 1970). The convergence of the DSMC method to the Boltzmann equation, as the number of molecules tends to infinity, was demonstrated by Wagner (WAGNER, 1992).

The DSMC method is now a well-established technique, and it has been recognized as an extremely powerful technique capable of predicting an almost unlimited variety of rarefied flowfields in the regimes where neither the Navier-Stokes nor the free molecular approaches are appropriate. The method has been thoroughly tested in high Knudsen number flows over the past 25 years and found to be in excellent agreement with experimental data (HARVEY, 1986; HARVEY, 2003; HARVEY; GALLIS, 2000; HOLDEN; WADHAMS, 2003; MOSS et al., 1995). The comparisons with experiments have given credibility and have been vital in gaining widespread

acceptance of the method. The potential advantages of the method that make it usable for practical scientific and engineering applications are conditioned to the comparative simplicity of transition from one-dimensional problems to two- and three-dimensional ones. Also to the possibility of incorporating complex models of gas particle interaction, including the models of internal degrees of freedom and chemical reactions without substantial complication of the computational algorithm and without significant increase in computational costs (IVANOV; GIMELSHEIN, 1998). It is also well suited for use on modern concurrent computer architectures.

DSMC models the flow as being a collection of discrete molecules, each one with a position, velocity and internal energy. The state of the molecules is stored and modified with time as the molecules move, collide and undergo boundary interactions in simulated physical space. The assumption of a dilute gas, which means that the mean molecular diameter is much less than the mean molecular spacing of molecules in the gas, allows for the molecular motion to be decoupled from the molecular collisions. Particle motions are modeled deterministically, while the collisions are treated statistically. Since it is impossible to simulate the actual number of molecules in the computational domain, a smaller number of representative molecules, referred as simulated molecules are used, each representing a large number of real molecules. DSMC simulations can vary in size from tens to thousands or millions of simulated molecules for very rarefied two-dimensional problems.

A computational cell network that represents the physical space is required for the method execution. The cell provides a convenient reference for the sampling of the macroscopic gas properties and for the choice of the potential collision pairs. The dimension of the cells must be such that changes in flow properties across each cell be small. The linear dimensions of the cells should be small in comparison with the mean free path λ in the direction of primary gradients (BIRD, 1994). Violation of cell dimension restriction leads to erroneous results, as was presented by Meiburg (MEIBURG, 1986) and pointed out by Bird (BIRD, 1987). Recent studies

18

(ALEXANDER et al., 1998; ALEXANDER et al., 2000) confirm that significant errors occur when the cell dimensions are larger than a mean free path λ. Since local mean free path λ is inversely proportional to flow density, high density flows demand more computational cells. This means that more molecules are simulated and more collisions are computed. The simulated molecules in the cell are considered as representative of the real molecules at the position of the cell, and the relative position of the molecules within the cell is ignored in the selection of a collision partner.

One additional requirement of the DSMC method is the lower limit on the number of simulated molecules per cell. As noted above, the DSMC method uses the cell system for the sampling of the macroscopic properties and for the selection of collision partners. The sampled density is used in the procedures for establishing the collision rate and it is desirable to have the number of molecules per cell as large as possible. In this way, it is advisable that each cell be populated with a minimum number of molecules, typically over twenty (CHEN; BOYD, 1996; CHEW et al., 2004; FALLAVOLLITA et al. 1993). Chen and Boyd (CHEN; BOYD, 1996) observed that the computed solution might be biased when a limited number of molecules is employed in the simulation. The deviation is inversely proportional to the number of molecules per cell. Furthermore, the corresponding number of possible collision pairs becomes much too large as the number of molecules in a unit cell is as large as possible. Therefore, in the selection of the collision partner, it is desirable to have the number of molecules per cell as small as possible. Also, the mean separation distance of the collision pair should be reduced to minimize the smearing of gradients. Bird (BIRD, 1987) solved these conflicting requirements by introducing the option of subdividing the sampling cell into an arbitrary number of subcells for the selection of collision pairs. In this way, the smallest unit of physical space is the subcell, where the collision partners are selected for the establishment of the collision rate. This procedure improves accuracy by ensuring that collisions occur only between near neighbors.

Another requirement in the DSMC method is a proper time step Δt. The paths of the

simulated molecules are traced out in physical space by decoupling motion from intermolecular collisions. The size of the time step over which decoupling occurs should be chosen to be significantly smaller than the mean time between collisions. A very small time step results in an inefficient advancement of the solution and accumulation of statistics. Most molecules will take many time steps to cross a given cell. As a result, the collision phase of each time step will involve the same group of molecules as in the previous time step since almost no molecules leave or enter the cell. Also, a large time step allows the molecules to move too far without the opportunity to participate in a collision. This again causes a smearing of the properties of the flow, resulting in yielding inaccurate or non-physical results. In this manner, the time step should be chosen such that a typical molecule moves about one fourth the cell dimension at each time step (LIU; YIN-KWEE NG, 2002). It should be remarked in this context that stability problems are completely absent in the DSMC method. Consequently, the DSMC method is not subject to a stability criterion such as the Courant-Friedrichs-Lewy condition of traditional computational fluid dynamics.

2.2.1 DSMC Methodology

The main phases related to the application of the DSMC method are illustrated in Figure 2.2. Based on this figure, the DSMC algorithm may be divided into four procedures: (1) moving of molecules, (2) indexing of molecules, (3) intermolecular collision of molecules, and (4) sampling of molecules properties.

The computational domain is initialized with a uniform equilibrium gas condition that agrees with the freestream conditions in the physical space. Density, temperature, velocity and internal energy of entering molecules generated during each time step are specified by the known boundary conditions. The velocity of a simulated molecule is assumed to be a linear combination of the thermal velocity and the freestream velocity. Boundary conditions corresponding to the desired flow are imposed at time zero. Boundary conditions should be such that a steady flow is established at a sufficient large

time, and the desired steady result is a time average of all values calculated after reaching the steady state.

After setting the position and velocity of each molecule, all the molecules are moved through distances appropriate to their velocity components and the size of the time step. Once a molecule has been moved, its location in the computational domain must be determined. This may be achieved in a number of different ways. For simple cartesian meshes, molecule destinations are quickly computed, and the new cell is computed by using indexing schemes (BIRD, 1994). For structured and unstructured grids, efficient particle tracing schemes are outlined by Dietrich (DIETRICH, 1990) and Laux (LAUX, 1997), respectively.

For more complex grids, such as hexahedral or tetrahedral, ray-tracing techniques can be used to determine the particle position (CHEW et al., 2004; NANCE et al., 1997; WILMOTH et al., 1996). After establishing the location of the molecules, appropriate action is taken if the molecules cross boundaries representing solid surface, lines or surfaces of symmetry or the outer boundary of the flow. Molecules crossing the side from the computational domain are removed from the flow. New molecules are introduced to the simulation at the outer boundaries of the computational domain for freestream boundary conditions or from within the domain from sources. Collisions with surfaces can be treated as being either fully specular, fully diffuse or some combination of the two. Modeling molecule-surface interactions requires applying the conservation laws to individual molecules instead of using the velocity distribution function. Such application allows the DSMC method to be extended to include physical effects such as chemical reactions, catalytic walls, radiation effects, three-body collisions and ionized flows without major modifications in the basic algorithm.
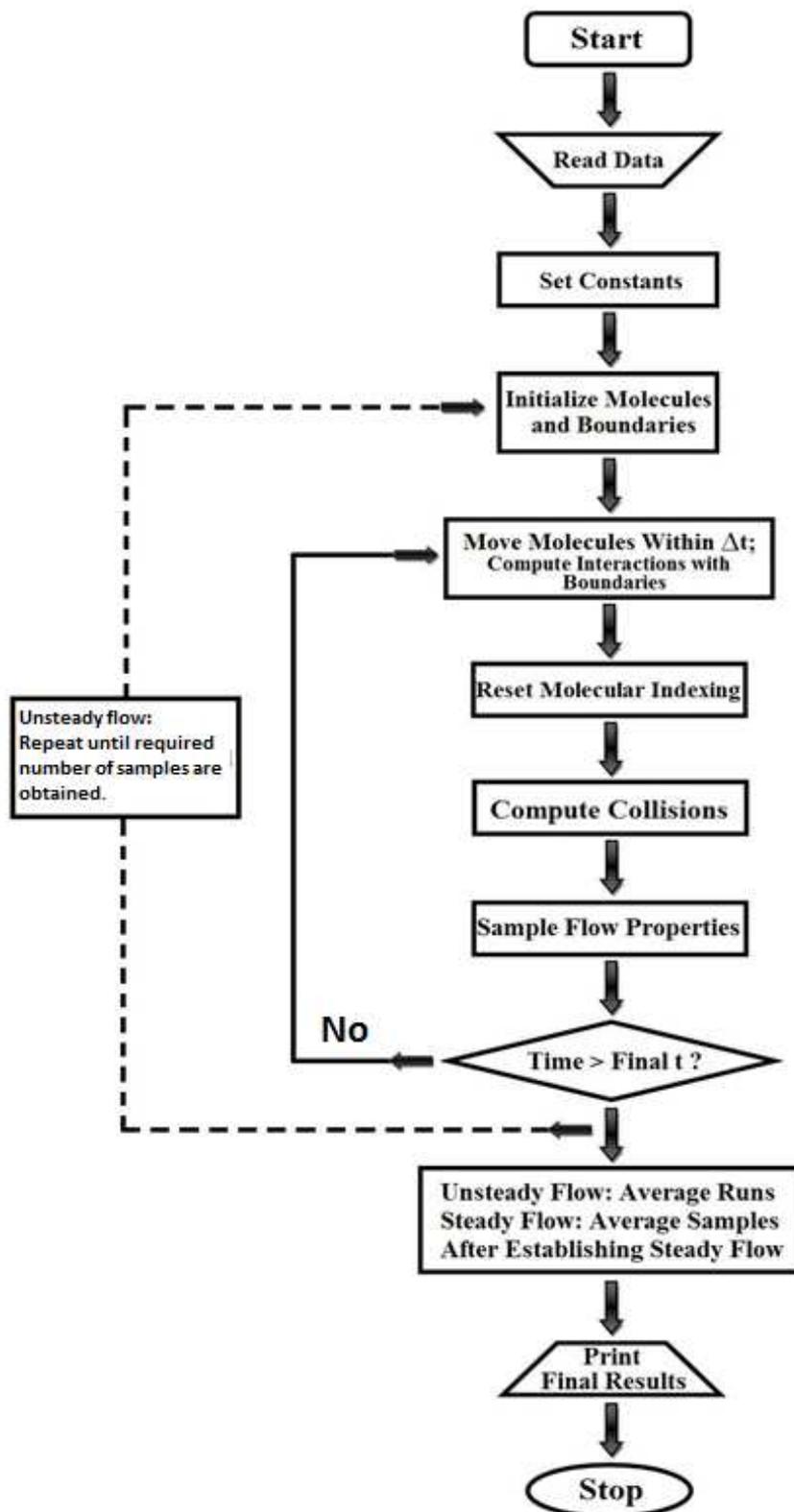
Figure 2.2 - Flowchart of DSMC method.

After determination of molecule location, they must be indexed by cell location for the two subsequent procedures: calculation of collisions and sampling the flowfield. For the selection and calculation of intermolecular collisions, each cell must be given a base index from which all other molecules in the cell can be reached through a cross-reference list. Bird (BIRD, 1976) proposed a fast indexing scheme in the original version of the DSMC algorithm. A different indexing scheme was presented by Cybyk et al. (CYBYK et al., 1995). This combines the DSMC method with the monotonic Lagrangian grid (MLG). The MLG maintains a direct correspondence between the indexing and the position of the molecules. The basic idea is to keep molecules that are close in physical space close in index space and hence close in computer memory.

In the next procedure, calculation of intermolecular collisions, molecular interactions are treated probabilistically rather than deterministically. Several different collision modeling schemes have been formulated and applied in the DSMC method. Among them, one has the time-counter (TC) technique (BIRD, 1976), Nanbu scheme (NANBU, 1986), null-collision (NC) technique (KOURA, 1986), no-time-counter (NTC) technique (BIRD, 1989) and the generalized scheme (ABE, 1993) of the no-time-counter technique. The NTC scheme proposed by Bird (BIRD, 1989) for the DSMC is the preferred model currently used along with the subcell approach discussed earlier. The collision procedure takes place on a cell-by-cell basis. The time step, the cell volume and the number of molecules resident in the cell will determine the number of candidate collision pairs that will be evaluated. The molecules are randomly selected as collision partners with the restriction that their mean separation be a fraction of the molecular mean free path. This restriction is enforced by selecting collision pairs from the list of molecules in the subcell. The DSMC method evaluates individual collision in a probabilistic basis, conserving momentum and energy.

Finally, the current description is completed by considering the sampling of the macroscopic flow properties. Macroscopic flow properties such as density, velocity, pressure and temperature are computed by appropriate averaging of the microscopic

23

state of molecules in each cell.

2.2.2 Molecular Model

The behavior of molecules during a simulated collision depends on the choice of the intermolecular force field. These fields are assumed to be spherically symmetric and the general form of the force between two neutral molecules is a function of the distance between their nuclei as shown in Figure 2.3.

Figure 2.3 - Typical intermolecular force field.
Source: Bird (1994).

According to this figure, the force is negligible when the distance between the nuclei is very large. Slightly attractive when the molecules are closed enough to the point of initiating the interaction. Finally this attractive force decays and becomes strongly repulsive as the molecules are very close one to each other.

A simple molecular model that is accurate enough for most hypersonic calculations is the inverse power potential. The intermolecular force potential is modeled as an inverse

power repulsive force by,

$$F = \frac{k}{r^\eta} \tag{2.2}$$

where r is the distance between colliding molecules and k and η are constants characterizing the molecule. The molecular force model of Equation 2.2 corresponds to a Maxwellian gas for $\eta = 5$. The hard sphere (HS) model is obtained by setting $\eta = \infty$.

In general, in any engineering simulation, millions or billions of collisions are considered. Therefore, it becomes imperative to employ a simple interaction model. In this fashion, the simplest model is that corresponding to a hard sphere. In the HS model, the collision cross section is invariant for a single gas species, the scattering angle is isotropic, and the post-collision relative velocity is sampled from a uniform solid angle distribution. However, such a model is not realistic because its total collision cross-section σ_T does not depend on the relative velocity of the colliding molecules. When the intermolecular force law is given by Equation 2.2, the Chapman-Enskog theory yields a direct relationship between the coefficient of viscosity and the gas temperature given by,

$$\mu \propto T^{(\frac{1}{2}+\frac{2}{\eta-1})} \propto T^s \tag{2.3}$$

According to Equation 2.3, the coefficient of viscosity has a fixed temperature exponent of 1 and 0.5 for Maxwellian and hard sphere models, respectively. The hard sphere and Maxwellian models are theoretical gases which can be viewed as the limiting cases for the behavior of a real gas since for almost all real gases s is generally in the range 0.6 to 0.9.

Alternative extensions of the hard sphere model have been proposed. These alternative models have proved to be very successful at reproducing the macroscopic behavior of a

25

gas yet remain computationally efficient. The first alternative model was defined as the variable hard sphere (VHS) model introduced by Bird (BIRD, 1981). The VHS molecular model treats molecules as hard spheres as far as the scattering angle distribution is concerned, i.e., all directions are equally possible for the postcollision velocity in the center-of-mass frame of reference. Furthermore, the total collision cross section σ_T is allowed to vary with the relative speed of colliding molecules as follows,

$$\frac{\sigma_T}{\sigma_{T_{ref}}} = \left(\frac{c_r^2}{c_{r_{ref}}^2}\right)^{\omega} \tag{2.4}$$

where $\omega = 2/(\eta\text{-}1)$, σ_T is the total cross section and c_r is the relative speed of the colliding molecules. The inverse power-law exponent η and the reference values are calculated by matching the viscosity of the simulated gas to that of its real counterpart.

The VHS model has been the most popular molecular model used in DSMC applications. It has been recommended (BIRD, 1994) for engineering calculations, since for most flows of interest, it has been observed that the variation in the collision cross section has a far greater influence on the structure of a flow than any variation in the molecular scattering characteristics.

Koura and Matsumoto (KOURA; MATSUMOTO, 1991; KOURA; MATSUMOTO, 1992) further improved the VHS model by introducing the Variable Soft Sphere (VSS) molecular model. The VSS model accounts for the anisotropic postcollision scattering. The second free parameter introduced by the postcollision scattering dynamics in the VSS model is chosen in order to reproduce correctly the actual viscosity and diffusion coefficients of the gases.

Hassan and Hash (HASSAN; HASH, 1993) introduced the generalized hard sphere (GHS) molecular model. The GHS model accounts for both repulsive and attractive parts of the particle-particle interaction. In this model, molecules scatter like hard

26

sphere, as was considered in the VHS model. Since the GHS model is capable of reproducing the effects of attractive portion of an interaction potential, then it is appropriate to simulate low temperature flows which are dominated by the attractive collisions (HASH et al., 1994; KUNC et al, 1995).

2.2.3 Collision Model

Several different collision-modeling schemes, which have been formulated and applied in the DSMC method, were pointed out in section 2.1.1, among them, the time-counter (TC) technique (BIRD, 1976), Nanbu scheme (NANBU, 1986), null-collision (NC) technique (KOURA, 1986), no-time-counter (NTC) technique (BIRD, 1989) and the generalized scheme (ABE, 1993) of the no-time-counter technique. For the purpose of this work, only the TC and NTC schemes will be described.

The procedures for the establishment of the correct collision rate are based on the cells, while individual collision pairs are chosen from the subcells. The time step Δt, the cell volume V_c, and the number of molecules N resident in the cell will determine the number of candidate collision pairs that will be evaluated. From kinetic theory, it may be shown that the number of collisions that must be simulated over a time step Δt is given by,

$$N_{coll} = \frac{1}{2}N\Delta t \overline{n\sigma_T c_r} \tag{2.5}$$

where n is the number density (BIRD, 1994).

In order to determine the correct total number of collisions during the time step Δt, it would be necessary to compute the average product of the relative velocity c_r and the collision cross section σ_T for all possible pairs of molecules. An algorithm that uses this approach would have a computational time proportional to N^2, where N is the total

27

number of simulated molecules. In order to overcome this difficulty, Bird (BIRD, 1976) introduced the parameter $(\sigma_T c_r)_{max}$, where the subscript max denotes the largest value for the cell, and should be updated during a binary collision if the real product $\sigma_T c_r$ were greater than $(\sigma_T c_r)_{max}$. Furthermore, the parameter $(\sigma_T c_r)_{max}$ is used to determine a real collision according to the following three operations:

(1)   Two molecules are randomly selected in the cell. The probability that these molecules collide is then given by,

$$P = \frac{\sigma_T c_r}{(\sigma_T c_r)_{max}} \qquad (2.6)$$

if this probability is larger than R_f, where R_f is a uniform random number in the range (0,1), then the pair of molecules is accepted for collision. Otherwise, a new pair is randomly selected and the procedure is repeated. This is the acceptance-rejection method described by Bird (BIRD, 1994) to select collision partners.

(2)   If the pair of molecules is accepted for collision, then a time counter for the current cell is advanced by the amount

$$\delta t = \frac{2}{N n \sigma_T c_r} \qquad (2.7)$$

(3)   A number of collisions is calculated in the cell until the sum of a number of δt's is just greater than the time step Δt. This is the time-counter (TC) scheme proposed by Bird (BIRD, 1976).

In the TC scheme, the total number of collision within the given time step Δt depends on the product $\sigma_T c_r$ related to the collision pairs, which are randomly chosen. In addition to that, it is not possible to calculate the total number of collisions at the

beginning of the iteration step. Consequently, a complete vectorization of the collision process is not possible. The difficulty in treating the TC scheme is due to the vector dependency associated with the implementation of summing several values of δt given by Equation 2.7 (BAGANOFF; MCDONALD, 1990).

In the NTC scheme, the time increment related to a randomly chosen pair of molecules is independent of the real product $\sigma_T c_r$. The parameter $(\sigma_T c_r)_{max}$ is fixed during a time iteration Δt and modified after performing all collisions. The idea of a time counter is replaced with the expression for the total number of collisions N_{coll} to be sampled in each cell by,

$$N_{coll} = \frac{1}{2} \frac{N \bar{N} F_N (\sigma_T c_r)_{max} \Delta t}{V_c} \tag{2.8}$$

where F_N is the number of real molecules represented by a single simulated molecule, N is a fluctuating quantity and $\bar{N}$ is an average value. The probability of collision for each pair sampled is again given by Equation 2.6.

The NTC scheme was introduced to alleviate difficulties found with the TC scheme in regions of highly nonequilibrium flows such as strong shock waves. The problem is related to the acceptance of an unlikely collision pair with a relatively small collision probability (one with a very small value for $\sigma_T c_r$). Under such conditions, the time increment determined by Equation 2.7 may substantially exceed the decoupled time step Δt.

2.2.4 Binary Elastic Collisions

It was pointed out in the previous subsections that DSMC is subjected to the restriction of dilute gases. For dilute gases, the intermolecular collision are considered as being

binary collisions. Also, an elastic collision is defined as one in which there is no interchange of translational and internal energy.

Given two molecules, their pre-collision velocities can be denoted by $\overrightarrow{c_1}$ and $\overrightarrow{c_2}$. Getting their physical properties and orientation of their trajectories, one can determine their post-collision velocities $\overrightarrow{c_1^*}$ and $\overrightarrow{c_2^*}$. Both momentum and energy must be kept in the collision process. In this manner, for the molecular masses denoted by m_1 and m_2 and the velocity of the centre of mass of the pair of molecules denoted by c_m, one has the following equations:

$$m_1\overrightarrow{c_1} + m_2\overrightarrow{c_2} = m_1\overrightarrow{c_1^*} + m_2\overrightarrow{c_2^*} = (m_1 + m_2)\overrightarrow{c_m} \tag{2.9}$$

$$m_1\overrightarrow{c_1^2} + m_2\overrightarrow{c_2^2} = m_1\overrightarrow{c_1^{*2}} + m_2\overrightarrow{c_2^{*2}} \tag{2.10}$$

Equation 2.9 shows that the centre of mass velocity is not affected by the collision. The values of pre- and post-collision, and the relative velocity between the molecules can be defined by:

$$\overrightarrow{c_r} = \overrightarrow{c_1} - \overrightarrow{c_2} \tag{2.11}$$

$$\overrightarrow{c_r^*} = \overrightarrow{c_1^*} - \overrightarrow{c_2^*} \tag{2.12}$$

By combining Equation 2.9 is combined with Equations 2.10 and 2.11, one obtains the following expressions:

$$\overrightarrow{c_1} = \overrightarrow{c_m} + \frac{m_2}{m_1 + m_2}\overrightarrow{c_r} \tag{2.13}$$

$$\overrightarrow{c_2} = \overrightarrow{c_m} - \frac{m_1}{m_1 + m_2}\overrightarrow{c_r} \tag{2.14}$$

The pre-collision velocities relative to the centre of mass are $\overrightarrow{c_1} - \overrightarrow{c_m}$ and $\overrightarrow{c_2} - \overrightarrow{c_m}$. Similarly, the post-collision, velocities are given by:

$$\vec{c_1^*} = \vec{c_m} + \frac{m_2}{m_1 + m_2} \vec{c_r^*} \tag{2.15}$$

$$\vec{c_2^*} = \vec{c_m} - \frac{m_1}{m_1 + m_2} \vec{c_r^*} \tag{2.16}$$

Based on these equations, it is seen that the post-collision velocities are also anti-parallel in the centre of mass frame of reference.

The conservation of angular momentum requires that the projected distance between the post-collision velocities be equal to the projected distance between the pre-collision velocities. As a result, Equations 2.13, 2.14 with 2.15 and 2.16 show that:

$$m_1 \vec{c_1^2} + m_2 \vec{c_2^2} = (m_1 + m_2) \vec{c_m^2} + m_r \vec{c_r^2} \tag{2.17}$$

$$m_1 \vec{c_1^{*2}} + m_2 \vec{c_2^{*2}} = (m_1 + m_2) \vec{c_m^2} + m_r \vec{c_r^{*2}} \tag{2.18}$$

where m_r is called the reduced mass and is given by:

$$m_r = \frac{m_1 m_2}{m_1 + m_2} \tag{2.19}$$

By comparing Equations 2.17 and 2.18 with the energy conservation Equation 2.10, it appears that the magnitude of the relative velocity is unchanged by the collision, i.e.,

$$\vec{c_r^*} = \vec{c_r} \tag{2.20}$$

Since $\vec{c_m}$ and $\vec{c_r}$ can be calculated from the pre-collision velocities, then the determination of post-collision velocity is reduced to calculating the change in direction of the χ relative to the velocity vector. If $\vec{F}$ is the force between two spherically symmetric points, and $\vec{r_1}$ and $\vec{r_2}$ their position vectors, the equations of motion of the molecules are as following:

31

$$m_1 \ddot{\vec{r}_1} = \vec{F} \tag{2.21}$$

$$m_2 \ddot{\vec{r}_2} = -\vec{F} \tag{2.22}$$

By combining these two equations, one has,

$$m_1 m_2 (\ddot{\vec{r}_1} - \ddot{\vec{r}_2}) = (m_1 + m_2)\vec{F} \tag{2.23}$$

By denoting the relative velocity vector by $\vec{r}$, then one obtains,

$$m_r \ddot{\vec{r}} = \vec{F} \tag{2.24}$$

In this way, the motion of the molecule of mass m_1 relative to the molecule of mass m_2 is equivalent to the movement of the molecule of mass m_r relative to a fixed center of force.

For completeness, the afore mentioned transformations are illustrated in Figure 2.4. According to these plots, the transformation from the centre of mass coordinate system changes a three-dimensional trajectory into a two-dimensional trajectory, which is symmetric about the apse line AA'. The two trajectories are reduced to one in the further transformation to the reduced mass frame of reference, and this trajectory remains symmetrical about the transformed apse line, which passes through the scattering centre O.

This symmetry reflects the symmetry of the equations related the pre- and post-collision velocities. Another consequence of this symmetry becomes apparent if one considers a collision between two molecules of velocities $\vec{c_1^*}$ and $\vec{c_2^*}$, and such that the separation of their undisturbed trajectories in the center of mass frame of reference is again equal to b.

This collision results in a post-collision velocities of $\vec{c_1}$ and $\vec{c_2}$ and is called the inverse of the original or direct collision.
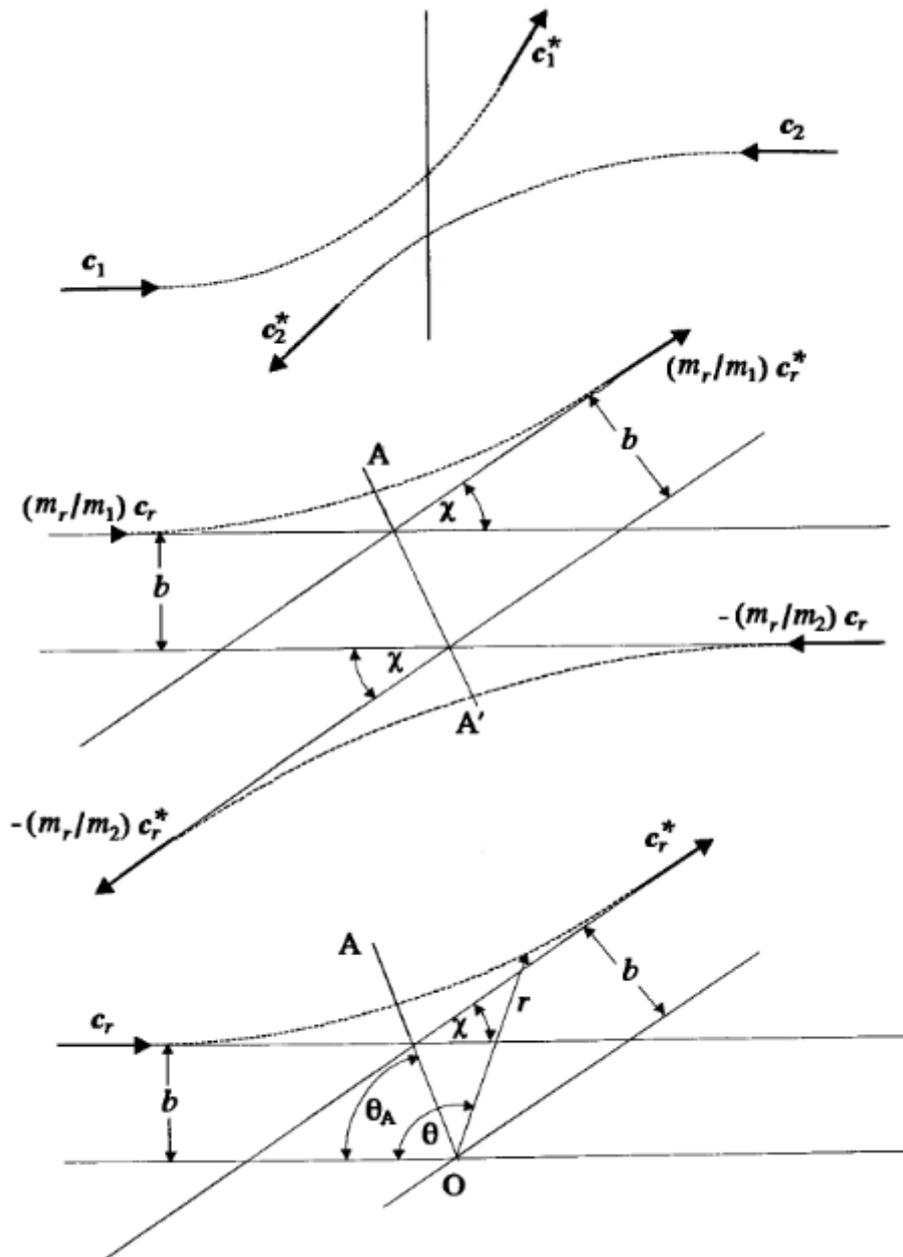
Figure 2.4 - Binary collision in the centre of mass frame reference.
Source: Bird (1994).

2.2.5 Internal Degrees-of-Freedom

One of the most significant effects observed in rarefied flows is the presence of a large degree of nonequilibrium between the various internal energy modes of the gas. For polyatomic gases, the transfer of energy to and from the internal modes has to be considered. However, energy transfer among translational, rotational and vibrational degrees of freedom cannot be accurately predicted using simple collision models.

The internal energy transfer between the various modes is usually implemented into the DSMC method by the phenomenological model introduced by Borgnakke and Larsen (BORGNAKKE; LARSEN, 1975). The essential feature of this model is that a fraction ϕ of translational collisions are assumed to be inelastic, and the remaining $(1-\phi)$ collisions are considered as elastic. The fraction ϕ can be interpreted as the average probability of rotational or vibrational energy exchange for translational collisions. This average probability can be determined from measured relaxation times. The relaxation time is a function of the local flow properties and can be related to a relaxation number (or collision number) Z. The relaxation or collision number Z is usually defined by,

$$Z = \frac{\tau}{\tau_c} \qquad (2.25)$$

where τ is the relaxation time and τ_c is the mean collision time. The relaxation or collision number is the average number of molecular collisions that are required for a particular mode to attain equilibrium energy. Therefore, once this number is determined, the average probability ϕ for each mode in a given collision is conveniently defined as,

$$\emptyset = \frac{1}{Z} \qquad (2.26)$$

In general, DSMC calculations use the rotational collision number Z_R on the order of 5. This means that, on average, a molecule rotationally relaxes once every five collisions.

This is generally a good engineering approximation. However, more realistic models for rotational collision number as a function of the translational temperature or translational energy have been proposed by Boyd (BOYD, 1990a; BOYD, 1990b; BOYD, 1990c).

Lumpkin et al. (LUMPKIN et al., 1991) have observed that the mechanisms of energy transfer employed in the DSMC calculation affect the rate of energy transfer. It is shown that the value of the collision number used in DSMC will be approximately half of that determined experimentally and employed in a continuum computation. They found the following relation,

$$Z_R^{DSMC} = \frac{Z_R^{Cont}}{\left(1 + \frac{\zeta_R}{\zeta_T}\right)} \tag{2.27}$$

where ζ_R and ζ_T are the rotational and translational degrees of freedom, respectively.

The vibrational relaxation number Z_V is also computed as a function of the flow properties. The relaxation number can be easily determined if the collision frequency and the relaxation time are known (Equation 2.25). The relaxation time of the vibrational mode is usually at least an order of magnitude larger than those associated with the translational and rotational modes of a molecule. In DSMC applications, a vibrational relaxation number Z_V on the order of 50 has been employed. This means that, on average, vibrational relaxation occurs for one in every fifty collisions.

The Borgnakke-Larsen method can be applied to the vibrational modes through either a classical or quantum procedure. In the classical procedure, the vibrational energy is treated as a continuous distribution described by a number of vibrational degrees of freedom ζ_V, which is fixed. In the quantum procedure, the discrete nature of vibrational spectrum is taken into account, since the vibrational spectrum of real molecules is characterized by large gaps between the neighboring energy levels. The quantum

procedure allows sampling of post-collision vibrational energy levels from the discrete form of the Simple Harmonic Oscillator (SHO). This procedure does not require the value of ζ_V to be estimated for the whole flowfield. Instead, ζ_V varies according to the local energy content of the flow. Both procedures are discussed at length by Bird's (BIRD, 1994). Vibrational relaxation number as a function of the collision energy is presented by Boyd and Bergemann (BOYD, 1990d; BOYD, 1991; BOYD; BERGEMANN, 1994) and as a function of temperature by Hash and Hassan (HASH; HASSAN, 1993).

2.2.6 Boundary Conditions

In the gas dynamics problems there are two basic types of boundary conditions: those specified by quantities given in the undisturbed freestream and those at a solid surface, where molecules interact or reflect directly.

The first condition is easily represented as a gas in equilibrium is moving with an imposed velocity. The molecular velocity distribution can be given as Maxwellian with an imposed velocity. This distribution holds for any ideal gas independently of the type of forces between molecules. The second condition depends on the treatment of gas-surface interactions. The influence of the model of gas-surface interactions on the aerodynamic forces and heat transfer increases substantially as the gas rarefaction increases. Therefore, the correct choice of the model for calculating hypersonic rarefied flows plays an important role.

Three models of gas-surface interactions may be employed in the DSMC method: (1) specular reflection, (2) diffuse reflection, and (3) a combination of these two methods. In a specular reflection, molecules are reflected like a perfectly elastic sphere with reversal of the normal component of velocity and no change in either the parallel components of velocity and energy. In a diffuse reflection, the molecules are reflected equally in all directions with a complete thermal accommodation. The final velocity

components of the reflected molecules are independent of their incident velocity and direction. The combination of diffuse reflection with specular reflection (Maxwell model) introduces a single parameter *f* to indicate the fraction of those molecules reflected diffusely in a completely accommodated fashion according to a Maxwellian distribution based to the wall temperature, the remaining fraction, (1-*f*), id assumed to reflect specularly.

The Maxwell model was followed by the introduction of three accommodation coefficients that describe the degree of accommodation of the incident normal momentum, tangential momentum and kinetic energy to the surface. A variety of definitions for accommodation coefficients exist in the literature. The traditional definition is usually expressed as being,

$$\alpha_r = \frac{e_i - e_r}{e_i - e_w} \tag{2.28}$$

$$\alpha_n = \frac{p_i - p_r}{p_i - p_w} \tag{2.29}$$

$$\sigma_t = \frac{\tau_i - \tau_r}{\tau_i} \tag{2.30}$$

where e_i, τ_i and p_i are fluxes of energy and of tangential and normal momentum, respectively, incident on the surface; e_r, τ_r and p_r are the fluxes of these quantities reflected form the surface; and e_w and p_w ($\tau_w = 0$) are the fluxes which would be reflected by a gas in complete Maxwellian equilibrium with the surface.

Data from many experiments show that molecules reflected or reemitted from solid surfaces present lobular distributions under high vacuum conditions and are poorly represented by the Maxwell model. However, this model is widely used because it satisfies the principle of detailed balance or reciprocity. Detailed balance means that at equilibrium every molecular process and its inverse process must individually balance.

37

A phenomenological model that satisfies detailed balance and has demonstrated improvement over the Maxwell model has been proposed by Cercignani and Lampis (CERCIGNANI; LAMPIS, 1971) (C-L model). This model is based on the definition of the accommodation coefficients σ_t and α_n that represent the accommodation coefficients for the kinetic energy associated with the normal and tangential components of velocity. The C-L model provides a continuous spectrum of behavior from specular reflection at one end to diffuse reflection with complete energy accommodation at the other, and produces physically realistic distributions of direction and energy reemitted molecules. Lord (LORD, 1991) has shown that the C-L model is suited for the DSMC method, and described how to incorporate it into the DSMC method. The DSMC method with Lord's implementation is referred as the Cercignani-Lampis-Lord (CLL) method. Figure 2.5 displays a schematic comparison of the Maxwell reflection model and the CLL reflection model. The C-L model has also been extended for covering diffuse scattering with partial energy accommodation and for simulating the accommodation of vibrational energy of a diatomic molecule modeled as simple harmonic oscillator (LORD, 1991) and an anharmonic oscillator (LORD, 1994).
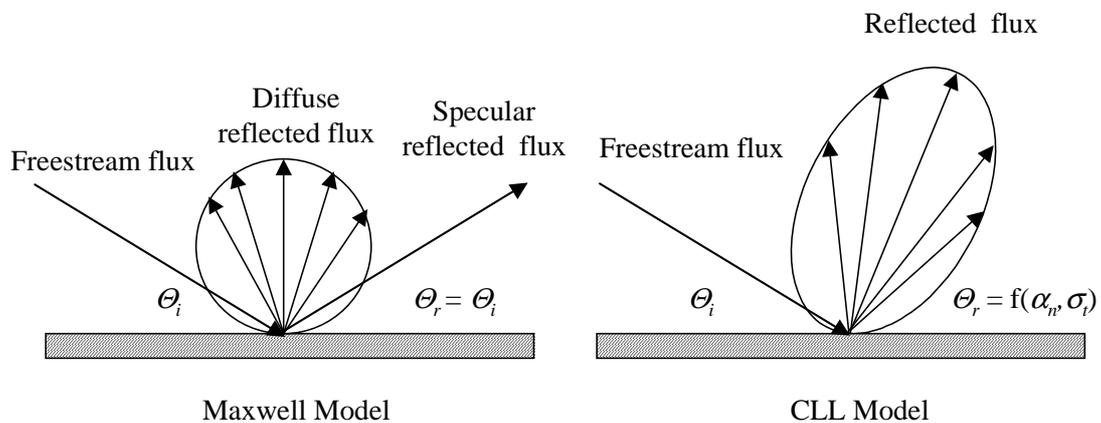
Figure 2.5 - Drawing illustrating the Maxwell reflection model and CLL reflection model.

3. COMPUTATIONAL PROCEDURE

3.1 Geometry Definition

Discontinuities or imperfections present on reentry vehicle surfaces is modeled in the present work by a gap with a length L and depth H. By considering that the depth H is generally of the order of 3 to 9 mm (EVERHART et al., 2006; GAI; MILTHORPE, 1995; GROTOWSKY; BALLMANN, 2000; HOZUMI et al., 2004; HINDERSKS; RADESPIED, 2006; JACKSON et al., 2001), and that the nose radius R of a reentry vehicle is approximately two order of magnitude larger than H, then $H/R \ll 1$. As a result, the hypersonic flow over the gap may be considered as a hypersonic flow over a flat-plate with a gap positioned far from the stagnation point at the vehicle nose.

Figure 3.1 illustrates a schematic view of the model employed and presents the important geometric and physical parameters. Referring to Figure 3.1, M_∞ represents the freestream Mach number, Kn_∞ stands for the Knudsen number, α the angle of attack, T_w the wall temperature, L_u the length of gap upstream surface, L the gap length, H the gap depth and L_d the length of the gap downstream surface. It was considered that the flat-plate is infinitely long but only the total length $L_u + L + L_d$ is investigated. In this fashion, for the cases investigated in this work L_u, L, L_d and H are tabulated in Table 3.1. The height H of 3, 6, 9 and 12mm correspond to height H of $3.23\lambda_\infty$, $6,46\lambda_\infty$, $9,69\lambda_\infty$ and $12.92\lambda_\infty$, where λ_∞ is the freestream mean free path.
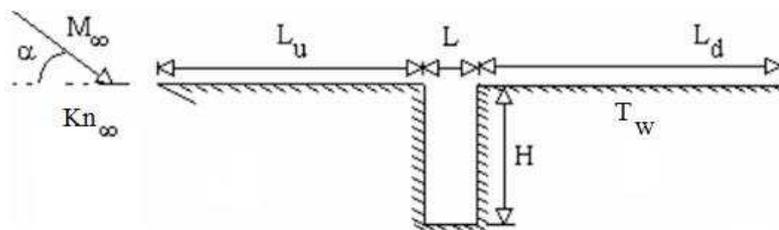
Figure 3.1 - Drawing illustrating the gap configuration.

Table 3.1 - Geometric features for the gaps.

Cases	L_u	L_d	L (mm)	H (mm)	L/H
A	$50\lambda_\infty$	$50\lambda_\infty$	3	3	1
B	$50\lambda_\infty$	$50\lambda_\infty$	3	6	1/2
C	$50\lambda_\infty$	$50\lambda_\infty$	3	9	1/3
D	$50\lambda_\infty$	$50\lambda_\infty$	3	12	1/4

In order to obtain a better understanding of the gap length-to-depth (L/H) ratio effects on the flowfield structure and on the aerodynamic surface properties, it becomes imperative to compare these properties with those on a flat-plate free of imperfections or discontinuities, i.e., without gaps. Thus, the solution obtained for a flat-plate free of discontinuities will represent a benchmark solution when compared to the cases with gaps.

3.2   Numerical Simulation Conditions

It was firmly established in chaprher 2 that the Boltzmann equation is the governing equation in the transition regime. The Boltzmann equation is a nonlinear integro-differential equation, closed with respect to the one-particle distribution function, which in turns determines the density of molecules in a six-dimensional phase space of particle coordinates and velocities. A detailed treatment of the Boltzmann equation can be found in Cercignani (CERCIGNANI, 1988). In order to avoid the difficulty of a direct solution of the Boltzmann equation, the DSMC method has been considered as one of the alternative approaches for solving the Boltzmann equation by simulating the behavior of individual molecules. It has been considered as the appropriate choice for problems involving complex multidimensional flows of rarefied hypersonic aerothermodynamics.

The DSMC algorithm used in the present study is built around the same basic physical concepts as described by Bird (BIRD, 1994). In this study, the molecular collisions are

modeled by using the variable hard sphere (VHS) molecular model and the no time counter (NTC) method as a collision-sampling technique. The energy exchange between kinetic and internal modes is controlled by the Borgnakke-Larsen phenomenological model (BORGNAKKE; LARSEN, 1975). The simulations are performed using a nonreactive air as working fluid with two chemical species, N_2 and O_2. An outline of the Borgnakke-Larsen phenomenological model in a form that is compatible with a gas mixture of VHS molecules is given by Bird (BIRD, 1989).

The probability of an inelastic collision determines the rate at which energy is transferred between the translational and internal modes after an inelastic collision. For a given collision, the probabilities are designated by the inverse of the relaxation numbers, which correspond to the number of collisions necessary, on average, for a molecule to relax. The relaxation numbers are assumed to be constant, on the order of $Z_r = 5$ for rotation and $Z_v = 50$ for vibration. The mechanics of vibrational energy exchange is also computed by the Borgnakke-Larsen approach with the post-collision vibrational energy levels sampled from the discrete form of the simple harmonic oscillator (SHO) (BIRD, 1994).

The rotational and vibrational relaxation models employed in this simulation are adjusted to match the continuum values by the correction presented in Equation 2.29. The freestream coefficient of viscosity μ_∞ and freestream mean free path λ_∞ are evaluated from a consistent definition (BIRD, 1983) by using the VHS collision model with the temperature exponent s (Equation 2.3) equal to 0.74 and 0.77 for N_2 and O_2, respectively. Table 3.2 summarizes the air characteristics used in the DSMC calculations.

The computational domain used for the calculations is large enough so that body disturbances do not reach the upstream and side boundaries, where freestream conditions are specified. The flowfield is divided into a number of regions and each one of them has a separate value of time step Δt and scaling factor F_N, which relates the

number of real molecules to the number of computational molecules. The ratio of these two quantities, F_N and $\varDelta t$, is the same in every region. The cell dimensions must be such that the change in flow properties across each cell is small; hence, the cell dimension is less than the local mean free path. Each cell is divided into four subcells, the smallest unit of physical space, where the collision partners are selected for the establishment of the collision rate. Also, time is advanced in discrete steps such that each step is small in comparison with the mean collision time. A view of the computational domain is depicted in Figure 3.2.

Table 3.2 - Characteristics of simulated air for DSMC calculations.

Properties	Values	Unity
Work fluid	N_2+O_2	
Molecular weight	28.96	kg/kg mole
Molecular mass of O_2	5.312×10^{-26}	kg
Molecular mass of N_2	4.650×10^{-26}	kg
Molecular diameter of O_2	4.010×10^{-10}	m
Molecular diameter of N_2	4.110×10^{-10}	m
Moles fraction of O_2	0.237	
Moles fraction of N_2	0.763	
Viscosity index (s) of O_2	0.77	
Viscosity Index (s) of N_2	0.74	
Degrees of freedom of O_2	5 to 7	
Degrees of freedom of N_2	5 to 7	

Referring to Figure 3.2, side I-A is the gap surface. Diffuse reflection with complete thermal accommodation is the condition applied to this side. Side I-B is a boundary where all flow gradients normal to the boundary are zero. Sides II and III are freestream sides through which simulated molecules can enter and exit. Finally, the flow at the downstream outflow boundary, side IV, is predominantly supersonic and vacuum condition is specified. At this boundary, simulated molecules can only exit. The choice of vacuum is normally used when the velocity of the gas through the boundary is supersonic. For flows with Mach number equal to or greater than three (BIRD, 1994), the molecules entering to the computational domain through the boundary can be neglected.

The grid generation, the effect of the grid resolution, and the verification and validation process employed in the present account are discussed in the next chapter.
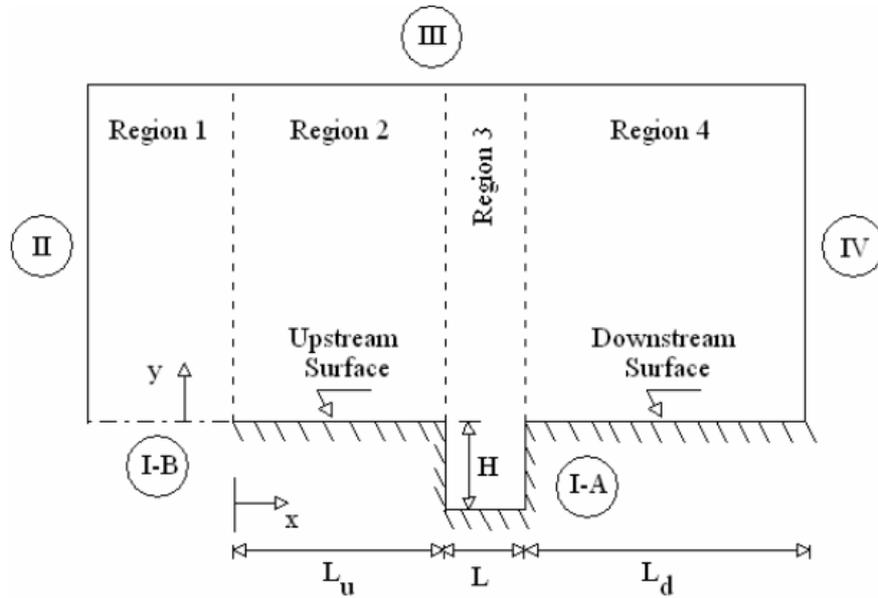
Figure 3.2 - Schematic view of the computational domain.

3.3 Freestream and Flow Conditions

The study at hand focuses on the influence of the gap length-to-depth (L/H) ratio on the flowfield structure. Effects of L/H ratio were investigated for L/H of 1, 1/2, 1/3 and 1/4, as defined by Table 3.1. The flow conditions are similar to those experienced by the SARA capsule at an altitude of 70 km. SARA (acronyms for SAtelite Recuperável Atmosférico) is a Brazilian satellite that has been developed by the IAE/DCTA (acronyms for Instituto de Aeronáutica e Espaço and Departamento de Ciência e Tecnologia Aeroespacial).

The Table 3.3 presents the freestream flow conditions used for the numerical simulations. The freestream velocity U_∞ is assumed constant as 7456 m/s, which corresponds to a freestream Mach number M_∞ of 25. The gap surface temperature T_w was assumed as a constant value of 880K. Diffuse reflection with complete thermal

accommodation was assumed for the gas-surface interaction. In addition, a flow with zero-degree angle of attack was assumed in this investigation.

By assuming the gap depth H as the characteristic length, the Knudsen number Kn_H corresponds to 0.3095, 0.1548, 0.1032 and 0.0774 for depth H of 3, 6, 9 and 12 mm, respectively. Finally, the Reynolds number Re_H is around 121.7, 243.4, 365.1 and 486.8 for H of 3, 6, 9 and 12 mm, respectively, also based on conditions in the undisturbed stream.

Table 3.3 - Freestream flow conditions.

Properties	Values	Unit
Velocity (U_∞)	7456	m/s
Temperature (T_∞)	219.69	K
Pressure (P_∞)	5.582	N/m^2
Density (ρ_∞)	8.753×10^{-5}	kg/m^3
Number density (n_∞)	1.819×10^{21}	m^{-3}
Viscosity (μ_∞)	1.455×10^{-5}	Ns/m^2
Mean free path (λ_∞)	9.285×10^{-4}	m

4.   CODE VERIFICATION AND VALIDATION

Before proceeding with the analysis of the computational results, it proves instructive to first examine the verification and validation processes. The DSMC verification and validation processes consist of three basic steps: (1) to verify the appropriate number of cells, (2) to verify the appropriate number of molecules, and (3) to compare DSMC results with analytic or experimental results available in the current literature. In this fashion, the purpose of this chapter is to discuss in detail these steps.

4.1   Computational Requirements

The DSMC method has become the most common computational technique for modeling complex transitional flows of engineering interest. The DSMC method models a gas flow by using a computer to track the trajectory of simulated molecules. Each simulated molecule represents a fixed number of real gas molecules. The simulated molecules are allowed to move and collide, while the computer store their position coordinates, velocities and energies. In order to do that, a computational mesh is used as a reference in the selection process of the collision pairs, and for sampling and averaging macroscopic flowfield properties. Currently, several methods of mesh generation have been used for different body shapes, each with its complexity and computational cost. Among them are: the body fitted, coordinate system implemented by Abe (ABE, 1989), the transfinite interpolation method made by Olynick et al. (OLYNICK et al., 1989) and multi-level Cartesian mesh proposed by Rault (RAULT, 1994).

In general, three basic types define mesh schemes: (1) uniform cartesian mesh, (2) structured body-fitted mesh, and (3) unstructured body-fitted mesh. Each of these schemes has advantages and disadvantages such as a low cost during the movement of molecules, the use of cells with non-uniform size in regions where the gradients are more intense, and application in simulation of complex geometries. Wilmoth et al.

45

(WILMOTH et al., 1996) and Nance et al. (NANCE et al., 1997) discuss in details the advantages of each scheme, in terms of accuracy, computational efficiency and ease of use.

Three primary constraints on the DSMC method must be considered when evaluating computational requirements: (1) the simulation time step must be less than the local average collision time, (2) the cell size must be smaller than the local mean free path, and (3) the number of molecules per cell must be roughly constant in order to preserve collision statistics.

An important assumption in the DSMC method is that the gas is dilute, meaning that the average molecular diameter is much smaller than the average spacing between molecules in the gas. This assumption allows that the molecular motion be decoupled from the molecular collisions over a small local time internal. Thus, the successful application of the method requires that the time step must be a fraction of the average time between collisions, as well as the cell dimensions must be of the order of one third of the local mean free path.

In order to accurately model the collisions through a statistical process, the cell size should be around one third of the local mean free path λ, becoming even smaller than λ in the directions in which the gradients are more intense (BIRD, 1994). In the vicinity of the body surface, the cell size in the normal direction to the surface should also be the order of or smaller than one third of the local mean free path. The reason for that is because in certain regions, such as the vicinity of adiabatic surfaces, flowfield gradients must be very small, and the cell size must be small enough to adequately capture flowfield physics near the body surface. Otherwise, the most energetic molecules so close to the far edge of the cell could transfer energy and momentum to molecules located immediately adjacent to the body surface. Moreover, such molecules adjacent the surface could transfer energy and momentum to the body surface. This leads to over prediction of heat flux to and the aerodynamic forces acting on the body surface. This

46

type of error can be minimized by reducing the cell size relative to the local mean free path of molecules near the surface. The cell size should be small in regions within the flowfield where the physical properties vary rapidly. For instance, in regions where the density is large, the cell size should be reduced in order to limit not only the number of molecules in each cell but also the number of collisions in a given time step.

In order to adequately model the physics of interest, the number of molecules in the simulation must be greater than a certain number. To obtain accurate collision statistics, it is desirable to have 20 - 30 computational molecules in each cell (ALEXANDER et al., 2000; FALLAVOLLITA et al, 1993). However, it is difficult to maintain this requirement when the density distribution in the computational domain is no longer uniform. As pointed out by Kannenberg and Boyd (KANNENBERG; BOYD, 2000), the number of molecules in the cell varies inversely with the gas density. Therefore high-density regions will tend to have few molecules, while low-density regions will have a large number of molecules resulting in over resolution in the flow domain. In order to overcome this difficulty, a variable scaling factor F_N is used to control the distribution of computational molecules within the grid. F_N is the ratio of real molecules and computational or simulated molecules.

In this scenario, the computational effort is substantially reduced by subdividing the flowfield into an arbitrary number of regions where the time step Δt and the scaling factor F_N remain constant within a region, but they can vary from one region to another one. The combination of subdividing the flowfield into regions along with the use of variable cell sizes provides the flexibility to substantially reduce the total number of molecules used in the simulation and also resolves the flow gradients. It is important to mention that although F_N and Δt can vary from region to region, the ratio $F_N/\Delta t$ must be the same for all regions in order to conserve mass across region boundaries in the flow.

More details for estimating the computational requirements of DSMC simulations are presented at length by Rieffel (RIEFFEL, 1999).

4.2   Computational Mesh Generation

The grid generation scheme used in this study was based on the procedure presented by Bird's G2 algorithm (BIRD, 1999). Basically the flowfield is divided into a number of arbitrary four-sided regions. Two opposite sides may be curved (sides I and III in Figure 3.5) and the other two are straight (sides II and IV in Figure 3.2). Along the boundaries, point distributions are generated in such way that the number of points on each side is the same. The cell structure is defined by joining the corresponding points on each side by straight lines and then dividing each of these lines into segments which are joined to form the system of quadrilateral cells. The distribution can be controlled by a number of different distribution functions which allow the concentration of points in areas where high flow gradients or small mean free paths are expected. The point distributions may be chosen independently for each region.

4.3   Computational Mesh Adaptation

The procedure for mesh adaptation employed in this study is threefold: (1) an initial region and cell mesh structure are generated from consideration of the freestream conditions, (2) assumed values of F_N are chosen for each region, Δt are then estimated subject to the condition that the ratio $F_N/\Delta t$ be the same for all regions, (3) these parameters are iteratively modified until an acceptable number of computational molecules, cell size distribution and simulation time step are obtained.

4.4   DSMC Test Case

The problem of hypersonic rarefied flow over a flat-plate is used to validate the two-dimensional version of the DSMC algorithm. The exceptionally simple geometry makes it the most useful test cases for the verification and validation process of the DSMC method through comparison with experiment. This model problem has been selected because both experimental data (BECKER et al., 1974) and previous numerical

48

simulations (CERCIGNANI; FREZZOTTI, 1989; HERMINA, 1989; LORD, 1994) are available for a comparison.

In the experiment setup, a flat-plate was placed along the centerline of an orifice jet. The helium flowfield was generated by the freejet expansion from a distance of the flat-plate that resulted in a freestream Mach number of 8.9, freestream temperature of 10.7 K and freestream pressure of 0.337 N/m^2. The plate was 50.8 mm long, 25.4 mm wide and a leading edge sharpness of 0.04 mm. The freestream Knudsen number based on plate length was 0.0253. The local Knudsen number can be significantly larger as a result of the high temperatures within the thermal boundary layer. Table 4.1 gives detailed information of the freestream and flow conditions at the leading edge.

In the computational solution, it is assumed that the flat-plate is immersed in a uniform stream flowing parallel to the plate itself. The flat-plate is modeled as one with zero thickness and length of 102.8 mm, which corresponds to $80\lambda_\infty$. The undisturbed freestream boundary conditions were imposed at $5\lambda_\infty$ upstream of the plate leading edge, and the computational domain normal to the plate extends to a distance of $30\lambda_\infty$ from the plate surface. The calculations are performed on a rectangular mesh above the plate

The computational domain used for the simulation was made large enough so that flat-plate disturbances did not reach the upstream and side boundaries, where freestream conditions were specified. A schematic view of the computational domain was divided into two regions, which were subdivided into computational cells. In this manner, region 1 consisted of 10 cells along side I-B and 40 cells along side II. Region 2 consisted of 300 cells distributed along side I-A and 80 cells along side IV. This computational mesh was defined as being the standard case. In addition to this mesh, two other meshes, defined by coarse and fine, were used to study the sensitivity of the computations to mesh resolution.
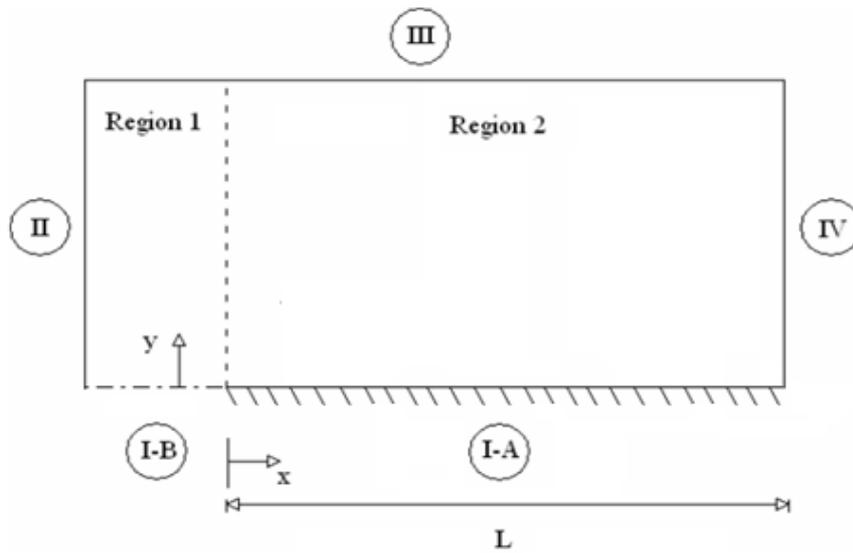
Figure 4.1 - Drawing illustrating the flat-plate computational domain.

Table 4.1 - Freestream and flow conditions for the test case.

Properties	Values	Unity
Velocity (U_∞)	1723	m/s
Temperature (T_∞)	10.7	K
Pressure (p_∞)	0.3379	N/m^2
Density (ρ_∞)	$1.520\text{x}10^{-5}$	kg/m^3
Number density (n_∞)	$2.285\text{x}10^{21}$	m^{-3}
Viscosity (μ_∞)	$1.865\text{x}10^{-5}$	Ns/m^2
Mean free path (λ_∞)	$1.286\text{x}10^{-3}$	m
Wall temperature (T_ω)	290	K
Model length	50.8	mm
Model length	25.4	mm
Bevel angle	20º	
Reynolds number (Re_∞)	71.3	
Mach number (M_∞)	8.9	
Knudsen number (Kn_∞)	0.0253	

4.4.1   Effect of Mesh Resolution

The effect of mesh resolution on computational results is of particular interest for the present study since insufficient grid resolution can reduce significantly the accuracy of predicted aerodynamic heating and forces. Hence, heat transfer, pressure and skin

50

friction coefficients are used as the representative parameters for the grid sensitivity study.

The effect of altering the mesh resolution in the x and y direction was investigated for a coarse and fine mesh with, respectively, 50% less and 100% more cells with respect to the standard mesh. Table 4.2 tabulates the number of cells employed in the two regions for coarse, standard and fine meshes. Furthermore, each mesh was made up of non-uniform cell spacing in both directions.

Table 4.2 – Number of cells in the (x-direction) and [y-direction] for the flat-plate.

	Region 1	Region 2	Cells
Coarse	(5x40) [10x20]	(150x80) [300x40]	12.200 12.200
Standard	10x40	300x80	24.400
Fine	(20x40) [10x80]	(600x80) [300x160]	48.800 48.800

The effect of changing the number of cells in the x-direction on pressure C_p, skin friction C_f and heat transfer C_h coefficients is illustrated in Figure 4.2. In this set of plots, the dimensionless length X corresponds to the length x normalized by the freestream mean free path λ_∞. Based on this set of plots, it is clearly seen that the calculated results are not affected to the range of cell spacing considered for the x-direction in the cases defined by coarse, standard and fine meshes. Also the effect of cell variations on the flowfield properties (not shown) was negligible.

A similar examination was made in the y-direction. The sensitivity of the calculated results to cell size variations in the y-direction is displayed in Figure 4.3. In this figure, a new series of three simulations, with grids in the region 2 of 300 cells in the x-direction and 40, 80 and 160 cells in the y-direction, are compared. The cell spacing in both directions is again nonuniform. According to this figure, the results for three independent meshes are approximately the same, indicating that the standard mesh is

essentially grid independent. For the standard case, the cell size in the y-direction is always less than the local mean free path length in the vicinity of the surface.

4.4.2 Effect of Number of Molecules Variations

A similar examination was made for the number of molecules. The sensitivity of the calculated results to number of molecules variations is demonstrated in Figure 4.4. The standard grid corresponds to a total of 512.800 molecules. Two new cases using the same grid were investigated. These new cases correspond to, on average, 256.400 and 1.025.600 molecules in the entire computational domain. The number of molecules was increased by changing the scaling factor F_N defined earlier. It is seen that the results are the same for all of the cases, indicating that the standard grid with a total of 512.800 molecules is enough for the computation of the flowfield properties.

4.4.3 Effect of Downstream Boundary Condition

In order to determine the extent of the interference region of the imposed downstream vacuum boundary condition used on side IV (Figure 4.1), calculations were made for two other plate lengths. Figure 4.5 presents a comparison of the aerodynamic surface quantities as calculated with the short plate, $60\lambda_\infty$, the standard plate, $80\lambda_\infty$, and the long plate with $100\lambda_\infty$. It is seen that the imposed boundary condition has a noticeable effect on the aerodynamic surface quantities for at least twenty freestream mean free paths upstream of this boundary.
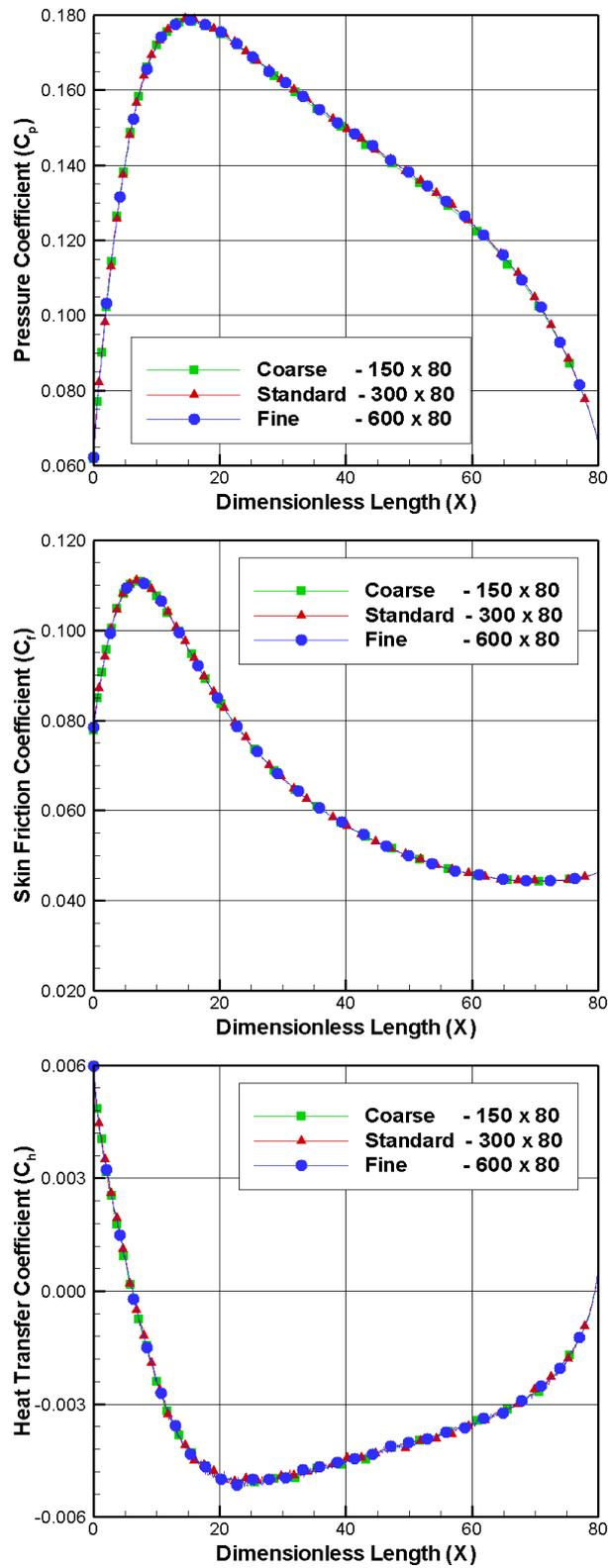
Figure 4.2 - Effect of variation in the cell size in the *x*-direction coordinate on pressure (top), skin friction (middle) and heat transfer (bottom) coefficients.

53
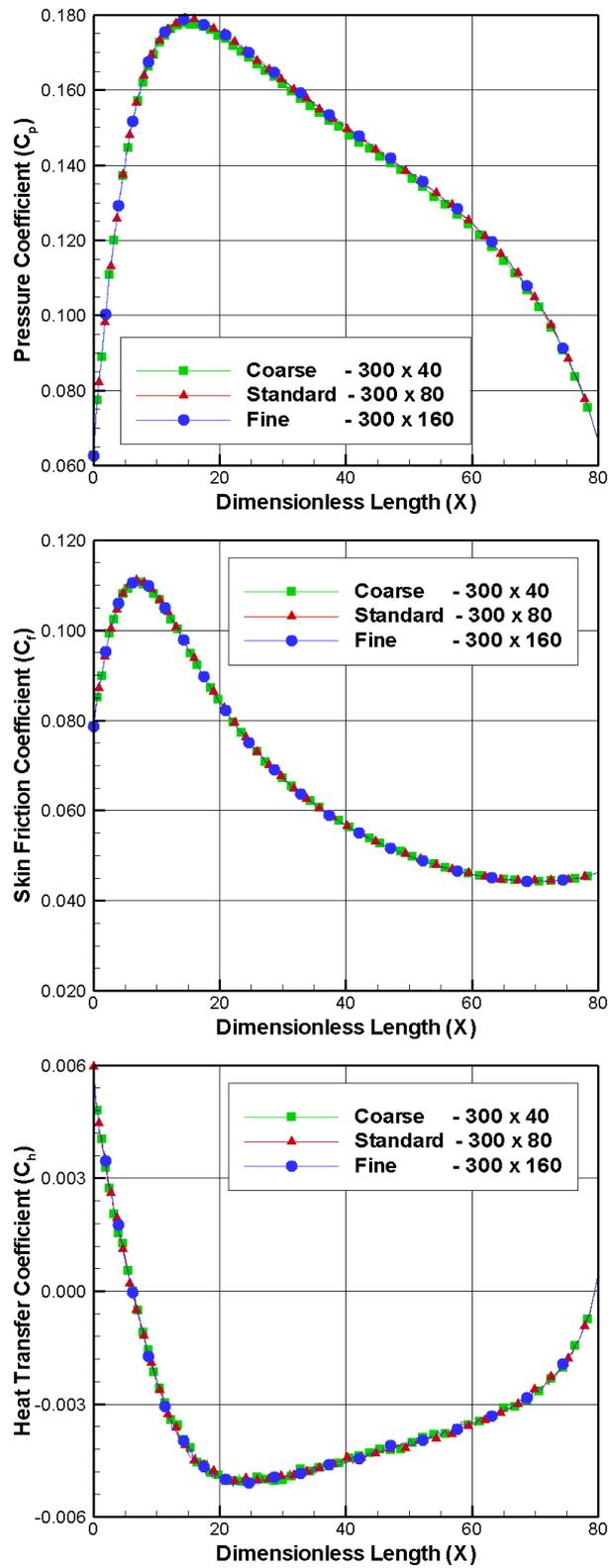
Figure 4.3 - Effect of variation in the cell size in the *y*-direction coordinate on pressure (top), skin friction (middle) and heat transfer (bottom) coefficients.
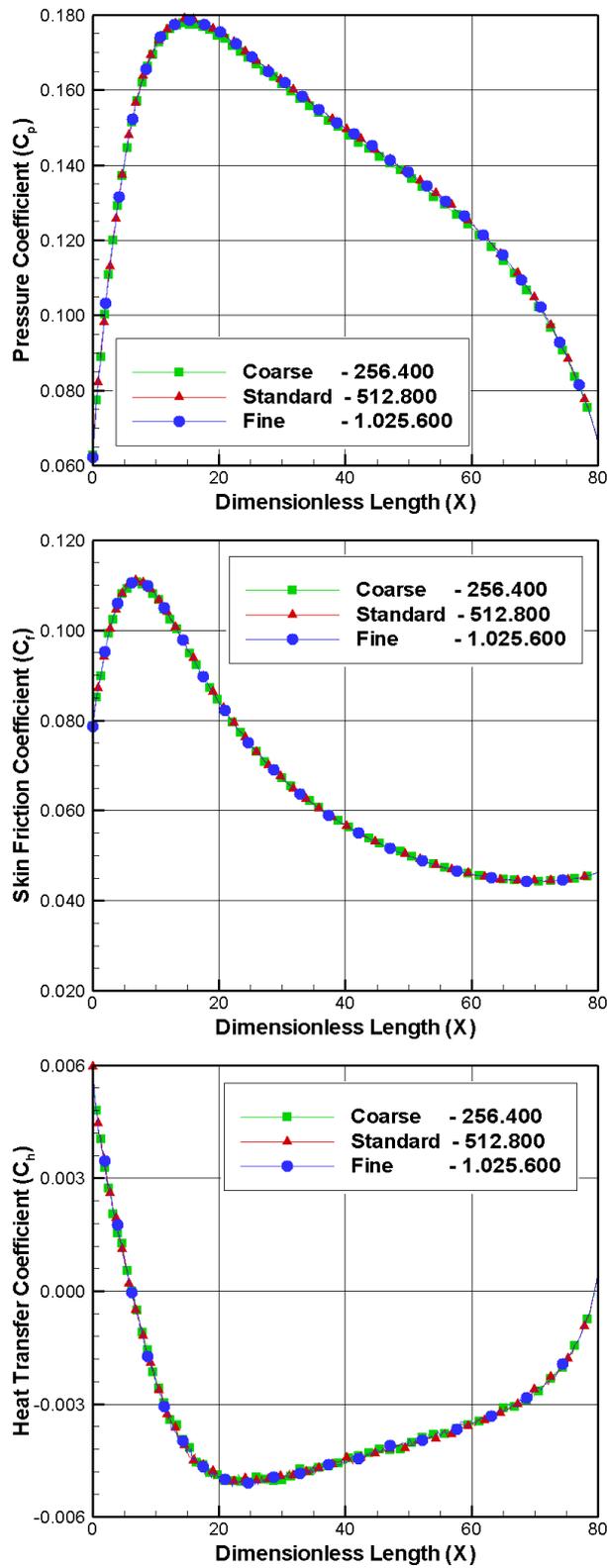
Figure 4.4 - Effect of variation in the number of molecules on pressure (top), skin friction (middle) and heat transfer (bottom) coefficients.
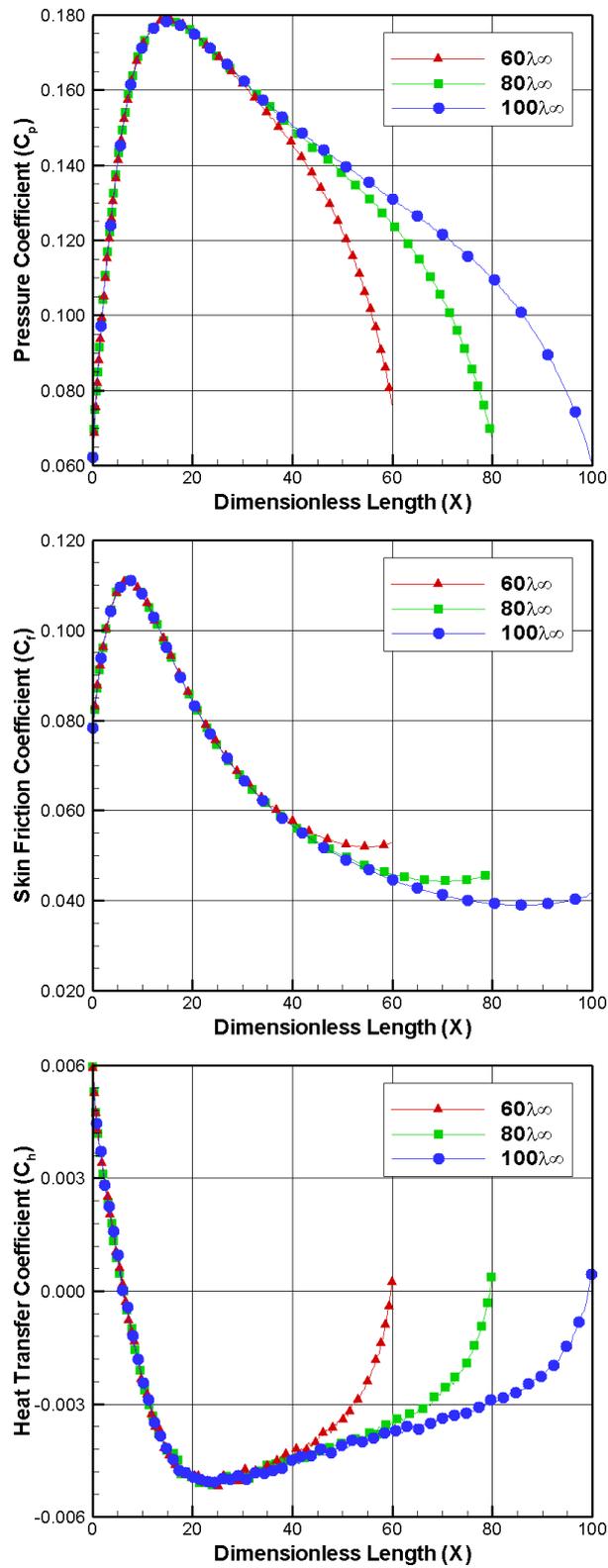
Figure 4.5 - Effect of variation in the flat-plate length on pressure (top), skin friction (middle) and heat transfer (bottom) coefficients.

4.4.4   Experimental and Numerical Comparisons

This section presents the comparisons with experimental data and with a series of numerical simulation data in order to ascertain how well the DSMC algorithm employed in this study is able to predict hypersonic rarefied flows. Since these data have been published elsewhere, details will be kept to the minimum and the discussion restricted to the significant conclusions.

Density profiles normal to the flat-plate surface are illustrated in Figure 4.6 for six axial position, ranging from the leading edge, $x = 0.5$mm to a position $x = 31.5$mm downstream of the leading edge. In this set of plots, density ρ is normalized by the freestream density ρ_∞, and dimensionless height Y corresponds to the height y normalized by the freestream mean free path λ_∞. In addition, solidlines represent the present DSMC simulations, full and empty symbols correspond, respectively, to experimental and numerical data available in the literature. Furthermore, the dependence of the density on axial location was measured for only three values of the y coordinate, i.e., $y = 1.25$, 2.5 and 5.0 mm. Details of the experimental tests are given by Becker et al. (BECKER et al., 1974). The numerical simulation data shown were obtained by Hermina (HERMINA, 1989) by employing the DSMC method, and by Cercignani and Frezzoti (CERCIGNANI, FREZZOTI, 1989) by means of the Boltzmann equation.

It is immediately evident from Figure 4.6 that there is a close overall agreement between the present DSMC simulation and the measured and calculated data near the leading edge of the plate. However, as the trailing edge is approached, a significant disagreement is observed between the experiment results and those of the present simulations, which predict higher density ratios. According to Lord (LORD, 1994), that analyzed the same problem by employing the DSMC method, this discrepancy cannot be attributed to surface accommodation, which appears to have very little effect, and is currently unexplained. In his analysis, the effects of the gas-surface interaction on the

57

flowfield were studied by assuming that molecules are reflected from the plate according to the Cercignani-Lampis-Lord (CLL) model. The comparison of the present simulations with those presented by Lord will be shown later for the case of complete accommodation.

Tangential velocity profiles normal to the flat-plate surface are demonstrated in Figure 4.7 for the same six axial positions. In this group of plots, the tangential velocity u is normalized by the freestream velocity U_∞. According to this group of plots, a strong velocity slip at the wall is observed near the leading edge, decreasing downstream along the plate due to the increasing number of molecular collisions with the wall. The comparison of the computed results with the experimental data shows that in the vicinity of the leading edge the computed velocities are larger than the measured velocities. Nevertheless, as the trailing edge is approached, the measured velocities are larger than the computed ones. According to Hermina (HERMINA, 1989), this is an indication that the accommodation coefficient used in the calculations is too small near the leading edge and too large at the downstream positions. In contrast to the density profiles, the tangential velocity profiles for the present DSMC calculations present a good agreement as compared to those of other computational results.

In analogous fashion, variations in temperature profiles, normalized by the freestream temperature T_∞, are displayed in Figure 4.8. It is apparent from this set of plots that the temperature jump at the wall is seen to diminish rapidly downstream along the plate. Similarly to velocity slip, the temperature jump at the wall decreases as a result of the increasing number of molecular collisions with increasing axial position. Once again, it is immediately evident that there is close overall agreement between the present DSMC calculations and the other computational results for temperature profiles.

58
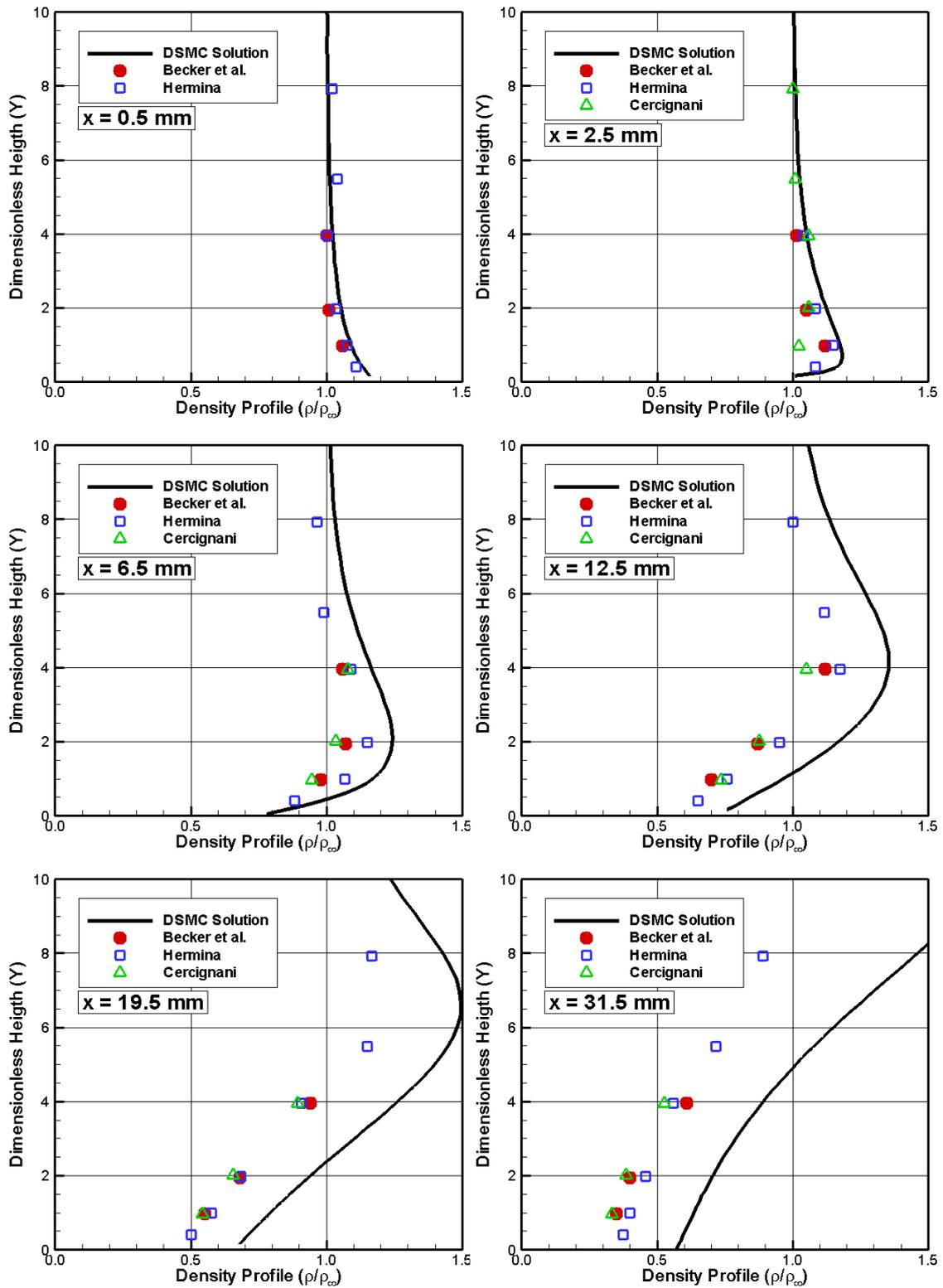
Figure 4.6 - Dimensionless density profiles normal to the flat-plate surface for various stations along the flat-plate. Solid lines represent the present DSMC computations, full and empty symbols represent experimental and numerical data, respectively.

59
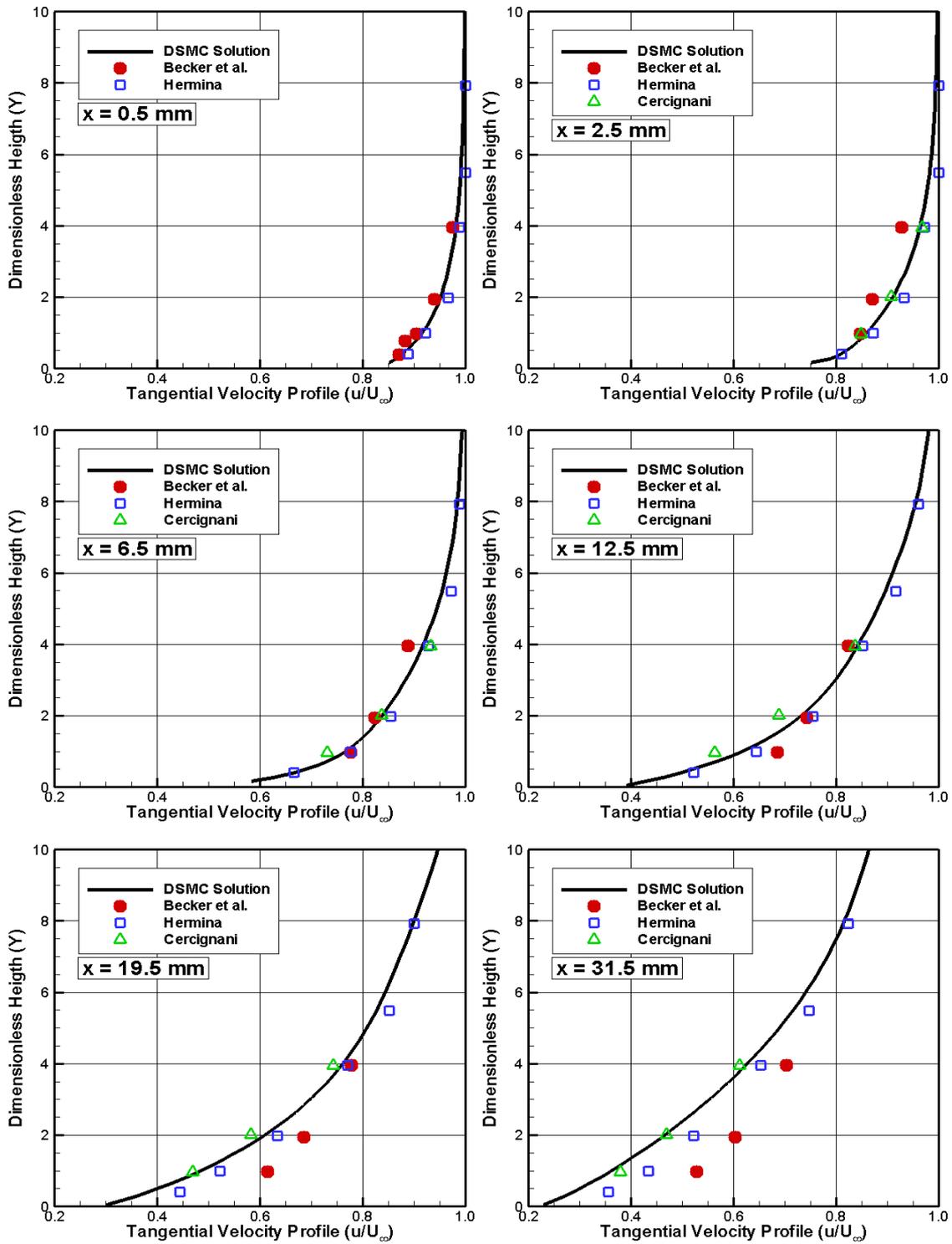
Figure 4.7- Dimensionless tangential velocity profiles normal to the flat-plate surface for various stations along the flat-plate. Solid lines represents the present DSMC computations, full and empty symbols represent experimental and numerical data, respectively.
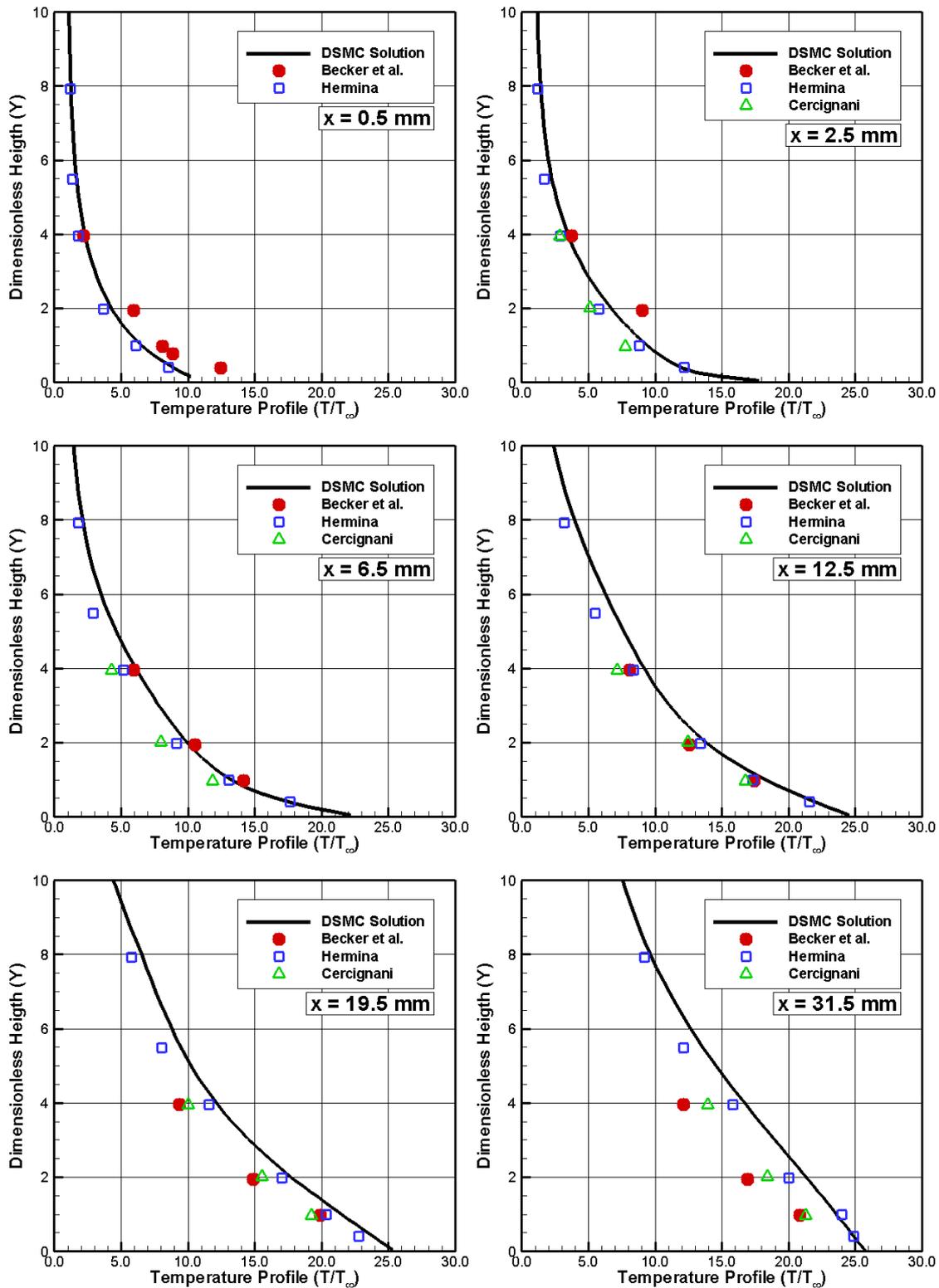
Figure 4.8 - Dimensionless temperature profiles normal to the flat-plate surface for various stations along the flat-plate. Solid lines represents the present DSMC computations, full and empty symbols represent experimental and numerical data, respectively.

61

In the following, longitudinal variations of the flow properties are depicted in Figures 4.9, 4.10 and 4.11. In this group of figures, dimensionless length X corresponds to the length x normalized by the freestream mean free path λ_∞. Again, solid lines represent the present DSMC simulations, and full and empty symbols stand respectively, for experimental and numerical data. Longitudinal variations of density ratio ρ/ρ_∞ profiles are illustrated in Figure 4.9 at a distance of 1.25mm from the flat-plate surface. According to this figure, a good agreement is observed between the present simulation and the Lord (LORD, 1994) simulation. However, both DSMC solutions are far from the measured results as the axial position increases. The same significant disagreement between the experimental data and those of the DSMC simulations for density ratios was shown earlier in Figure 4.6.

The corresponding longitudinal variations of the tangential velocity is displayed in Figure 4.10. From this figure, it is again evident that there is close overall agreement between the computational solutions. Nevertheless, the comparison with the experimental data shows that the calculated tangential velocities drop much faster downstream of the flat-plate leading edge than the measured ones.

Finally, Figure 4.11 exhibits the corresponding variation of the gas temperature normalized by its freestream value. From this figure, it is also apparent that optimal agreement is obtained between the calculated results yielded by the DSMC method.

The aforementioned, comparisons were made between several calculated and measured results for the hypersonic flow of Helium over a flat-plate. The analysis of the numerical results leads to the conclusion that agreement with the experimental results is remarkably close to the leading edge but becomes less exact downstream along the flat-plate. If differences on the results were attributed to the computational method, then, at least at first sight, they should indicate the inadequacy in the gas surface interaction model.
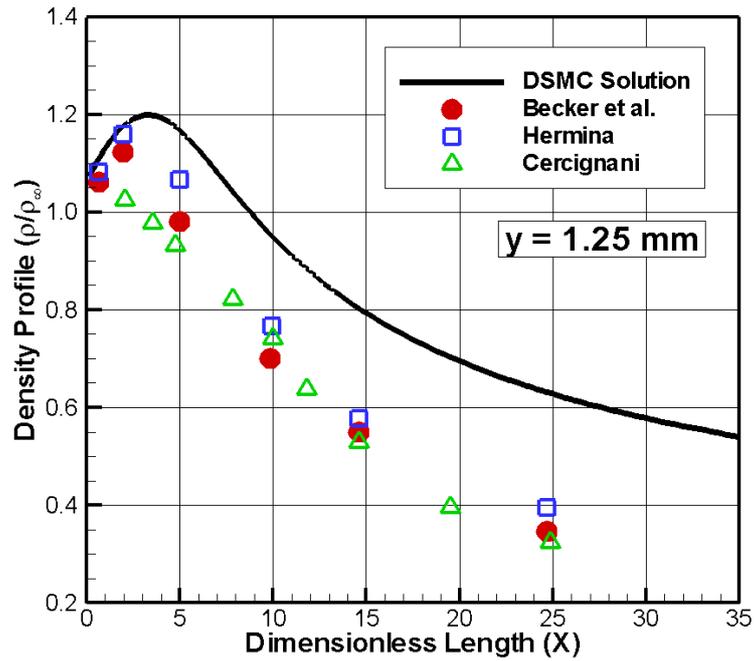
Figure 4.9 - Density profiles along the flat-plate at station *y* = 1.25 mm. Solid line represents the present DSMC computations, full and empty symbols represent experimental and numerical data, respectively.
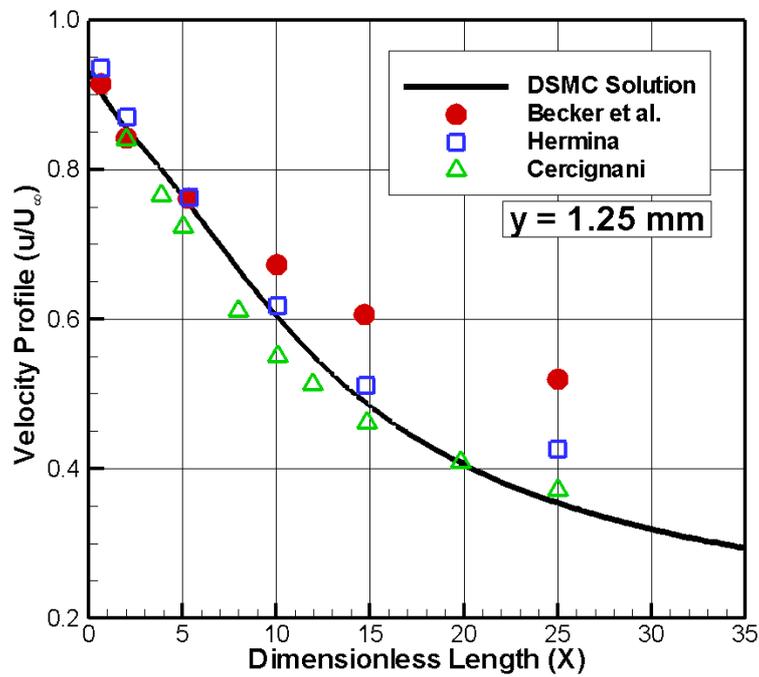
Figure 4.10 - Tangential velocity profiles along the flat-plate at station *y* = 1.25 mm. Solid line represents the present DSMC computations, full and empty symbols represent experimental and numerical data, respectively.
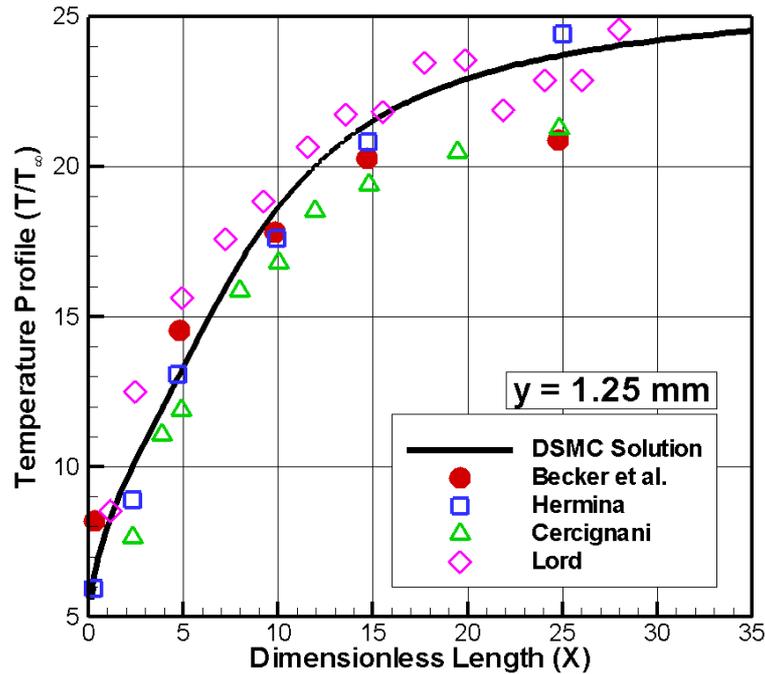
Figure 4.11 - Temperature profiles along the flat-plate at station $y = 1.25$ mm. Solid line represents the present DSMC computations, full and empty symbols represent experimental and numerical data, respectively.

This is further corroborated by the results obtained by Hermina (HERMINA, 1989), and Cercignani and Frezzotti (CERCIGNANI; FREZZOTTI, 1989) that showed a better agreement by taking into account the incomplete surface accommodation. However, comparisons taking into account incomplete surface accommodation results are beyond the scope of the present validation process that is restricted only to the complete surface accommodation.

Moreover, some caution must also be exercised in drawing definite conclusions from the comparisons since each simulation differs in some characteristics. For instance, Hermina (HERMINA, 1989) considered a diverging flow of Helium gas along the flat-plate, and took into account for the finite plate thickness and leading-edge level angle, as used in the experimental model. Cercignani and Frezzotti (CERCIGNANI; FREZZOTTI, 1989) performed the calculations by assuming that the flat-plate was placed inside an axisymmetric jet from a sonic orifice. However, the interaction between the axisymmetric jet and the flat-plate was not treated correctly because the

resulting 3-D flow was calculated as a 2-D one. Therefore, the effect of the jet divergence on the entire flowfield is to be expected. Also, a uniform stream flowing parallel to the flat-plate rather than a field having the divergence of the free jet flow has been used in the present DSMC simulation as well as in Lord (LORD, 1994) simulations.

4.5   Gap Case

Analogous to the procedure adopted for the flat-plate, simulations with different configurations of computational meshes have also been applied to the gap cases mentioned in Chapter 3, respecting the restrictions of the DSMC method already mentioned in sections 4.1 to 4.3. Since for a flat-plate, the gradients are more intense near the surface and for a gap, the gradients are more intense inside of it, the clustering of the computational mesh was intensified in these regions.
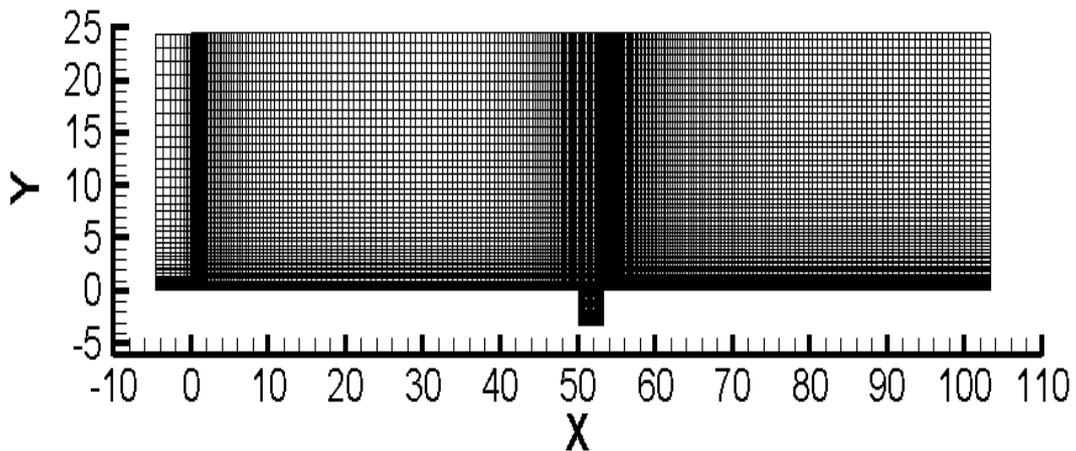
Figure 4.12 - Drawing illustrating the computational domain for standard gap case.

The effect of altering the mesh resolution in the *x* and *y* directions was investigated for a coarse and fine mesh with, respectively, 50% less and 100% more cells with respect to the standard mesh. Figure 4.12 illustrate the gap standard computational mesh and Table 4.3 tabulates the number of cells employed in the four regions for coarse, standard and fine meshes. Furthermore, each mesh was made up of non-uniform cell spacing in both

directions.

Table 4.3 – Number of cells in the (*x*-direction) and [*y*-direction] for the gap case of *L/H*=1.

	Region 1	Region 2	Region3	Region 4	Cells
Coarse	(5x40) [10x20]	(60x50) [120x25]	(10x70) [20x35]	(60x60) [120x30]	7.500 7.500
Standard	10x40	120x50	20x70	120x60	15.000
Fine	(20x40) [10x80]	(240x50) [120x100]	(40x70) [20x140]	(240x60) [120x120]	30.000 30.000

The effect of changing the number of cells in the *x*-direction and in the y-direction on pressure C_p, skin friction C_f and heat transfer C_h coefficients is illustrated in Figures 4.13 – 4.18. In this set of plots, the dimensionless length *X* corresponds to the length *x* normalized by the freestream mean free path λ_∞ and dimensionless height Y'_H is the height (*y+H*) normalized by the gap depth *H*.

A similar examination was made for the number of molecules and showed in Figures 4.19 – 4.21. The standard mesh for *L/H*=1 case corresponds to, on average, a total of 315.000 molecules. Two news cases using the same grid were investigated. These two new cases correspond to 157.500 and 630.000 molecules in the entire computational domain. As the three cases presented the same results for the heat transfer, pressure and skin friction coefficients, hence the standard grid with a total of 315.000 molecules was considered enough for the computation of the flowfield properties.
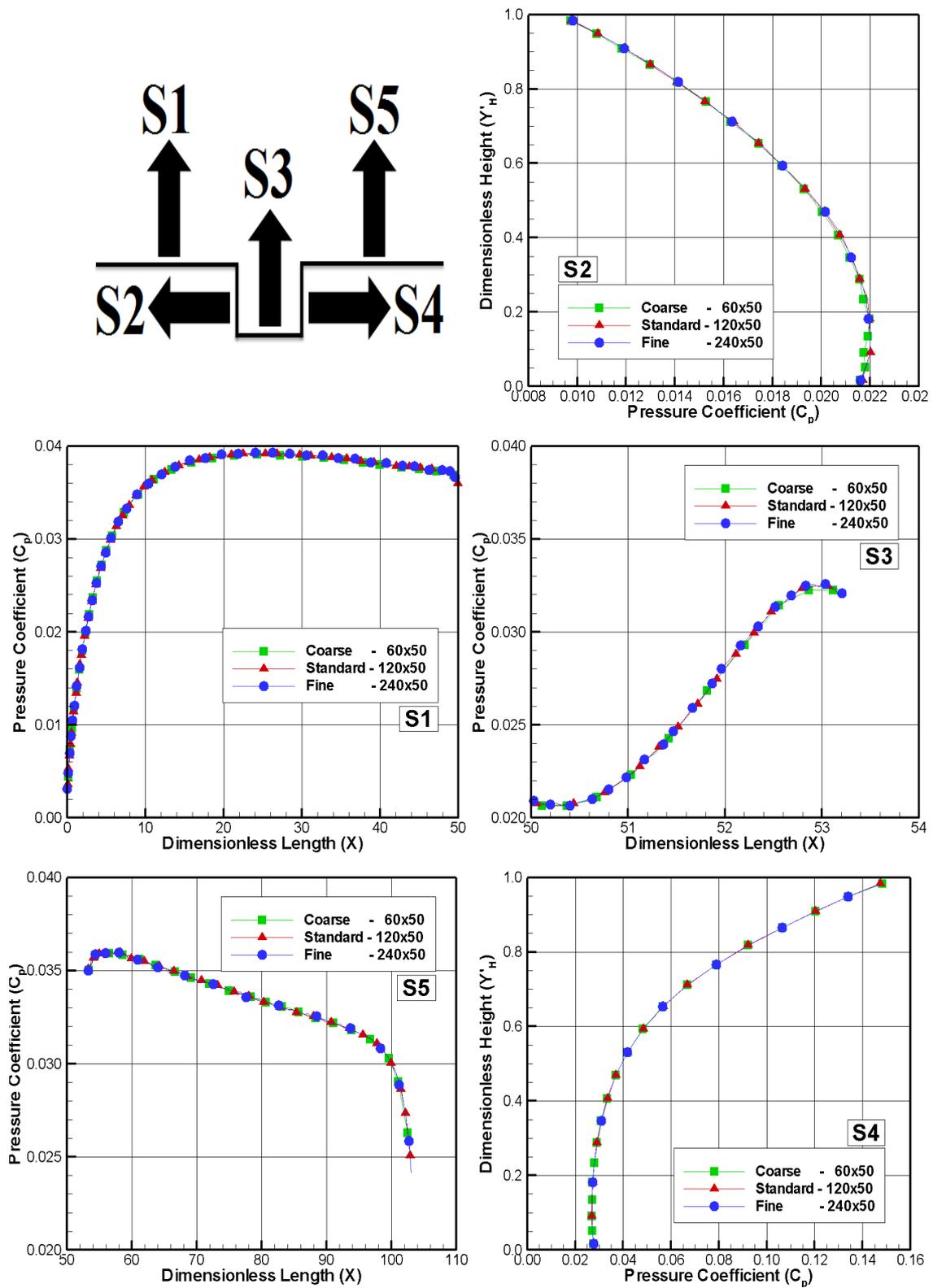
Figure 4.13 - Effect of variation in the cell size in the *x* direction in pressure coefficient for *L/H*=1.
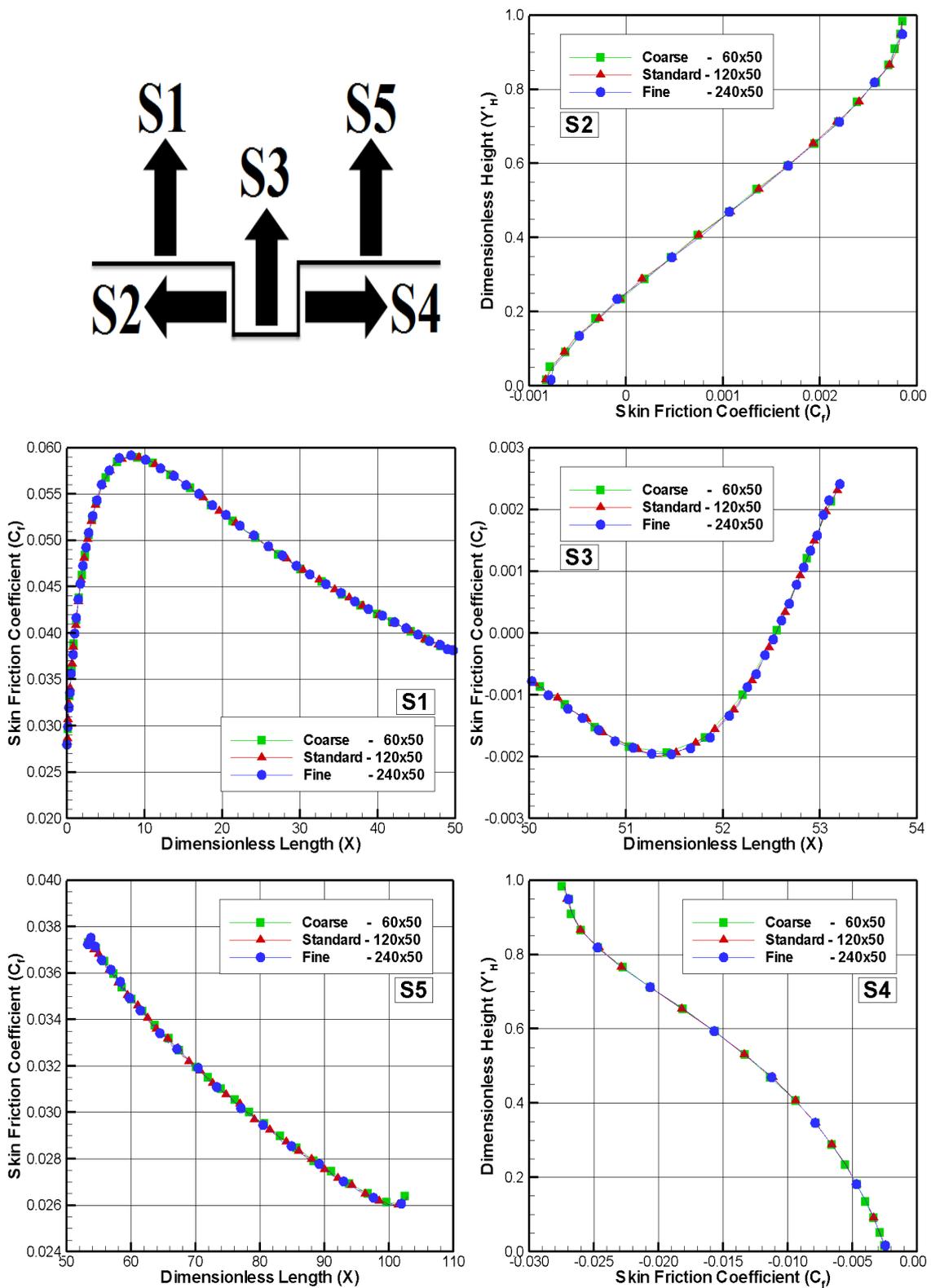
Figure 4.14 - Effect of variation in the cell size in the *x* direction in skin friction coefficient for *L/H*=1.
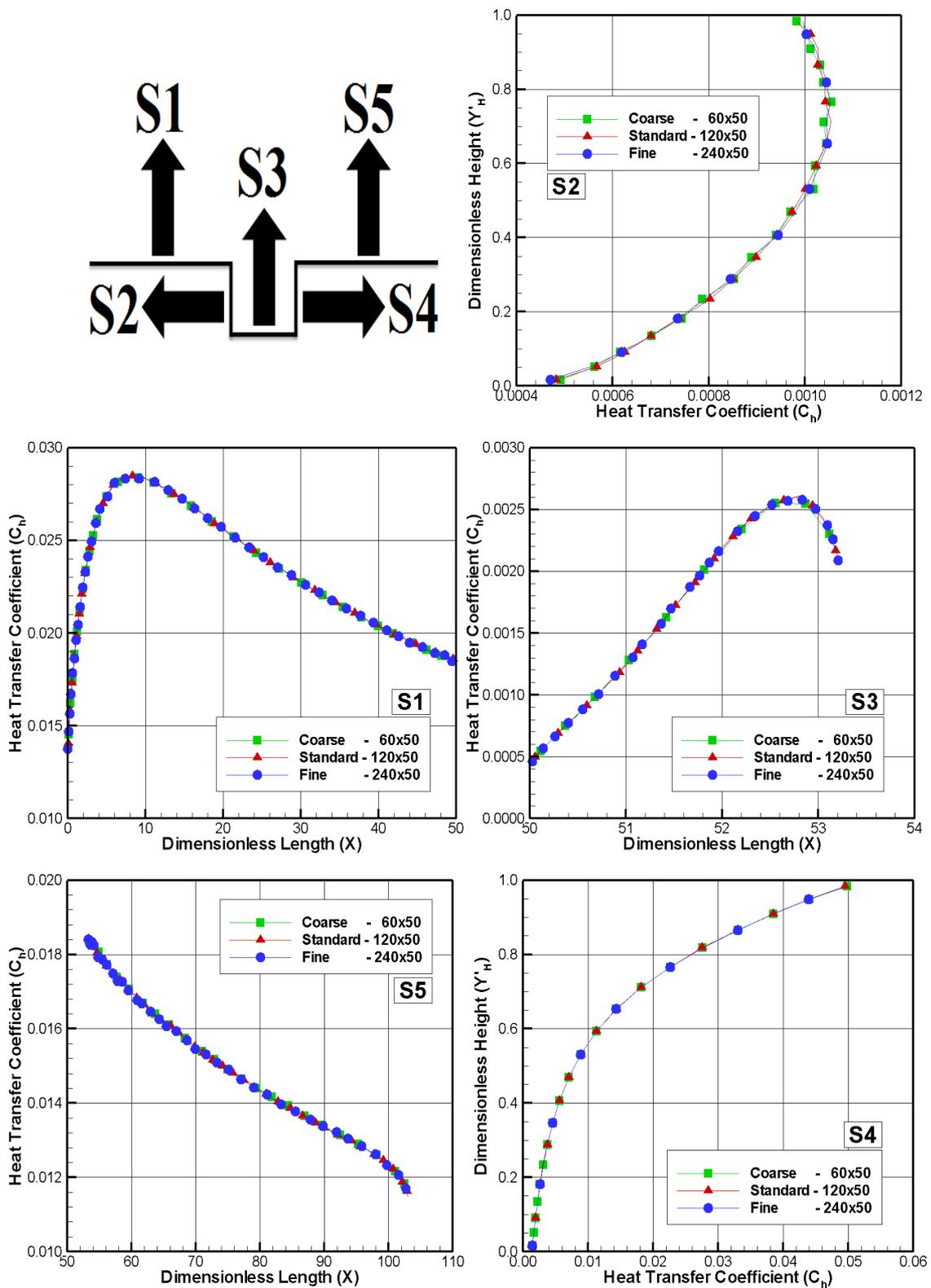
Figure 4.15 - Effect of variation in the cell size in the *x* direction in heat transfer coefficient for *L/H*=1.
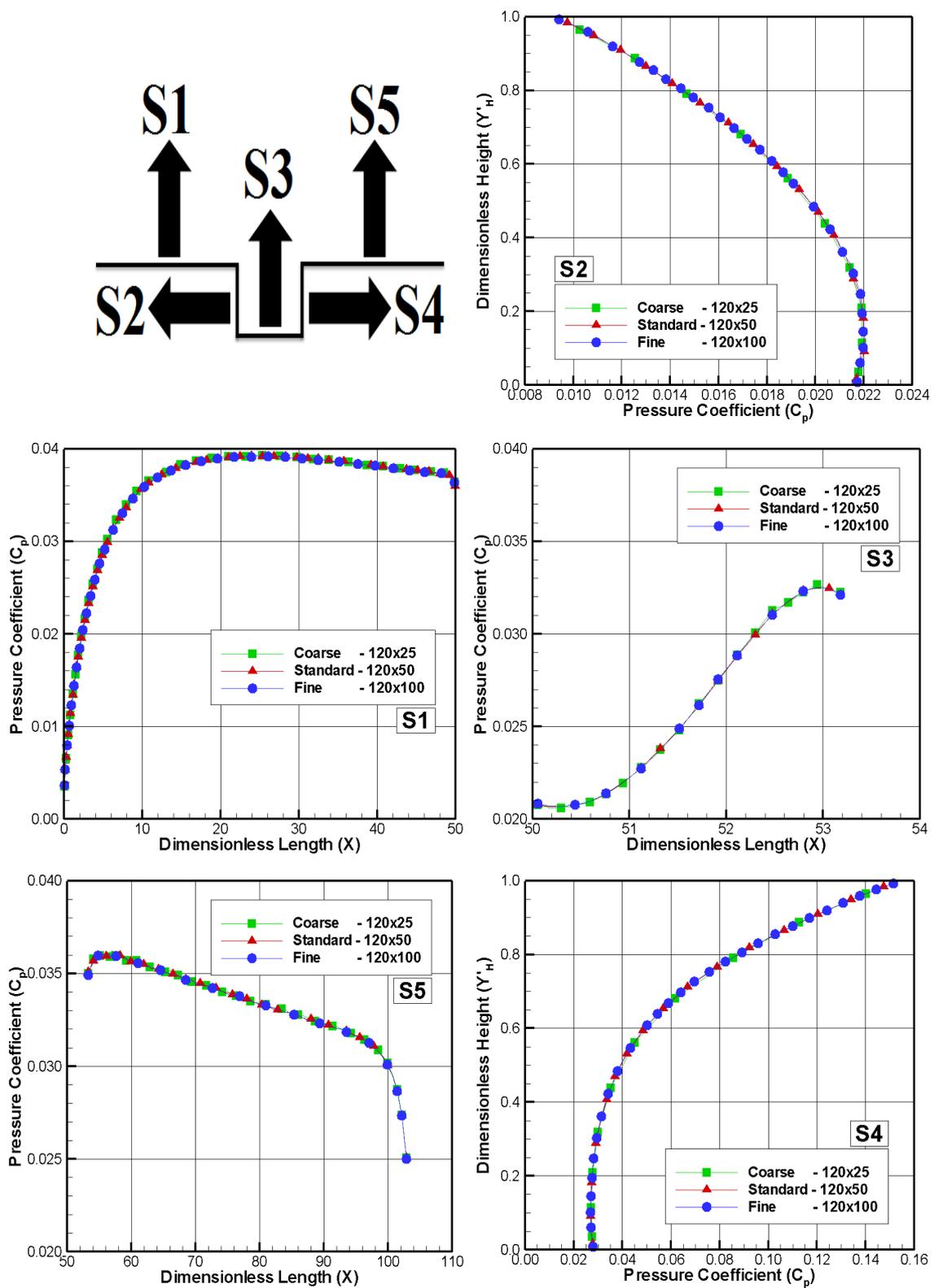
Figure 4.16 - Effect of variation in the cell size in the *y* direction in pressure coefficient for *L/H*=1.
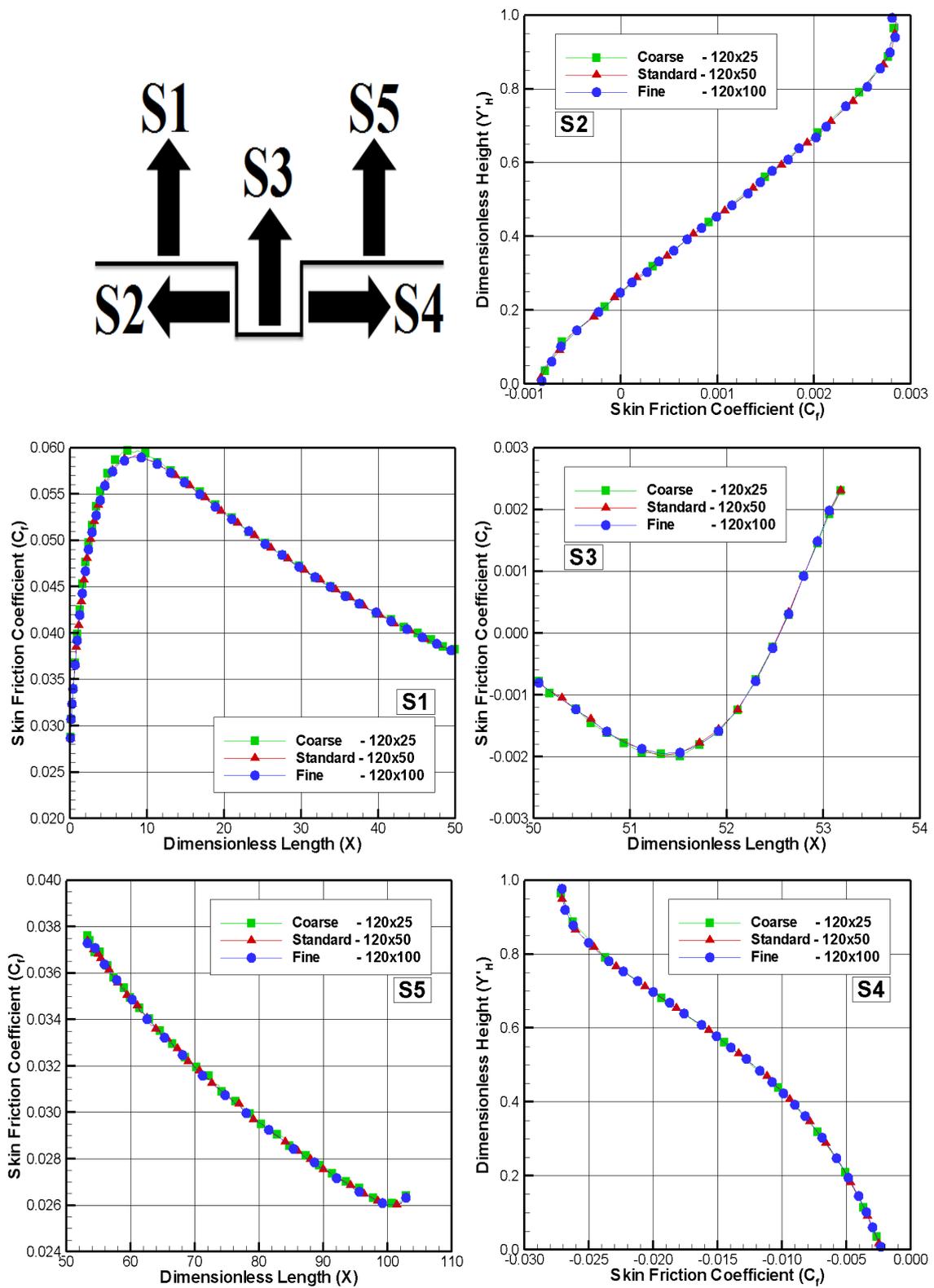
Figure 4.17 - Effect of variation in the cell size in the *y* direction in skin friction coefficient for *L/H*=1.
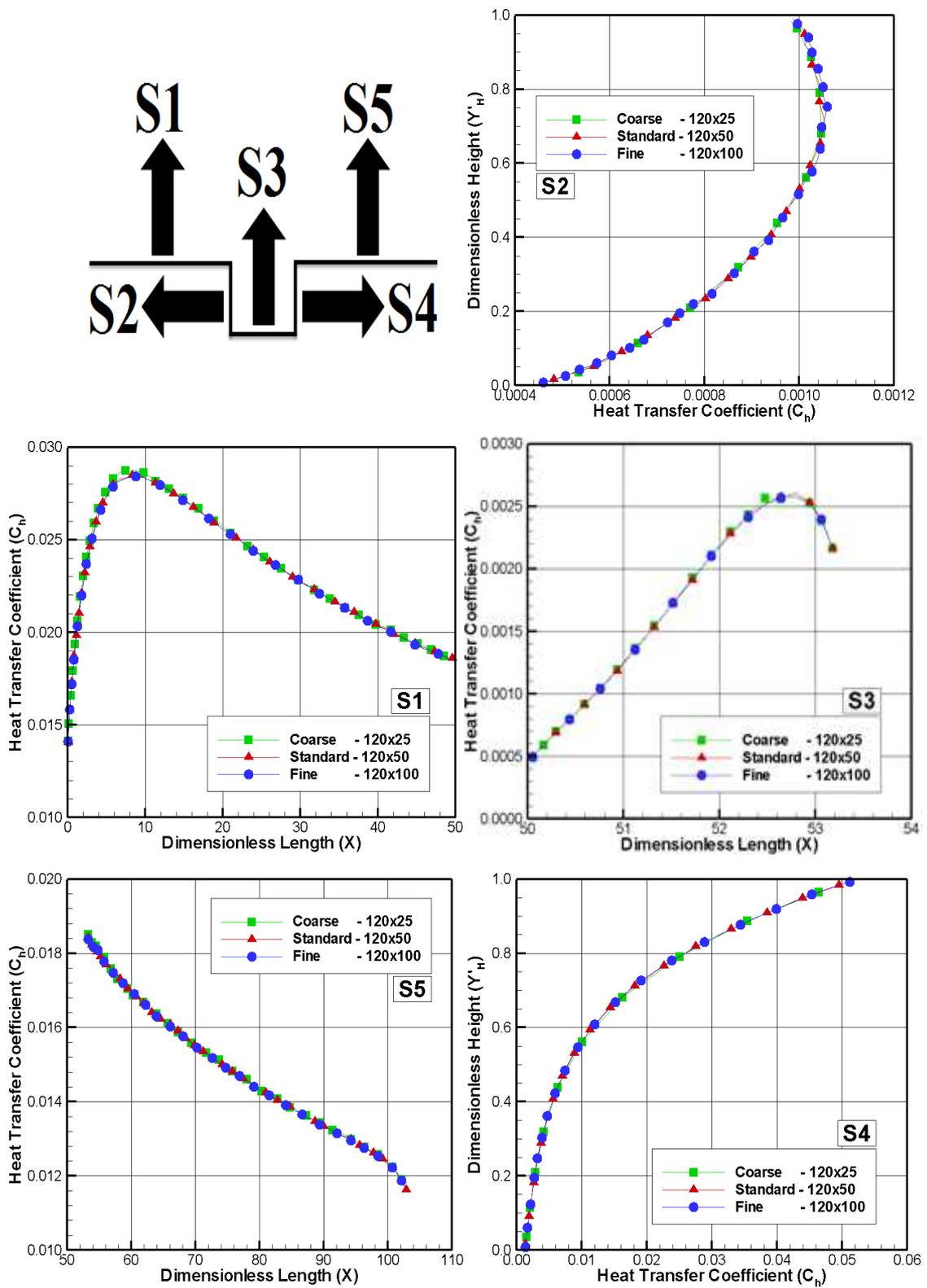
Figure 4.18 - Effect of variation in the cell size in the *y* direction in heat transfer coefficient for *L/H*=1.
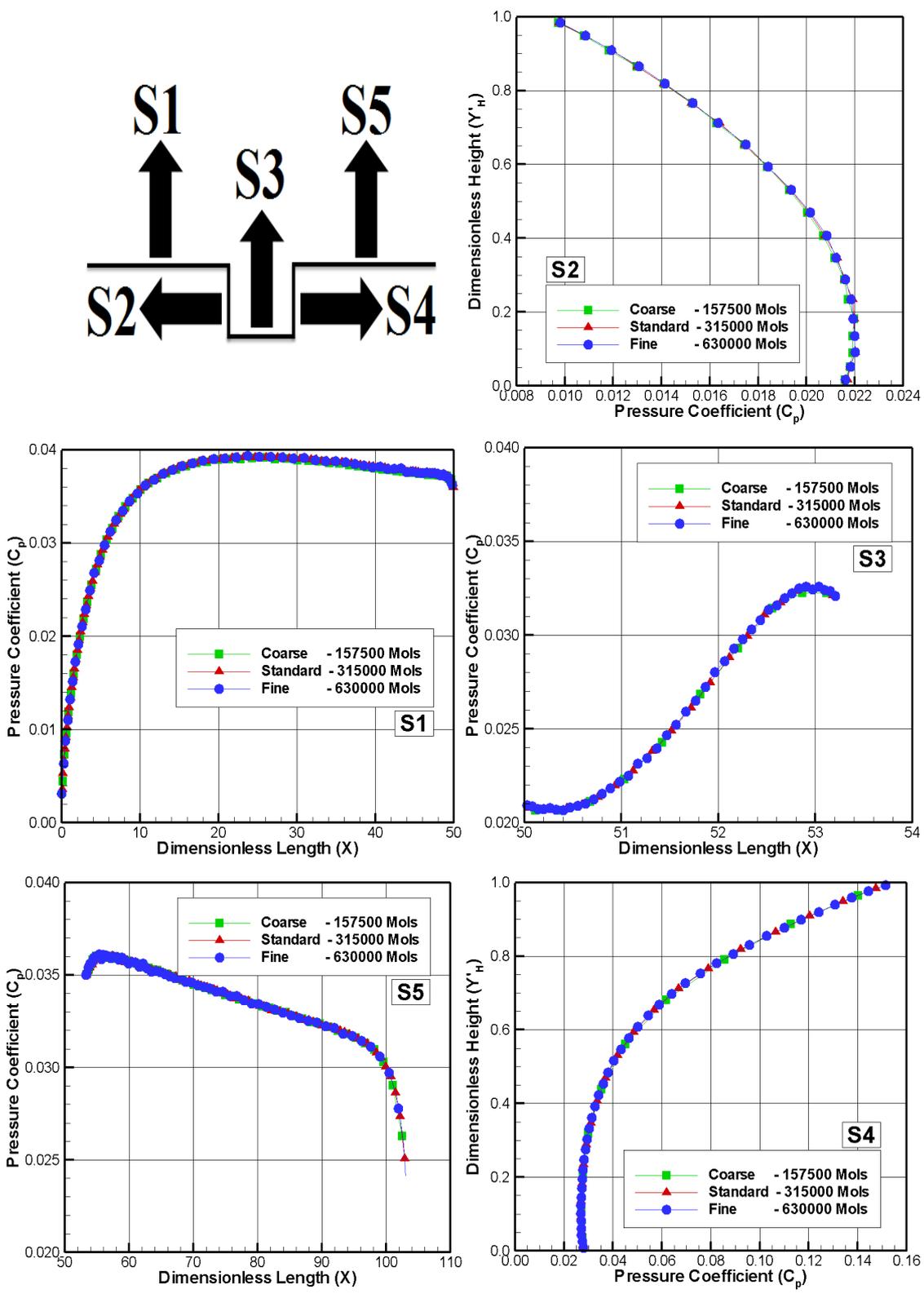
Figure 4.19 - Effect of variation in the number of molecules in the pressure coefficient for *L/H*=1.
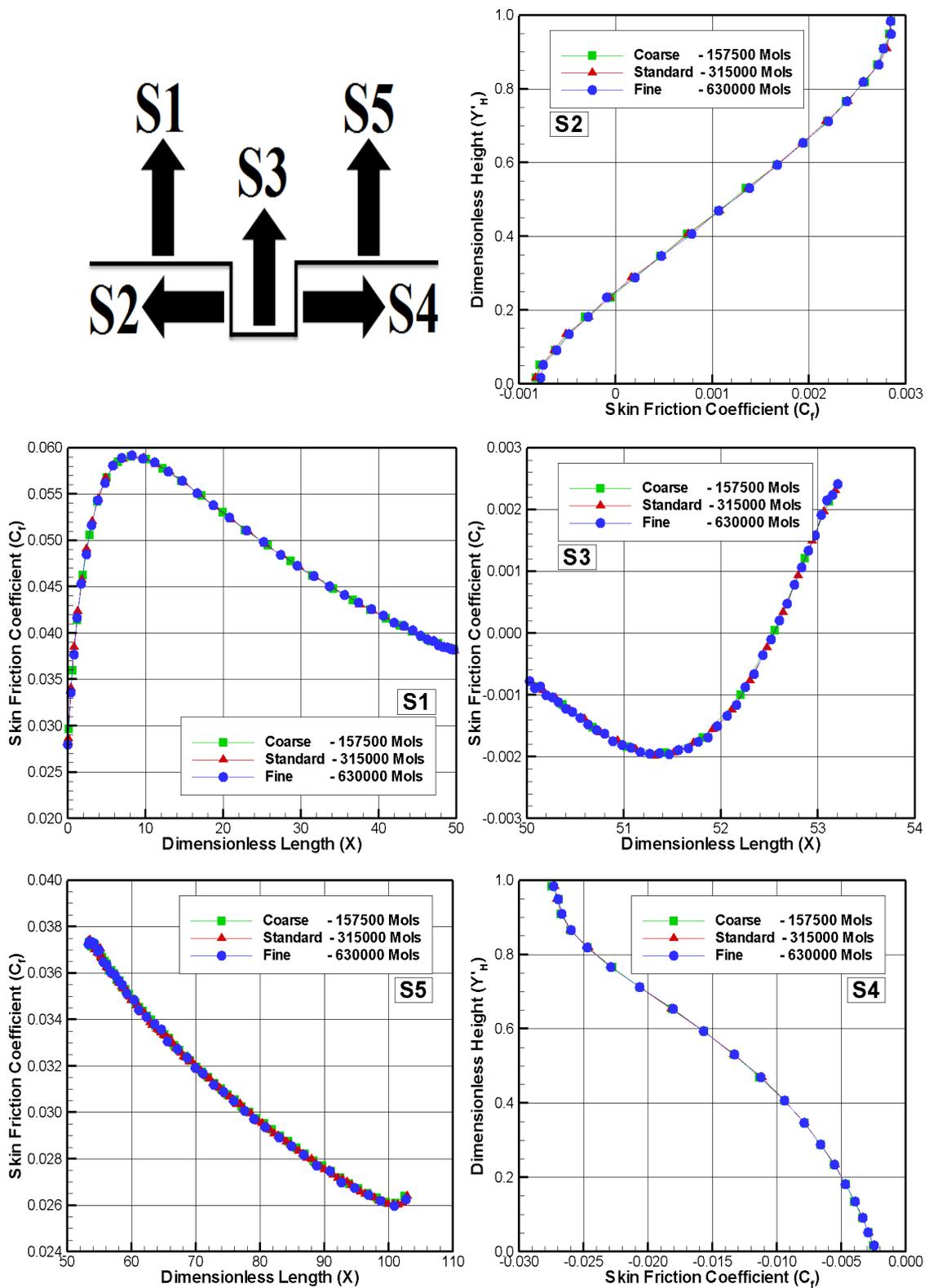
Figure 4.20 - Effect of variation in the number of molecules in the skin friction coefficient for *L/H*=1.
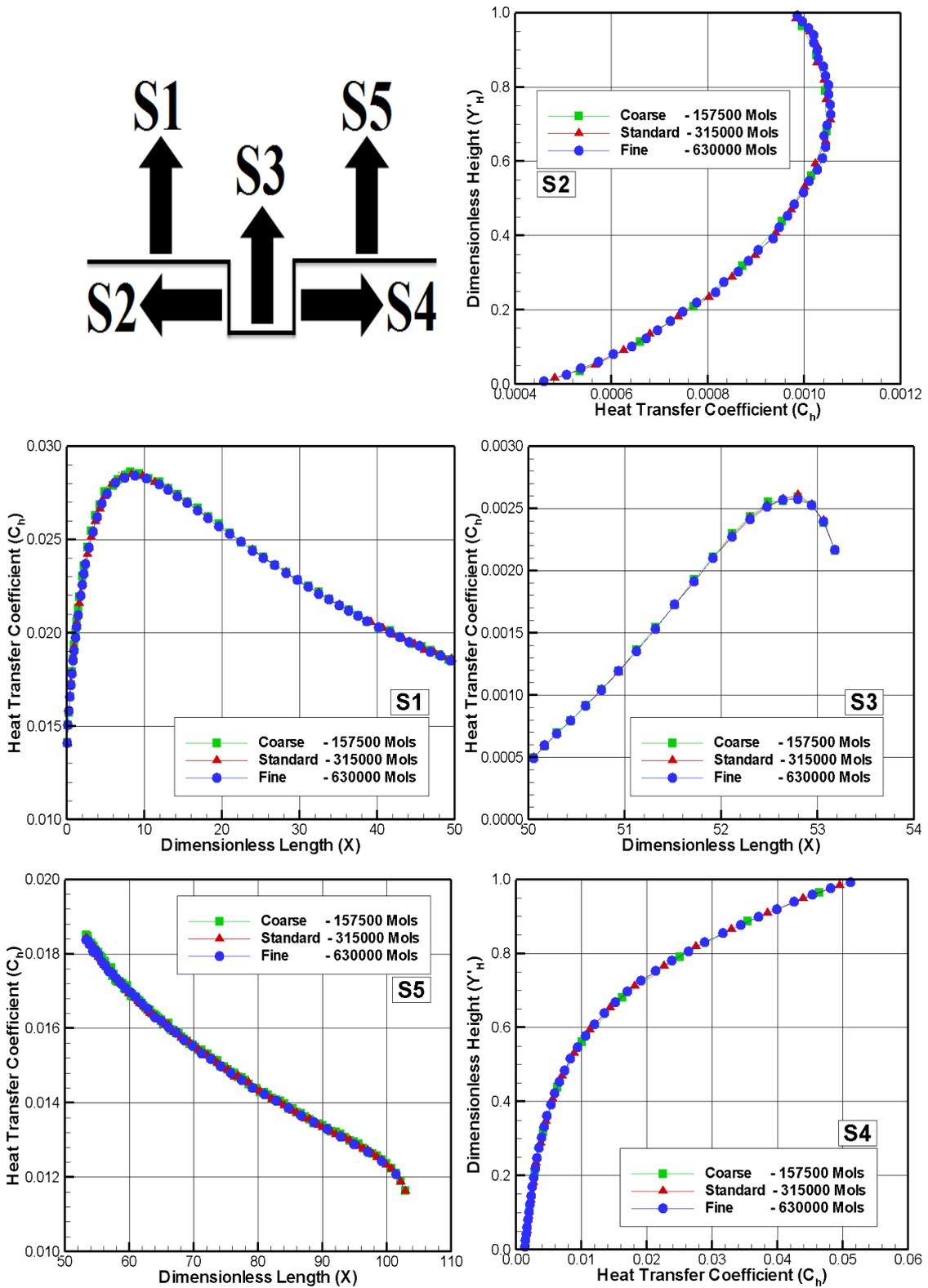
Figure 4.21 - Effect of variation in the number of molecules in the heat transfer coefficient for *L/H*=1.

5. COMPUTATIONAL RESULTS AND DISCUSSION

Having computed flowfield properties over a wide range of simulation parameters, it proves instructive to summarize the major features of the results. In this fashion, the purpose of this Chapter is to discuss and to compare differences in the flowfield structure as well as in the aerodynamic surface quantities due to variations in the gap L/H ratio.

5.1 Flowfield Structure

This section focuses on the calculations of the primary properties obtained from the DSMC results. The primary properties of particular interest in this dissertation are velocity, density, pressure and kinetic temperatures.

5.1.1 Velocity Field

In the DSMC method, the macroscopic properties are computed as averages from the microscopic properties in each cell in the computational domain. As a result, the velocity vector is given by the following expression,

$$\vec{c_0} = \frac{\sum_{j=1}^{N} m_j \vec{c_j}}{\sum_{j=1}^{N} m_j} \tag{5.1}$$

where N, m and $\vec{c_j}$ represent, respectively, the number of molecules, mass, and the velocity vector of the molecules in each cell.

It is important to mention that the mean molecular velocity $\bar{\vec{c}}(\equiv \vec{c}_0 = u\vec{\imath} + v\vec{\jmath} + w\vec{k})$ defines the macroscopic mean velocity. In addition, the velocity of the molecules relative to the macroscopic mean velocity, defined by thermal or peculiar velocity, is denoted by $\vec{c}' \equiv \vec{c} - \vec{c}_0$.

Tangential velocity profiles outside the gaps are illustrated in Figure 5.1 for five sections as a function of the *L/H* ratio. In this set of plots, the tangential velocity *u* is normalized by the freestream velocity U_∞, $X_L^{'}$ represents the distance $(x$-L_u-$L/2)$ normalized by the gap length *L*, and *Y* refers to the height *y* normalized by the freestream mean free path λ_∞. In addition, for comparison purpose, the tangential velocity ratio profiles for the flat-plate case without a gap are presented in the same plots.

According to Figure 5.1, it is observed that, at $Y \approx 0$, i.e., at the SR line, the tangential velocity profiles for the gaps are slightly different from those for a flat-plate case at sections defined by $X_L^{'}$ of -0.25, 0, and 0.25. It is also observed that this difference is confined in a region of one freestream mean free path above the SR line. In addition, as $Y \rightarrow \infty$, the tangential velocity *u* is not affected anymore for the presence of the gaps, since there are no differences in the profiles with increasing the *L/H* ratio. Furthermore, the tangential velocity *u* increases significantly and tends to the freestream velocity U_∞ at the vicinity of the upper boundary of the computational domain.

Still referring to Figure 5.1, it is noted that, for sections $X_L^{'}$ of -1 and 1, the tangential velocity profiles for the gaps are identical to those for the flat-plate case, indicating that the presence of the gaps does not influence the flowfield far upstream and downstream the gaps. This domain of influence is confined in a region smaller than a half-gap length, i.e., smaller than *L/2*. Particular attention is paid to the magnitude of the velocity at $Y = 0$ for sections $X_L^{'}$ of -1 and 1. It is clearly noted that the velocity ratio is not zero at the wall, there is a velocity slip, a characteristic of a rarefied flow. As a result, the condition $u/U_\infty = 0$ does not apply in a rarefied flow at the wall.

Another interesting characteristic in these plots is the similarity of the velocity profiles along the body surface. This is an indication that the velocity profiles may be expressed in terms of functions that, in appropriate coordinates, may be independent of one of the coordinate directions. However, no attempts have been done to find such functions.

Tangential velocity profiles inside the gaps are demonstrated in Figure 5.2 for three sections parameterized by the L/H ratio. In this set of diagrams, the left-column diagrams correspond to u/U_∞ as a function of the dimensionless height Y, i.e., the height y normalized by the freestream mean free path λ_∞, and the right-column diagrams correspond to u/U_∞ as a function of the dimensionless height Y'_H, i.e., the height $(y+H)$ normalized by the gap depth H.

Normal velocity profiles inside the gaps are displayed in Figure 5.3 for three sections as a function of the streamwise distance X'_L and parameterized by the L/H ratio. In this set of diagrams, the normal velocity v is normalized by the freestream velocity U_∞, and the three sections correspond to the transversal sections defined by the dimensionless height Y'_H of 0.25, 0.50, and 0.75. According to these plots, near the gap back face, $X'_L \approx$ -0.4, the normal velocity ratio profiles present positive values for the $L/H > 1/2$ cases, meaning that the flow is moving upward. Conversely, at the vicinity of the gap frontal face, $X'_L \approx 0.4$, the normal velocity ratio profiles present negative values, indicating that the flow is moving downward. Therefore, based on the two opposite behaviors for the normal velocity ratio, it may be inferred in passing by the way that there is a region of clockwise circulating flow. In addition, of particular interest is the behavior of the normal velocity profiles for the $L/H < 1/2$ cases near the bottom surface of the gaps, i.e., $Y'_H = 0.25$. It is quite apparent that the v-velocity component is zero, indicating that there is no a recirculation region at the vicinity of the gap floor for these cases.
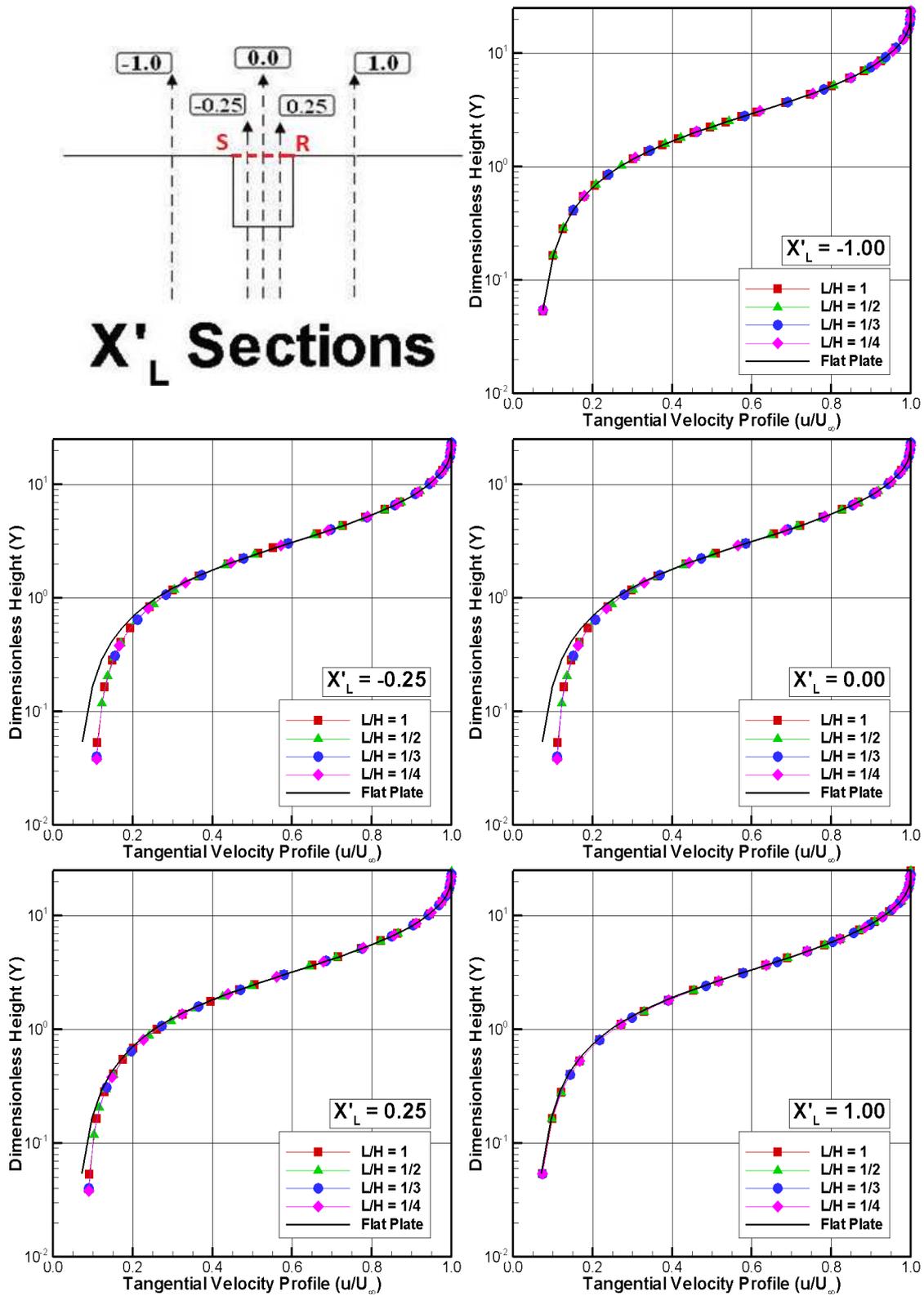
Figure 5.1 - Tangential velocity ratio (u/U_∞) profiles outside the gaps for five sections parameterized by the L/H ratio.

80
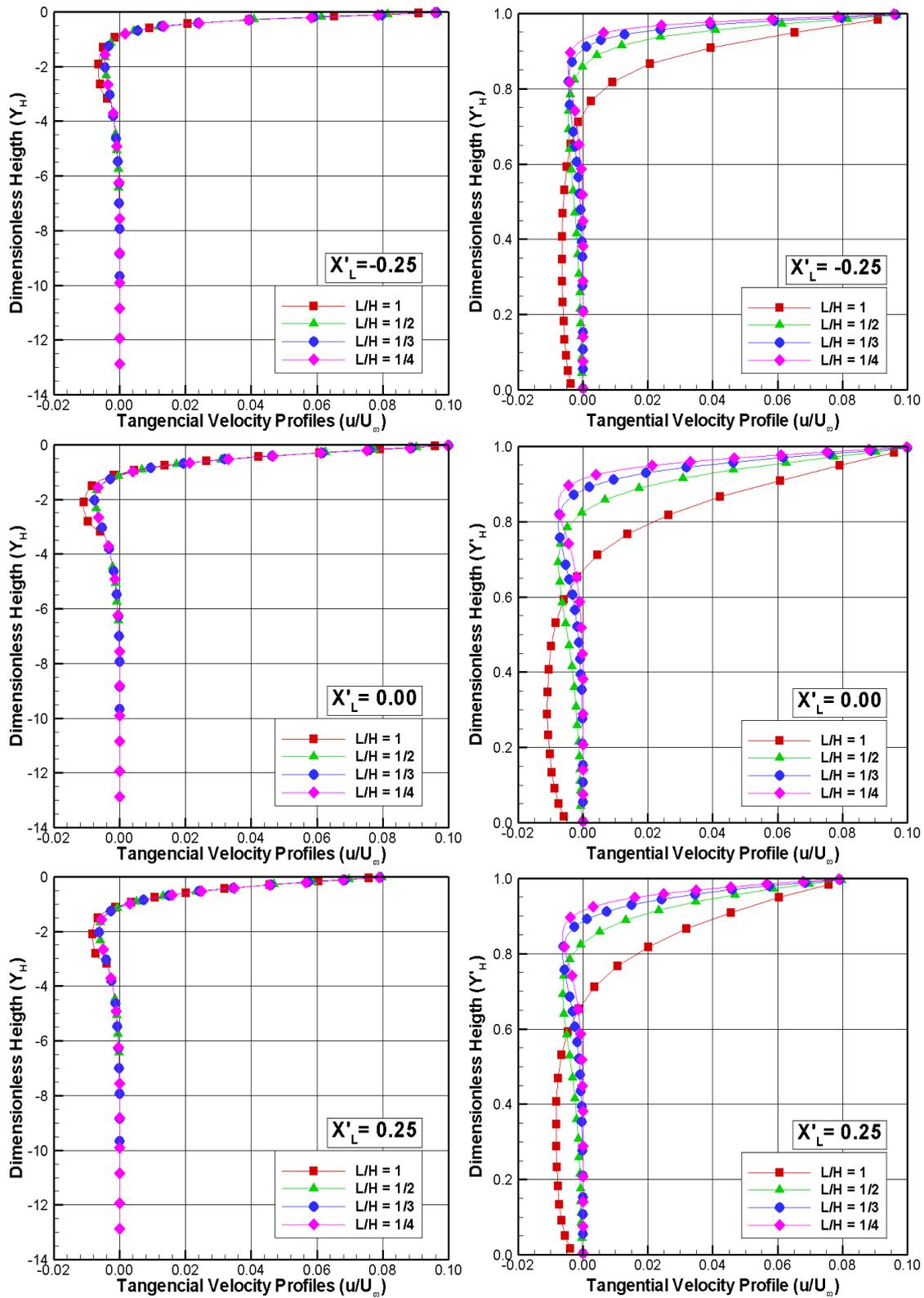
Figure 5.2 - Tangential velocity ratio (u/U_∞) profiles inside the gaps for three sections as a function of the dimensionless heights Y (left column) and Y'_H (right column).

At this point, it is worth taking a closer look at the recirculation region. In this manner, streamline traces inside the gaps are depicted in Figure 5.4. In this set of diagrams, the *L/H* ratio decreases from 1 (left side) to 1/4 (right side). Based on Figure 5.4, it is clearly noticed that the flow within the gaps is characterized by a primary vortex system. For the *L/H* = 1 and 1/2 cases, it is noteworthy that the recirculation region fills the entire gaps. Conversely, for the *L/H* = 1/3 and 1/4 cases, the recirculation region does not fill the entire gaps. In addition, as expected, the external stream does not reattach the bottom surface of the gaps. Moreover, it should be mentioned that the gap flow topology observed here in a rarefied environment differs from that usually observed in the continuum flow regime, as showed in Chapter 1.

Finally, in an effort to emphasize points of interest related to the velocity field, Figure 5.5 displays contour maps for the distribution of Mach number in the entire computational domain. In this family of plots, dimensionless height *Y* stands for the height *y* normalized by the freestream mean free path λ_∞, and the dimensionless length *X* refers to the length *x* also normalized by the λ_∞. Also, the plots in the left column represent the Mach number in the entire computational domain, and the plots in the right column correspond to a magnified view of the Mach distribution inside the gaps. According to the plots in the right column, it is firmly established that the Mach number at the vicinity of the back-face corner is larger than that at the vicinity of the frontal-face corner, as a result of the flow separation and flow reattachment on these faces.
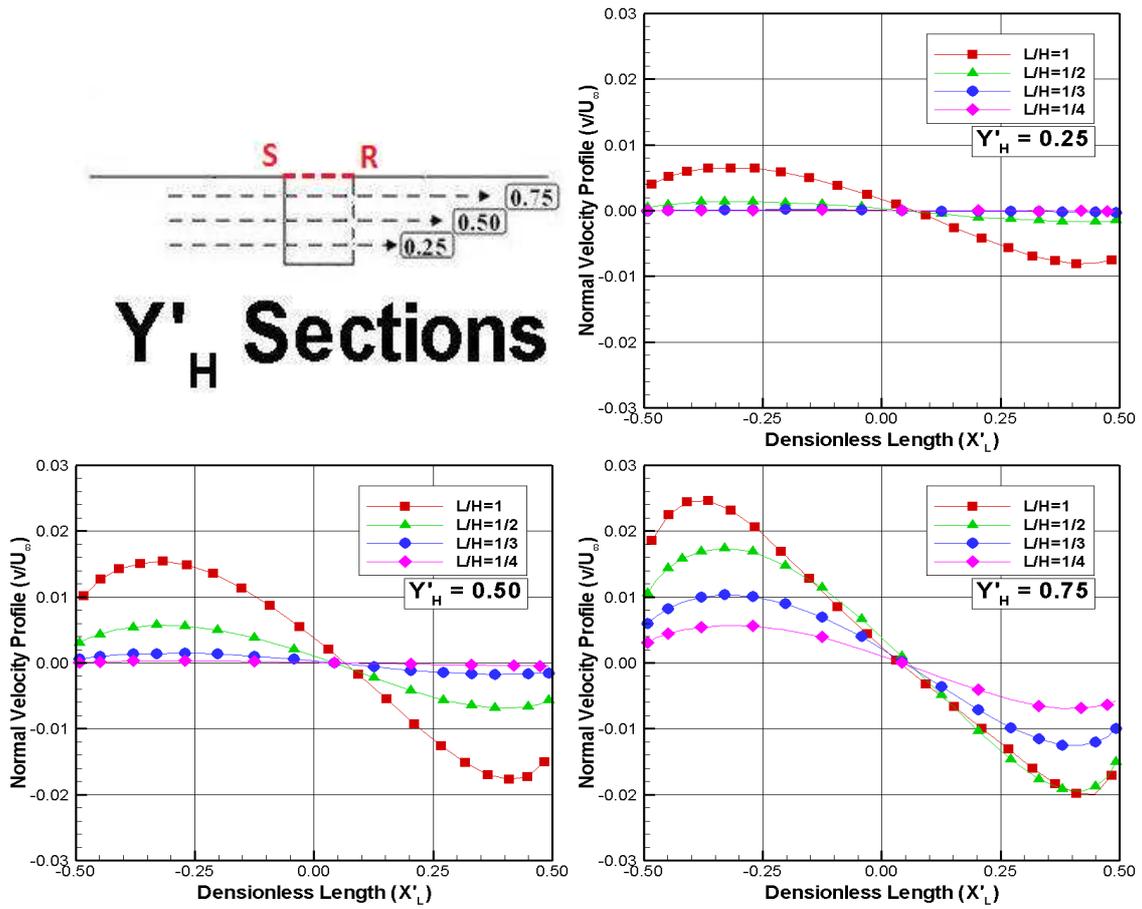
Figure 5.3 - Normal velocity ratio (v/U_∞) profiles inside the gaps for three transversal sections as a function of the dimensionless length X'_L.
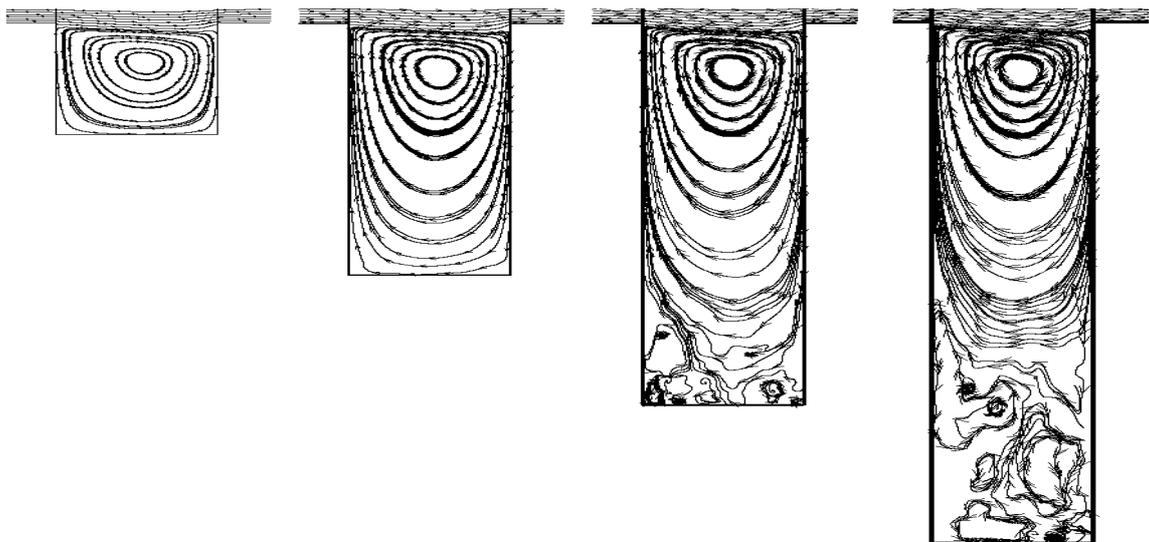
Figure 5.4 - Distribution of streamline traces inside the gaps for *L/H* of 1 (left), 1/2, 1/3 and 1/4 (right).

83
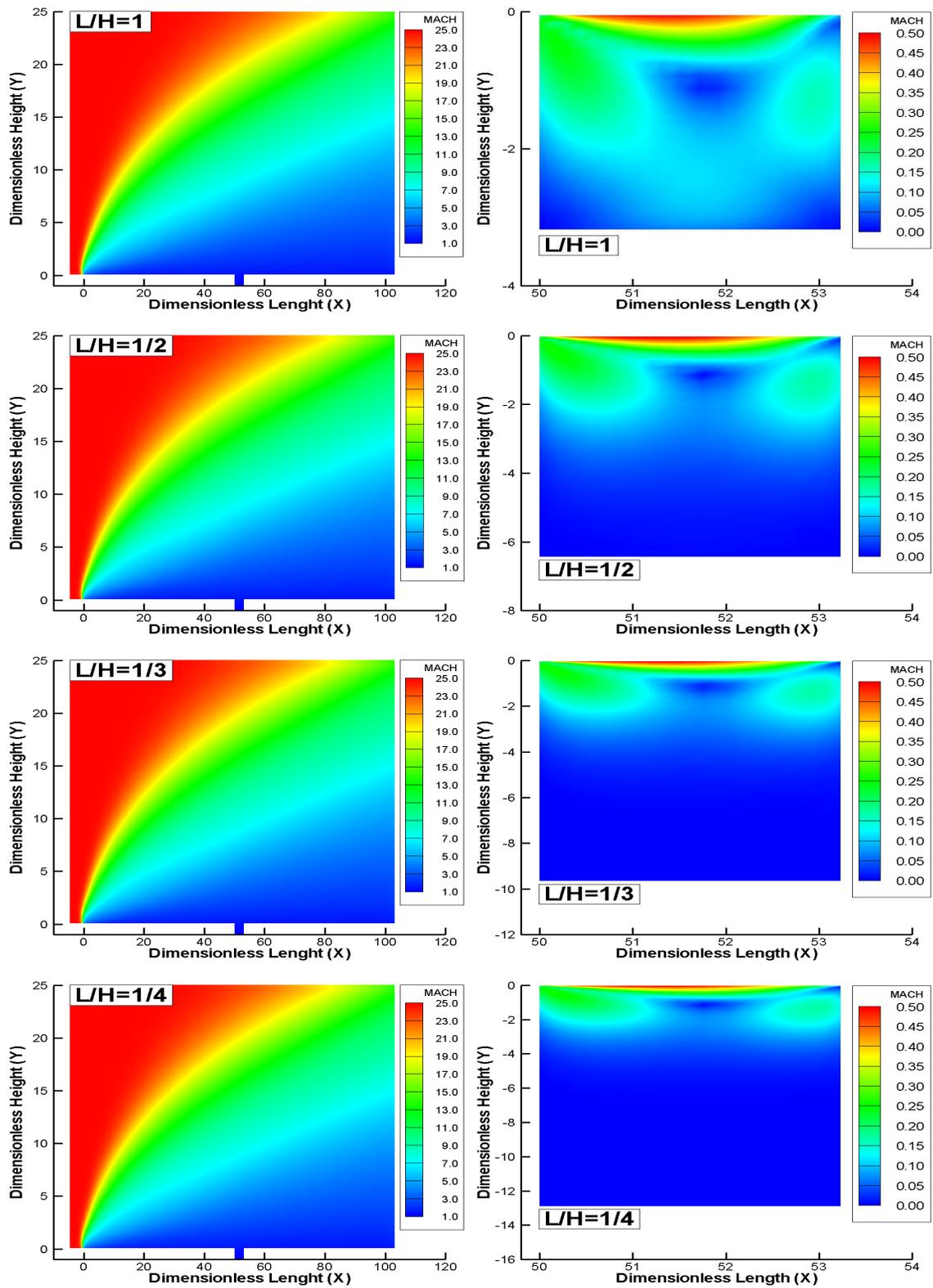
Figure 5.5 - Mach number distribution outside (left) and inside (right) the gaps for *L/H* ratio of 1, 1/2, 1/3 and 1/4.

5.1.2 Density Field

The density in each cell in the computational domain is obtained by the following expression,

$$\bar{\rho} = \frac{1}{NV_c} \sum_{j}^{N} m_j \tag{5.2}$$

where N is the number of molecules in the cell, m is the mass of the molecules, and V_c is the volume of the cell.

The impact on the density profiles outside the gaps due to changes on the L/H ratio is illustrated in Figure 5.6 for five sections. In this group of plots, density ρ is normalized by the freestream density ρ_∞, X_L' and Y are dimensionless length and height, respectively, as defined previously in the velocity ratio profiles. Besides, as a base of comparison, density ratio profiles for the flap-plate case are presented in the same plots.

According to Figure 5.6, it is observed that the density ratio experiences significant changes in the direction perpendicular to the SR line as the flow moves downstream along the surface. The density ratio is high adjacent to the SR line, $Y \approx 0$, and rapidly decreases inside a layer of thickness around two to three freestream mean free paths, where the density ratio is less than one. It means that the density ρ is smaller than the freestream density ρ_∞. This characteristic is observed when the body surface is very much colder than the stagnation temperature of the oncoming gas. As a result, the gas near the body surface tends to be much denser and cooler (see next sections) than the gas in the rest of the boundary layer. As Y increases, the density ratio increases significantly at a maximum value, around $\rho/\rho_\infty \approx 1.6$, inside the shock wave. After that, the density decreases and reaches the freestream density value as $Y \to \infty$.

85

Still referring to Figure 5.6, it is noticed that, for section $X_L' = -1$, density ratio profiles for the gaps are identical to those for the flat-plate case, indicating that the presence of the gaps does not influence the flowfield far upstream. In contrast, for section $X_L' = 1$, density ratio profiles for the gaps are slightly different from that for the flat-plate case, indicating that the presence of the gaps is still felt at least a half-gap length downstream the gaps. Particular attention is paid to the density ratio at $Y \approx 0$ for the sections X_L' of -0.25, 0, and 0.25. It is noticed that the density ratio significantly decreased in the range $-1 \leq X_L' \leq -0.25$, due to the flow expansion around the gap back face, and increased in the range $-0.25 \leq X_L' \leq 1$ because of the flow compression around the gap frontal face.

Effects of the *L/H* ratio on density ratio profiles inside the gaps are displayed in Figure 5.7 for three sections defined by X_L' of -0.25, 0, and 0.25. In this set of plots, similar to the tangential velocity profiles, the left-column plots correspond to ρ/ρ_∞ as a function of the dimensionless height Y, i.e., the height y normalized by the freestream mean free path λ_∞, and the right-column plots correspond to ρ/ρ_∞ as a function of the dimensionless height Y_H', i.e., the height $(y+H)$ normalized by the gap depth H. Based on these plots, it may be recognized that the density ratio inside the gap increases from the SR line to the bottom of the gaps for the *L/H* ratio investigated. It is quite apparent that the density ratio tends to a constant value at the bottom of the gap with decreasing the *L/H* ratio.

Finally, in attempting to bring out the essential features of the density behavior in the gaps, Figure 5.8 illustrates contour maps for the density ratio distribution in the entire computational domain. In this group of plots, similar to the Mach number distribution, dimensionless height Y stands for the height y normalized by the freestream mean free path λ_∞, and the dimensionless length X refers to the length x also normalized by the λ_∞. Furthermore, the plots in the left column represent the density ratio in the entire computational domain, and the plots in the right column correspond to a magnified view of the density ratio distribution inside the gaps. Looking first to the plots in the left column, it is observed that, in general, the density ratio distribution follows that

presented by a flat-plate. Turning to the plots in the right column, it noticed that the density ratio is low at the vicinity of the back-face corner, due to the flow expansion, and it is high at the frontal-face corner, because of the flow compression region. It is also observed that the density ρ is, at least, twice the freestream density ρ_∞ at the bottom surface of the gaps, for the *L/H* ratio investigated.
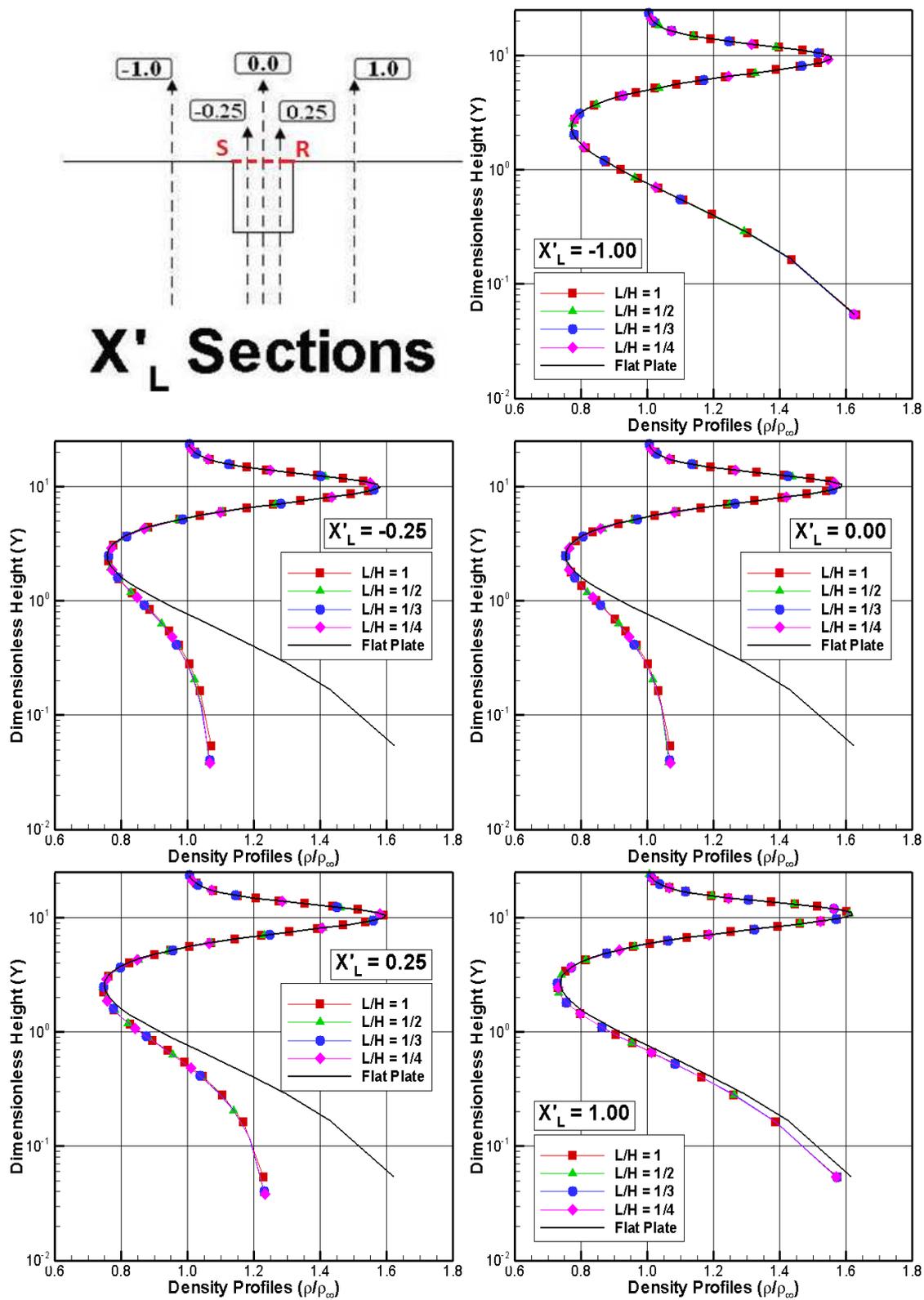
Figure 5.6 - Density ratio (ρ/ρ_∞) profiles outside the gaps for five sections parameterized by the *L/H* ratio.

88
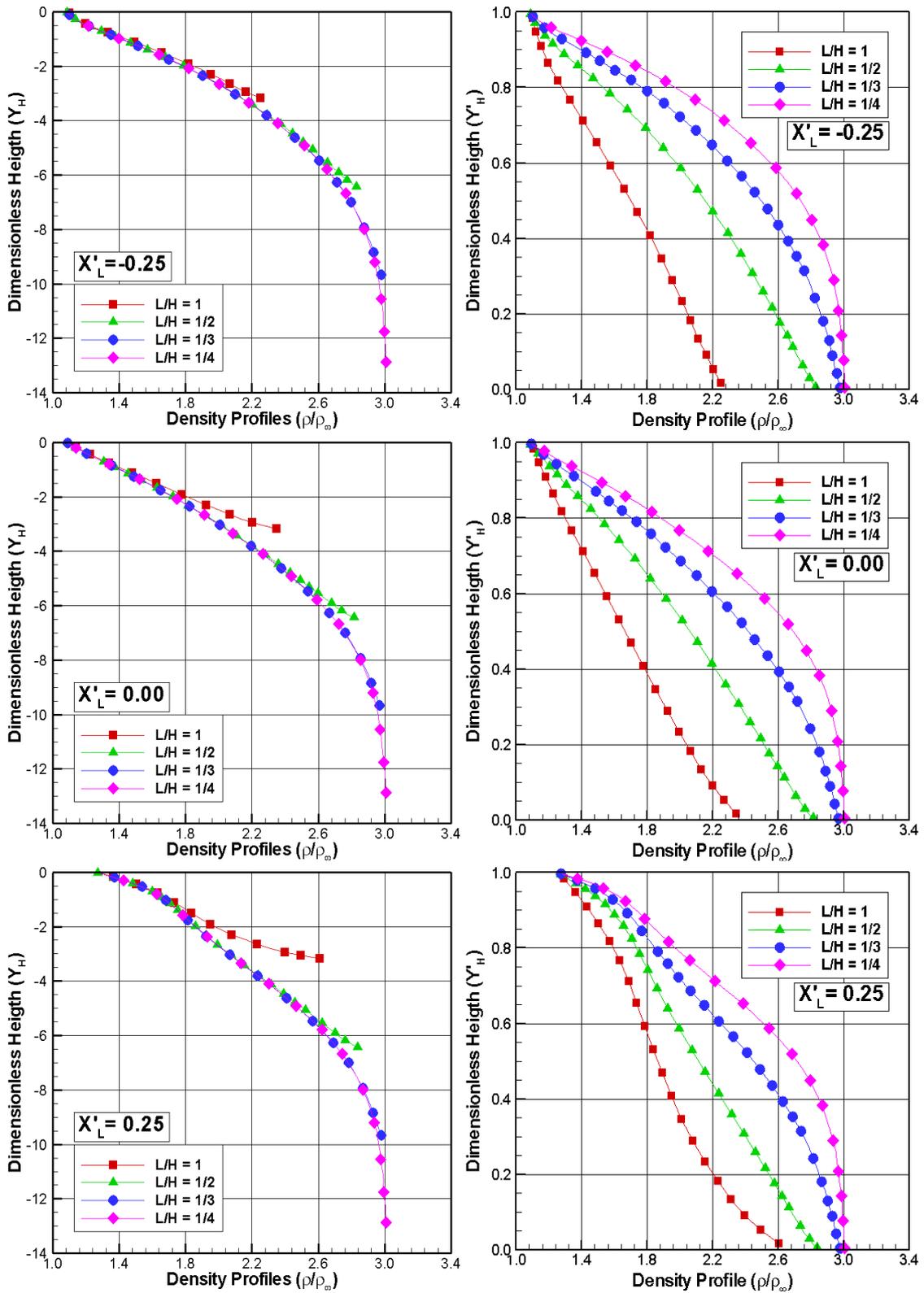
Figure 5.7 - Density ratio (ρ/ρ_∞) profiles inside the gaps for three sections as a function of the dimensionless heights Y (left column) and Y'_H (right column).

89
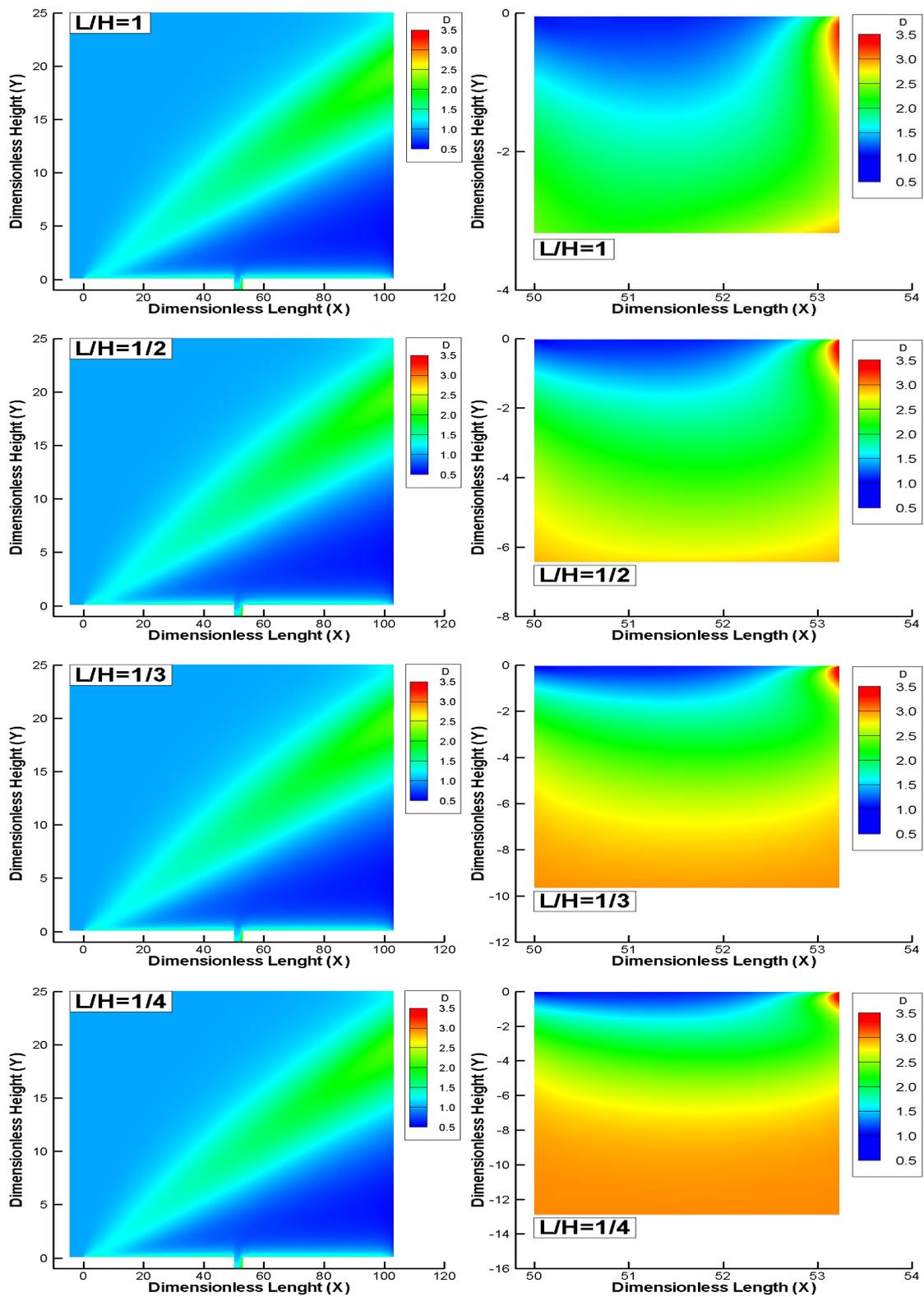
Figure 5.8 - Density ratio (ρ/ρ_∞) distribution outside (left) and inside (right) the gaps for *L/H* ratio of 1, 1/2, 1/3 and 1/4.

5.1.3 Pressure Field

The pressure in each cell inside the computational domain is obtained by the following equation,

$$\bar{p} = \frac{1}{3V_c} \sum_{j=1}^{N} \frac{(mc'^2)_j}{N} \tag{5.3}$$

where, N is the number of molecules in the cell, m is the mass of the molecules, V_c is the volume of the cell, and c' is the thermal velocity of the molecules.

The influence of the *L/H* ratio on pressure profiles outside the gaps is exhibited in Figure 5.9 for five sections. In this set of diagrams, pressure p is normalized by the freestream pressure p_∞, X'_L and Y are dimensionless variables as defined previously in the density ratio profiles. Moreover, for comparative purpose, pressure ratio profiles for the flat-plate case are also exhibited in the same diagrams.

According to this set of diagrams, it is noticed that pressure ratio profiles follow a similar behavior as compared to those presented by tangential velocity ratio and density ratio profiles in the sense that they differ from those for the flat-plate case in a small region above the SR line. Beyond of this small region, the pressure ratio continues to increase to a maximum value inside the shock wave that formed at the sharp leading edge of the flat-plate. After that, the pressure dramatically decreases, outside the shock wave, and reaches the freestream pressure value at the boundary of the computational domain.

Still referring to Figure 5.9, it should be remarked that no visible changes are observed in the pressure profiles for the *L/H* ratio investigated. Nevertheless, a feature of particular interest is related to the pressure ratio profiles for sections defined by X'_L of -0.25 and 0.25. At $X'_L = -0.25$, the pressure ratio for the gaps is lower than that for the

91

flat-plate case in a region defined by one freestream mean free path above the SR line. Conversely, at X'_L = 0.25, it is larger than that for the flat-plate case. This is explained by the fact that, at the vicinity of the back face, X'_L = -0.25, the flow experiences an expansion. On the other hand, at the vicinity of the frontal face, X'_L = 0.25, the flow experiences a compression.

Effects of the *L/H* ratio on pressure ratio profiles inside the gaps are demonstrated in Figure 5.10 for three sections defined by X'_L of -0.25, 0, and 0.25. In this group of plots, similar to the tangential velocity profiles, the left-column plots correspond to p/p_∞ as a function of the dimensionless height *Y*, and the right-column plots correspond to p/p_∞ as a function of the dimensionless height Y'_H. According to these plots, it is very encouraging to observe that the pressure ratio inside the gaps decreases from the SR line to the bottom of the gaps for the *L/H* ratio investigated. However, similar to the density ratio, the pressure ratio tends to a constant value at the bottom of the gaps with decreasing the *L/H* ratio. Moreover, as indeed is clear from these plots, at the bottom of the gaps, the pressure *p* is one order of magnitude larger than the freestream pressure p_∞.

In the following, it is desirable to present contour maps for the pressure ratio in the entire computational domain. In this fashion, Figure 5.11 depicts the pressure ratio distribution in the entire computational domain (left column) as well as a magnified view of the pressure ratio inside the gaps (right column). In this set of plots, dimensionless height and length, *Y* and *X*, respectively, are similar to those defined in the density ratio contours.

According to this set of plots, at the vicinity of the sharp leading edge of the flat-plate, pressure is almost two orders of magnitude larger than the freestream pressure. The reason for that is because of the large amount of kinetic energy present in a hypersonic freestream. This energy is converted by molecular collisions into high thermal energy surrounding the body and by flow work into increased pressure. Inside the gaps, it is very encouraging to observe that the maximum pressure ratio takes place at the corner

of the frontal face, i.e., pressure p is thirty times the freestream pressure p_∞. It should be remarked that this pressure ratio is three times the pressure ratio observed at the bottom of the gaps, for the *L/H* ratio investigated. As a result, it may be inferred in passing that particular attention should be paid to the gap frontal face in terms of the pressure loads, since the vicinity of the corner represents a zone of strong compression.
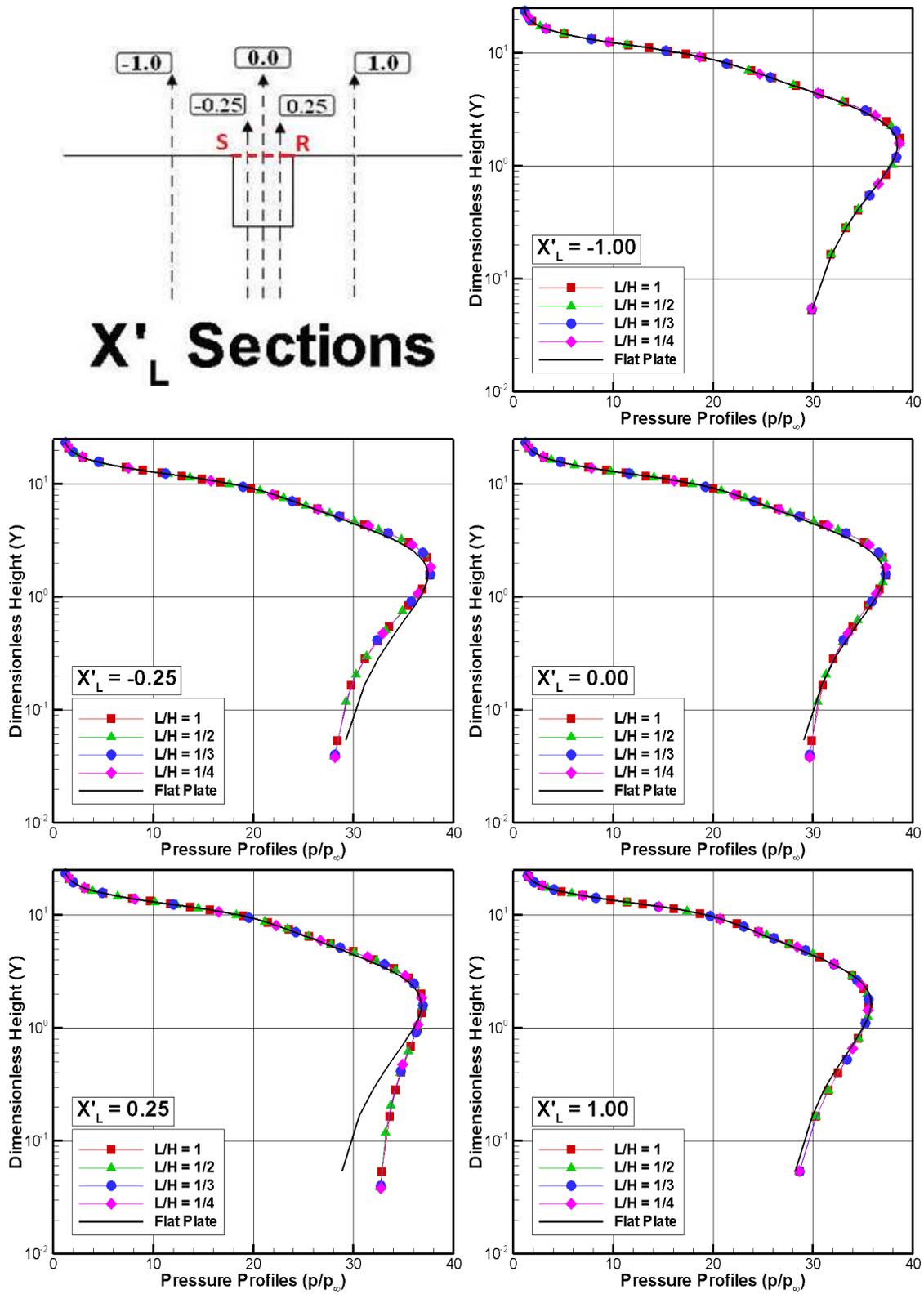
Figure 5.9 - Pressure ratio (p/p_∞) profiles for five sections outside the gap parameterized by the *L/H* ratio.
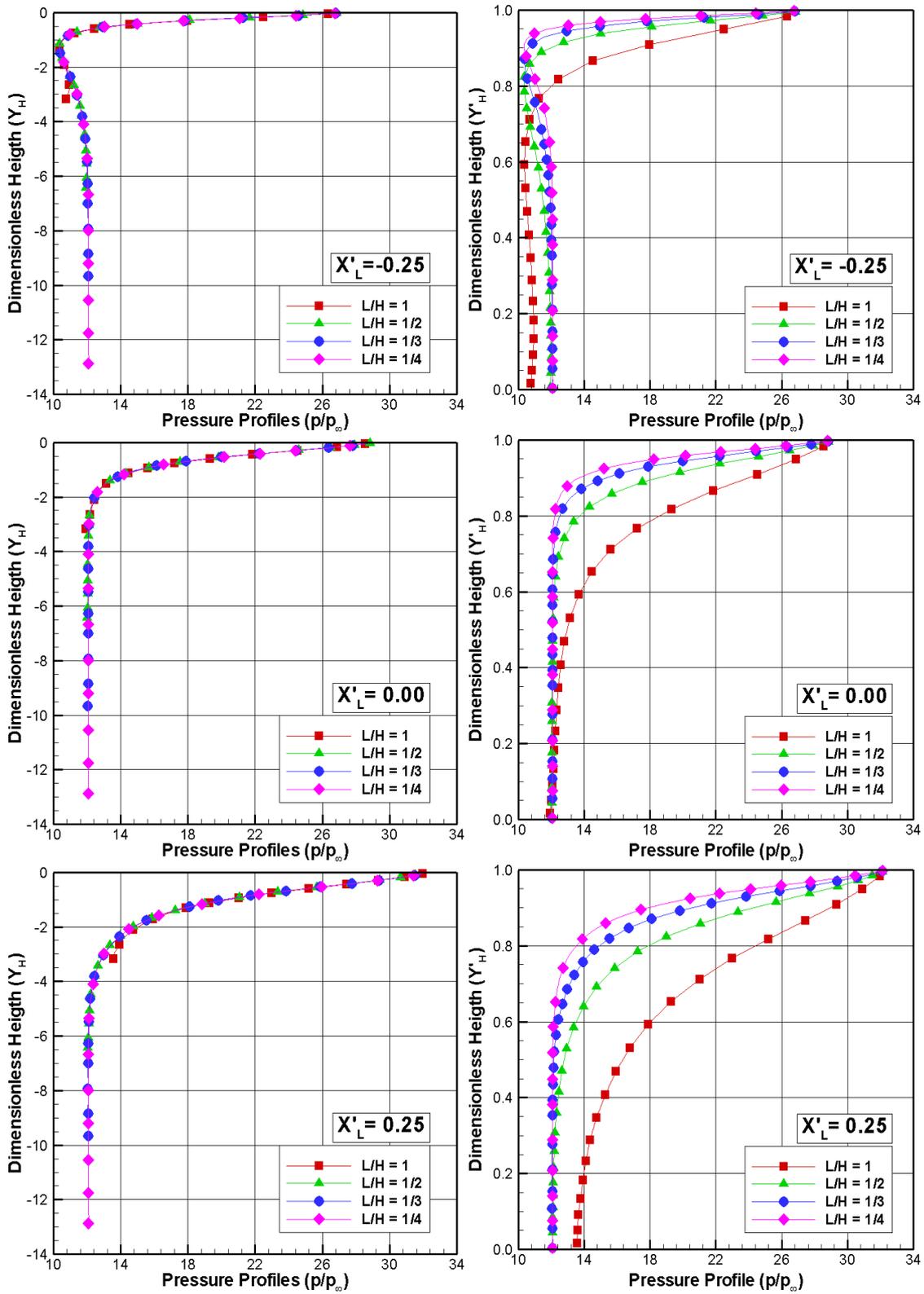
Figure 5.10 - Pressure ratio (p/p_∞) profiles for three sections inside the gap as a function of the dimensionless heights Y (left column) and Y'_H (right column).
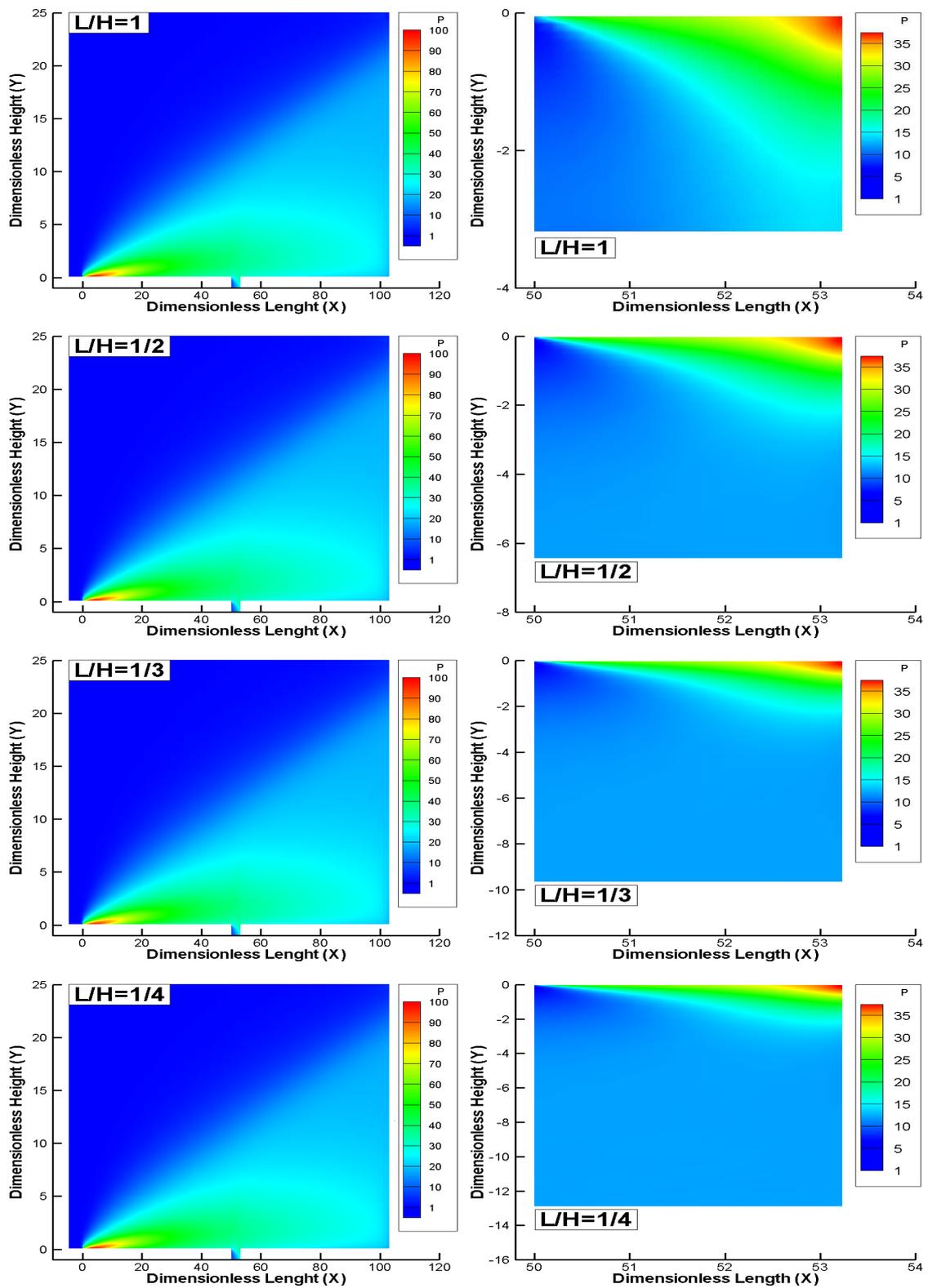
Figure 5.11 - Pressure ratio (p/p_∞) distribution outside (left) and inside (right) the gaps for *L/H* ratio of 1, 1/2, 1/3 and 1/4.

5.1.4   Kinetic Temperature Field

In a diatomic or polyatomic gas in complete thermodynamic equilibrium, the translational temperature is equal to the temperature related to the internal modes, i.e., rotational, vibrational, or electronic temperatures, and it is identified as thermodynamic temperature. When the equilibrium is disturbed, relaxation processes arise in the system that attempt to return it to the state of the total statistical equilibrium. In diatomic or polyatomic gas, there are processes which results in the establishment of equilibrium with respect to individual degrees of molecular freedom such as translational, rotational, vibrational or electronic. Conversely, in a thermodynamic non-equilibrium gas, an overall temperature is defined as the weighted mean of the translational and internal temperatures (BIRD, 1994) as being,

$$T_O = \frac{3T_T + \zeta_R T_R + \zeta_V T_V}{3 + \zeta_R + \zeta_V} \tag{5.4}$$

where T and ζ stand for the temperature and the degree of freedom, respectively, and subscripts T, R and V refer to translation, rotation and vibration, respectively.

Translational, rotational, and vibrational temperatures are obtained to each cell in the computational domain by the following equations,

$$\overline{T}_T = \frac{1}{3k} \sum_{j=1}^{N} \frac{(mc'^2)_j}{N} \tag{5.5}$$

$$\overline{T}_R = \frac{2}{k} \frac{\overline{\varepsilon}_R}{\zeta_R} \tag{5.6}$$

$$\overline{T}_V = \frac{\Theta_V}{\ln\left(1 + \frac{K\Theta_V}{\overline{\varepsilon}_V}\right)} \tag{5.7}$$

97

where k is the Boltzmann constant, Θ_V is the characteristic temperature of vibration, and $\overline{\varepsilon}_R$ and $\overline{\varepsilon}_V$ are, respectively, rotation and vibration average energies in each cell.

The *L/H* ratio effects on temperature profiles outside the gaps are illustrated in Figure 5.12 for five sections. In this group of plots, kinetic temperature ratio stands for the translational temperature T_T, rotational temperature T_R, vibrational temperature T_V, and overall temperature T_O normalized by the freestream temperature T_∞. X'_L and Y are dimensionless variables as defined previously in the pressure ratio profiles. Furthermore, profiles are only shown for *L/H* of 1 and 1/4. Results for *L/H* of 1/2 and 1/3 are intermediate and will not be shown.

Referring to Figure 5.12, it is clearly seen that thermodynamic non-equilibrium occurs outside the gaps, as shown by the lack of equilibrium between the translational and internal kinetic temperatures. As mentioned earlier, thermal non-equilibrium occurs when the temperatures associated with the translational, rotational, and vibrational modes of a polyatomic gas are different. It should be mentioned in this context that the overall temperature, defined by Equation (5.4), is equivalent to the thermodynamic temperature only under thermal equilibrium conditions. In addition, the ideal gas equation of state does not apply to this temperature in a non-equilibrium situation.

Still referring to Figure 5.12, it should be recognized that, in the undisturbed freestream far from the flat-plate, $Y \rightarrow \infty$, the translational and internal kinetic temperatures have the same value and are equal to the thermodynamic temperature. Approaching the flat-plate, $Y \approx 2$, the translational kinetic temperature rises to well above the rotational and vibrational temperatures and reaches a maximum value that is a function of the section X'_L. Since a large number of collisions is needed to excite molecules vibrationally from the ground state to the upper state, the vibrational temperature is seen to increase much more slowly than rotational temperature. Still further toward the flat-plate surface, $Y \approx 0$, the translational kinetic temperature decreases, and reaches a constant value on the

98

wall, sections X'_L = -1 and 1, that is above the wall temperature T_w ($\approx 4T_\infty$), resulting in a temperature jump as defined in continuum formulation (GUPTA et al., 1985). Furthermore, the difference between translational temperature and internal temperatures at the vicinity of the flat-plate surface also indicates that the thermodynamic equilibrium is not achieved in the boundary layer. Moreover, it should be emphasized that no visible changes are observed in the temperature ratio profiles due to variations on the L/H ratio, since L/H of 1 and 1/4 represent, respectively, the largest and the smallest values investigated.

Having a clear qualitative picture of the kinetic temperature ratio outside the gaps, it proves instructive to examine the differences in the kinetic temperature profiles as compared to those for a flat-plate without gaps. In doing so, Figure 5.13 illustrates this comparison for the same five sections outside the gaps. By the time being, the comparison is only based on the L/H = 1 case, since kinetic temperature ratio was not affected by the L/H ratio outside the gaps.

According to Figure 5.13, it is observed that, at $Y \approx 0$, i.e., at the SR line, the kinetic temperature ratio profiles for the gaps are different from those for a flat-plate case at sections defined by X'_L of -0.25, 0, and 0.25. It is also observed that this difference is confined in a region of two to three freestream mean free paths above the SR line. Nevertheless, for sections X'_L of -1 and 1, the kinetic temperature ratio profiles for the gaps are identical to those for the flat-plate case, indicating that the presence of the gaps does not affect the flowfield far upstream and downstream the gaps. Similar to the other primary properties, the domain of influence is confined in a region smaller than a half-gap length, i.e., smaller than $L/2$.

Proceeding in a manner analogous to the pevious primary properties, effects of the L/H ratio on temperature ratio profiles inside the gaps are demonstrated in Figure 5.14 for three sections defined by X'_L of -0.25, 0, and 0.25. Again, in this group of plots, the left-column plots correspond to T/T_∞ as a function of the dimensionless height Y, and the

right-column plots correspond to T/T_∞ as a function of the dimensionless height Y_H'. Also, filled and empty symbols stand for L/H of 1 and 1/4, respectively. Results for L/H of 1/2 and 1/3 are intermediate and will not be shown. According to this set of plots, it is apparent that the kinetic temperature ratio T/T_∞ decreases and reaches a constant value on the bottom surface, which corresponds to the wall temperature T_w ($\approx 4T_\infty$). At the bottom surface, it is seen that the flow is thermal equilibrium, once the internal temperatures are equal to the translational temperature. It is important to recall that, the density increased at the vicinity of the gap bottom surface, as shown in Figure 5.7 and 5.9. Consequently, the local mean free path decreased and the mean collision frequency increased and, therefore, the flow reached the thermal equilibrium.

In what follows, it is important to demonstrate contour maps for the translational temperature ratio in the entire computational domain. In this sense, Figure 5.15 illustrates the translational temperature ratio distribution in the entire computational domain (left column) as well as a magnified view of the translational temperature ratio inside the gaps (right column). In this family of plots, dimensionless height and length, Y and X, respectively, are similar to those defined in the pressure ratio contours. Moreover, attention should be paid to the different temperature ratio scale used in right column plots.

According to Figure 5.15, it is observed that, at the vicinity of the sharp leading edge of the flat-plate, translational temperature is around fifty times the freestream temperature. As explained earlier, the large amount of kinetic energy present in a hypersonic freestream is converted by molecular collisions into high thermal energy surrounding the body. Inside the gaps, the translational temperature ratio reaches the wall temperature, i.e., the translational temperature T_T is four times the freestream temperature T_∞.
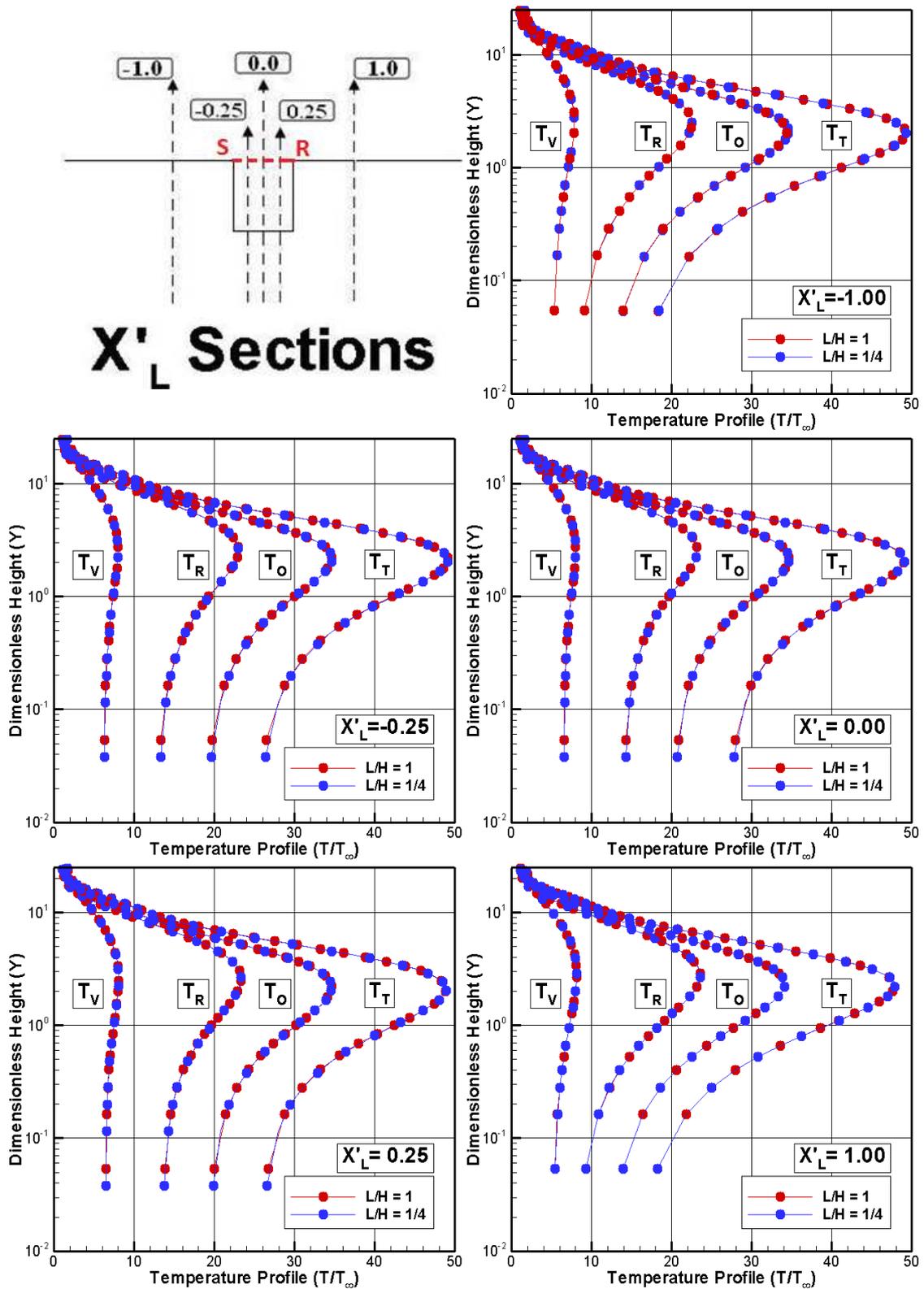
Figure 5.12 - Kinetic temperature ratio (T/T_∞) profiles for five sections outside the gap parameterized by the L/H ratio.

101
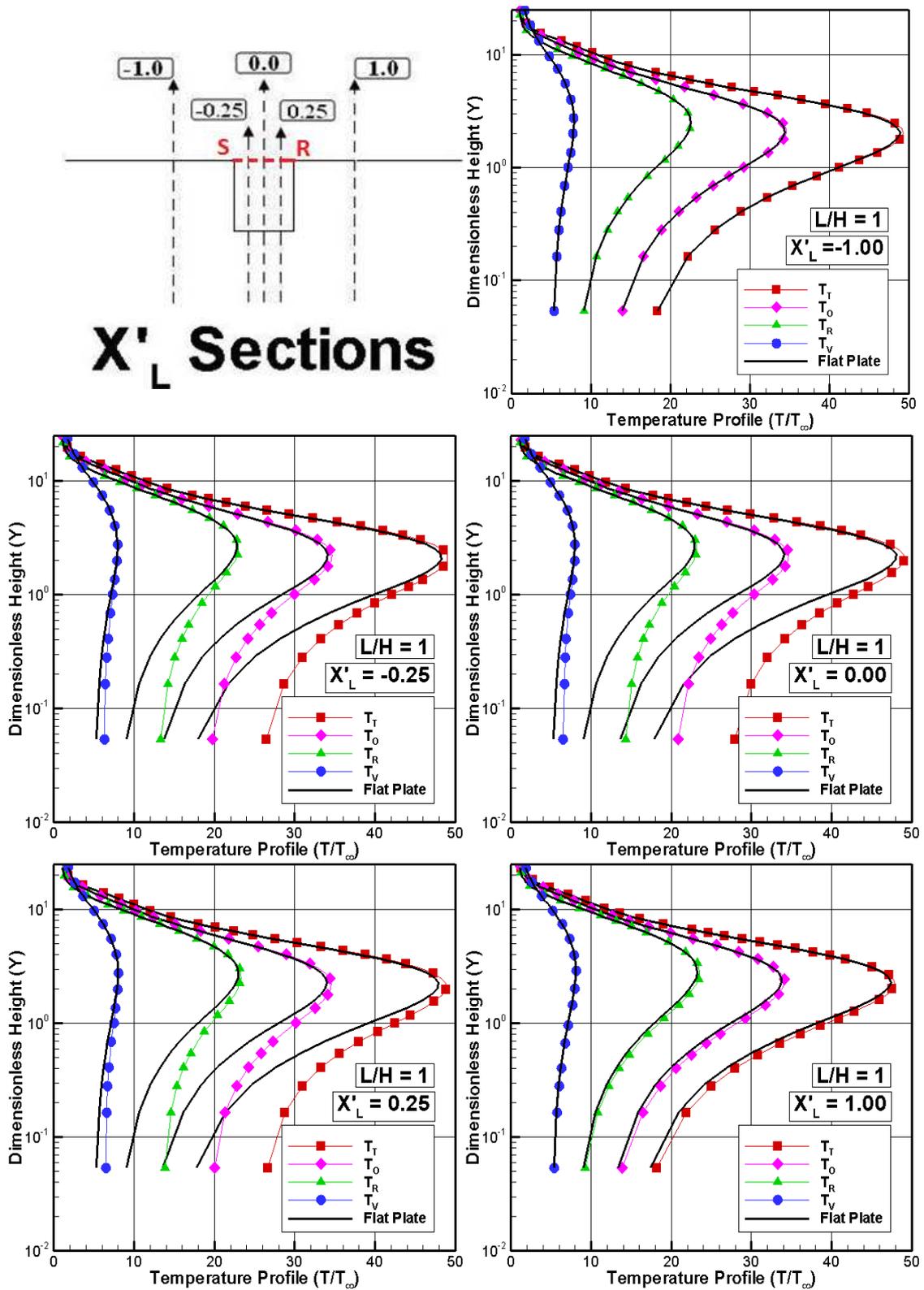
Figure 5.13 - Comparison of the kinetic temperature ratio (T/T_∞) profiles for the flat-plate and the gap defined by the $L/H = 1$.
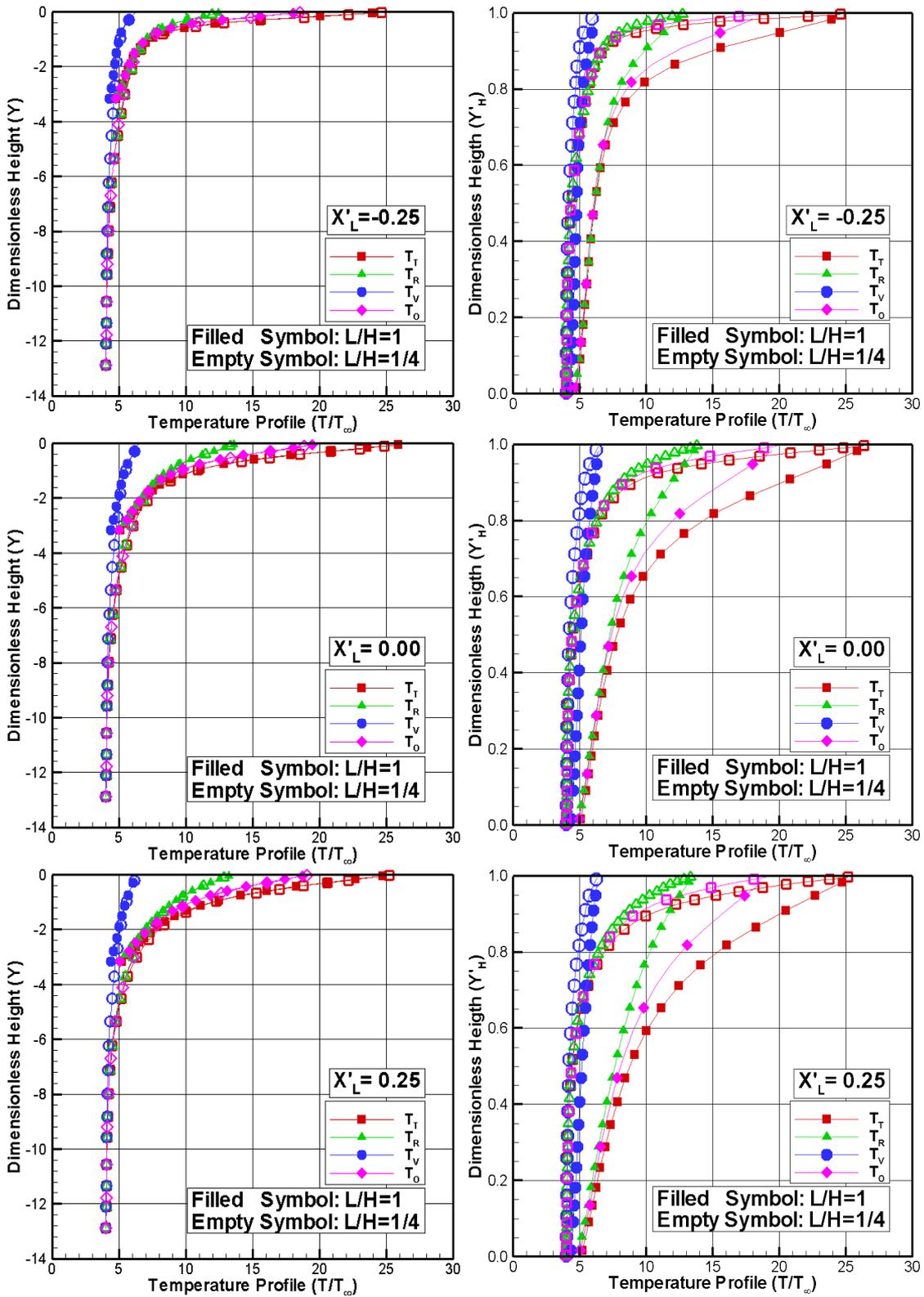
Figure 5.14 - Kinetic temperature ratio (T/T_∞) profiles for three sections inside the gap as a function of the dimensionless heights Y (left column) and Y'_H (right column).
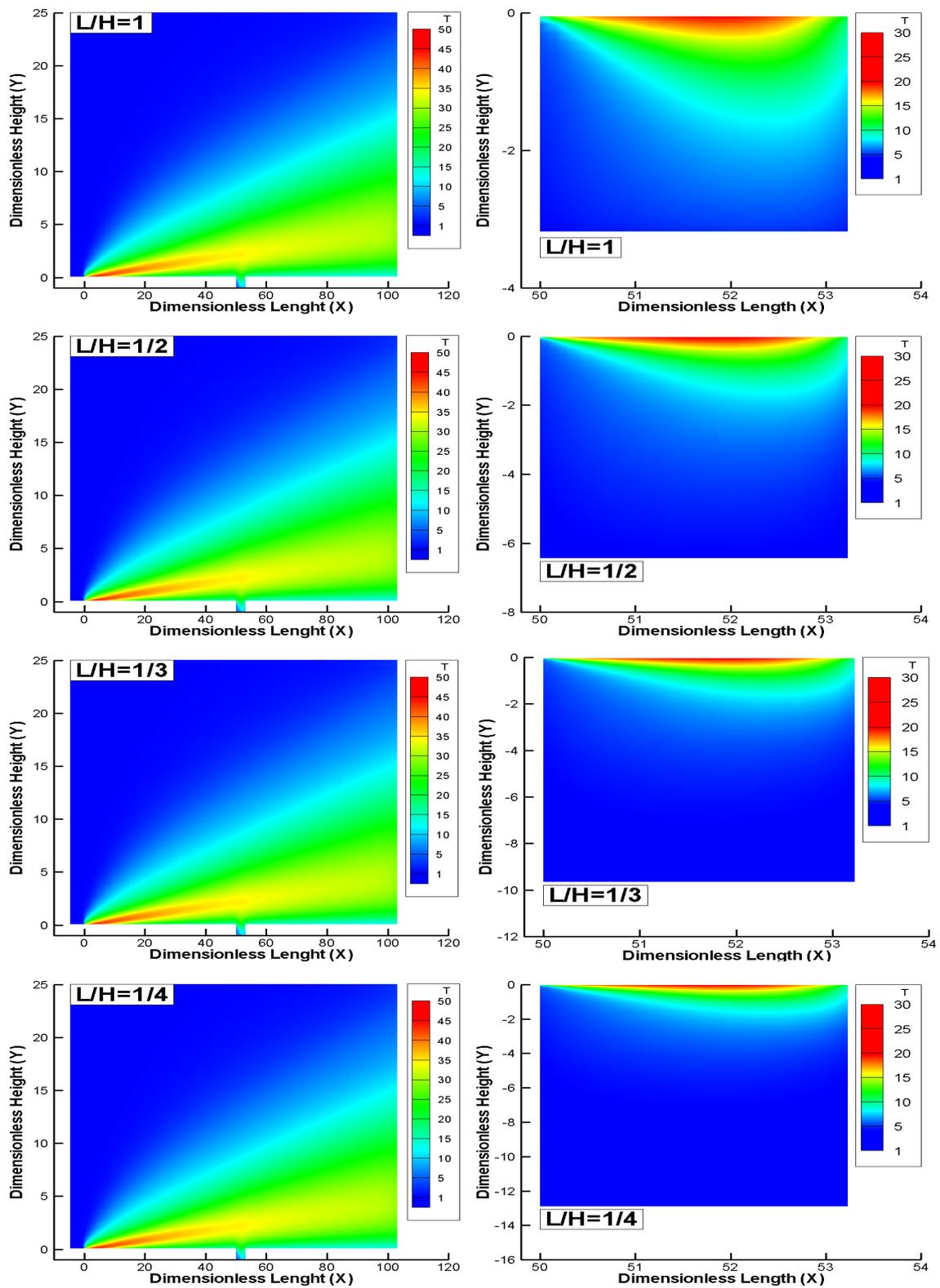
Figure 5.15 - Translational temperature ratio (T_T/T_∞) distribution outside (left) and inside (right) the gaps for *L/H* ratio of 1, 1/2, 1/3 and 1/4.

104

5.2   Aerodynamic Surface Quantities

Aerodynamic surface quantities of particular interest in the transition flow regime are number flux, pressure, heat flux, and shear stress. In this manner, the purpose of this section is to present and to discuss these quantities, expressed in coefficient form, due to variations in the gap L/H ratio.

5.2.1   Number Flux

The number flux N is calculated by sampling the molecules impinging on the gap surface by unit time and area. Effects of the L/H ratio on the number flux are illustrated in Figure 5.16. In this group of plots, N_f represents the number flux N normalized by $n_\infty U_\infty$, where n_∞ is the freestream number density and U_∞ is the freestream velocity. The left-column plots correspond to the number flux distribution along the gap upstream and downstream surfaces, i.e., surfaces S1 and S5, while the right-column plots refer to the distribution on the surfaces inside the gap, i.e., surfaces S2, S3, and S4. In addition, X is the length x normalized by the freestream mean free path λ_∞, and the dimensionless height Y'_H is the height $(y+H)$ normalized by the gap height H. Furthermore, for comparison purpose, the number flux distribution for the flat-plate case is also illustrated in this group of plots.

Examining first the left-column plots in Figure 5.16, it is clearly seen that the number flux behavior follows that presented by the flat-plate case for the L/H ratio investigated in this work, since no upstream disturb is caused by the gap presence. Along surface S5, no appreciable changes are observed in the number flux distribution. It is seen that N_f basically follows the same pattern of that presented by the flat-plate case. Nevertheless, attention should be paid to two interesting features. At the beginning of surface S5, the number flux is lower than that for the flat-plate case. Due to the flow expansion on the gap shoulder, density is low at the beginning of surface S5. As a result, number flux is low compared to that for the flat-plate case. In addition, a dramatically reduction in the

number flux is observed at the end of the surface S5. The reason for that is associated with the boundary conditions assumed for the outflow boundary, as explained in Chapter 3.

Turning next to the right-column plots in Figure 5.16, for the upstream face, surface S2, the dimensionless number flux is low at the top of the gap and increases gradually along the surface up to the corner at the bottom surface. Along the gap floor, surface S3, the number flux behavior also relies on L/H ratio. It is noticed that it increases with decreasing the L/H ratio. Nevertheless, it seems to reach a constant value for $L/H < 1/3$. Finally, along the downstream face, surface S4, N_f basically increases from the corner, at the bottom surface, up to the top of the gap. This behavior is in contrast to that observed for the upstream face. In fact, this is an expected behavior in the sense that it is directly related to the flow recirculation pointed out earlier. Due to the clockwise flow recirculation, at the vicinity of the surface S4, density is higher than that close to the surface S2. Therefore, a larger flux of molecules colliding to this surface is expected.
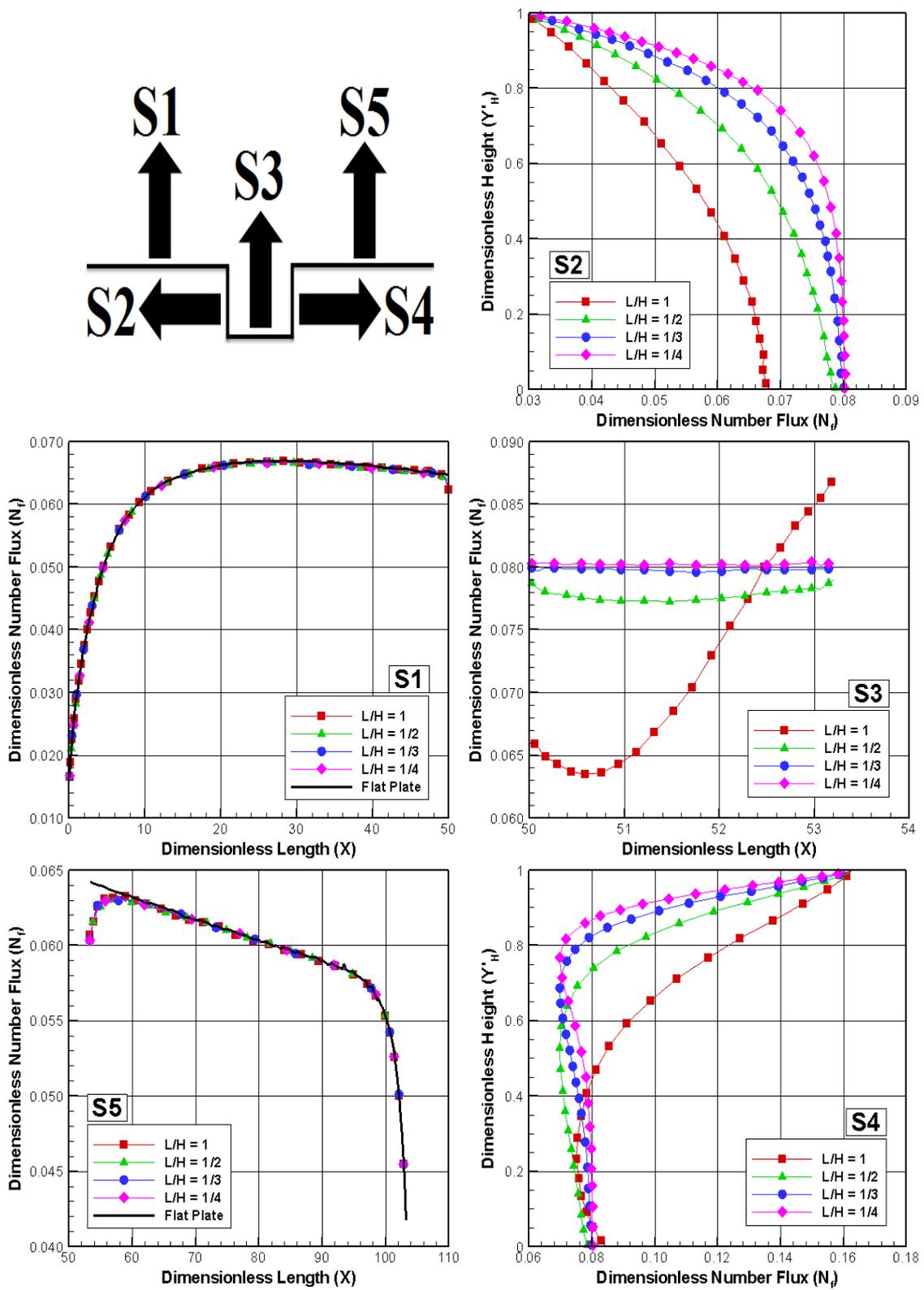
Figure 5.16 - Dimensionless number flux (N_f) distribution along the gap surfaces as a function of the *L/H* ratio.

5.2.2 Heat Transfer Coefficient

The heat transfer coefficient C_h is defined as follows,

$$C_h = \frac{q_w}{\frac{1}{2}\rho_\infty U_\infty^3} \tag{5.8}$$

where the heat flux q_w to the body surface is calculated by the net energy flux of the molecules impinging on the surface.

A flux is regarded as positive if it is directed toward the body surface. The net heat flux q_w is related to the sum of the translational, rotational and vibrational energies of both incident and reflected molecules as defined by,

$$q_w = q_i + q_r = \frac{1}{A\Delta t}\sum_{j=1}^{N}\{[\frac{1}{2}m_j c_j^2 + e_{Rj} + e_{Vj}]_i + [\frac{1}{2}m_j c_j^2 + e_{Rj} + e_{Vj}]_r\} \tag{5.9}$$

where N is the number of molecules colliding with the gap surface by unit time and unit area, m is the mass of molecules, c is the velocity of the molecules, e_R and e_V stand for the rotational and vibrational energies, respectively. Subscripts i and r refer to incident and reflect molecules.

The *L/H* ratio effect on the heat transfer coefficient C_h is demonstrated in Figure 5.17. Again, the left-column plots refer to the heat transfer distribution along the gap surfaces S1 and S5, while the right-column plots stand for the distribution on the gap surfaces S2, S3, and S4. As a basis of comparison, the heat transfer coefficient distribution for the flat-plate case is also illustrated in this figure.

Looking first to the left-column plots, along surface S1, it is observed that the heat transfer coefficient C_h for the gaps is the same of that presented by the flat-plate case.

C_h is low at the leading edge, increases up to a peak value, $C_h = 0.029$ around section $X = 8$, and decreases downstream along the plate. Along surface S5, it is seen that the heat transfer coefficient C_h is slightly larger than that for the flat-plate case, especially at the vicinity of the downstream corner of the gaps, defined by the surface-S4/surface-S5 junction. However, as the flow moves downstream along the surface S5, the heat transfer coefficient C_h basically recovers the value obtained for the flat-plate case.

Turning next to the right-column plots, for the upstream face, surface S2, the heat transfer coefficient is high at the top of the gap and increases to a maximum value still close to the shoulder, surface-S1/surface-S2 junction. Afterwards, C_h drops off along the surface up to the corner at the bottom surface. Along the gap floor, surface S3, the heat transfer coefficient depends on the L/H ratio. It is noted that the behavior for the $L/H = 1$ case differs from those cases defined by $L/H < 1$. While C_h increases up to a peak value close to the surface-S3/surface-S4 junction for the $L/H = 1$ case, C_h practically goes to zero for the cases defined by $L/H < 1$. It should be remarked in this context that, for $L/H < 1$ cases, the recirculation region does not reach the bottom of the gaps. Also, density is higher in this region. As a result, the molecular collision rate is larger compared to the other regions, and the flow comes to the thermal equilibrium and reaches the wall temperature, as shown in Figure 5.14.

Still referring to the right-column plots, along the downstream face, surface S4, the heat transfer coefficient increases monotonically from basically zero, at the surface-S3/surface-S4 junction, to the maximum value, $C_h \approx 0.054$, at the vicinity of the suface-S4/surface-S5 junction. It is very encouraging to observe that the heat transfer coefficient C_h for the downstream face is roughly one order of magnitude larger than that for the bottom surface, and this is one order of magnitude larger than that for the upstream surface. This is explained by the fact that, at the vicinity of the upstream face, the flow experiences an expansion. In contrast, at the vicinity of the downstream face, the flow experiences a compression due to the recirculation region inside the gaps.

The heat flux to the gap surface was defined in terms of the incident and reflected flow properties, Equation 5.9, and based upon the gas-surface interaction model of fully accommodated, complete diffuse reemission. The diffuse model assumes that the molecules are reflected equally in all directions, quite independently of their incident speed and direction. Due to the diffuse reflection model, the reflected velocity of the molecules impinging on the gap surface is obtained from a Maxwellian distribution that takes into account for the temperature of the gap surface. In this fashion, according to Equation 5.9, not only the number of molecules impinging on the surface but also the wall temperature plays an important role on the reflected contribution to the net heat flux to the gap surface.

At this point it is worth taking a closer look at the heat transfer coefficient results. In order to do that, the peak value for the heat transfer coefficient, $C_h \approx 0.054$, at the surface-S4/surface-S5 junction, is compared to that predicted for a smooth surface, i.e., a flat plate without a gap. For the flat-plate case, $C_h \approx 0.029$ around section $X = 8$. Therefore, for the same freestream conditions, the peak value of C_h for the gaps is approximately twice of that for a smooth surface.
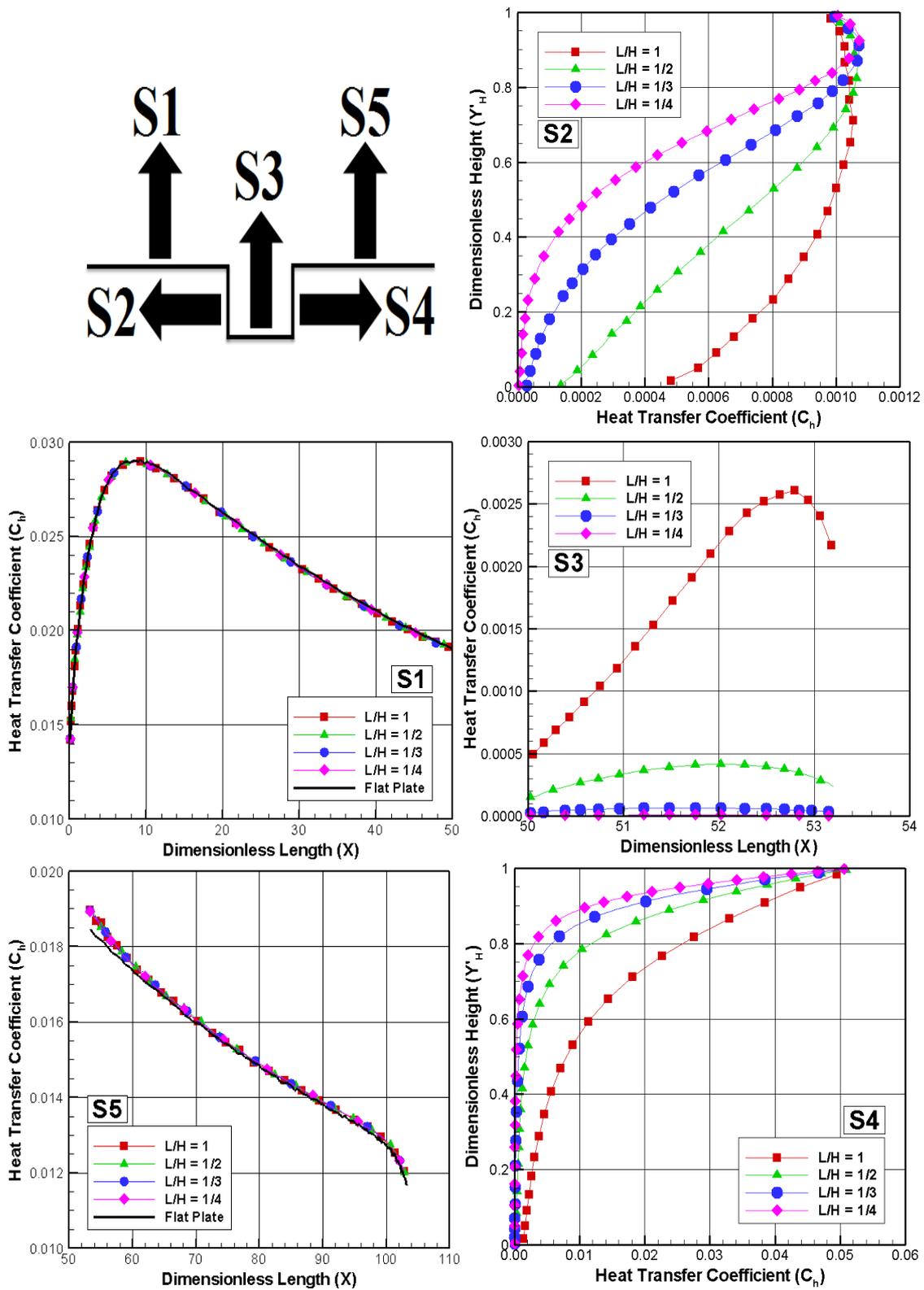
Figure 5.17 - Heat transfer coefficient (C_h) distribution along the gap surfaces as a function of the *L/H* ratio.

5.2.3   Pressure Coefficient

The pressure coefficient C_p is defined as follows,

$$C_p = \frac{p_w - p_\infty}{\frac{1}{2}\rho_\infty U_\infty^2} \tag{5.10}$$

where the pressure p_w on the gap surface is calculated by the sum of the normal momentum fluxes of both incident and reflected molecules at each time step by the following expression,

$$p_w = p_i + p_r = \frac{1}{A\Delta t}\sum_{j=1}^{N}\{[(mv)_j]_i + [(mv)_j]_r\} \tag{5.11}$$

where v is the velocity component of the molecule j in the surface normal direction.

The impact on the pressure coefficient C_p due to changes in the gap L/H ratio is displayed in Figure 5.18. Again, the left-column plots refer to the pressure coefficient distribution along the gap surfaces S1 and S5, while the right-column plots correspond to the distribution on the gap surfaces S2, S3, and S4. Referring to the left-column plots, it is clearly noticed that the pressure coefficient C_p follows the same trend as that presented for the dimensionless number flux in the sense that, along surface S1, the pressure coefficient presents the same behavior for the flat-plate case. Along surface S5, it is seen that the pressure coefficient C_p behavior is similar to that for the flat-plate case, except at the vicinity of the gap downstream corner, i.e., the surface-S4/surface-S5 junction. Near to this corner, a significant reduction in the pressure coefficient is observed when compared to the pressure coefficient for the flat-plate case. The reason for that is due to the flow expansion around this corner. Moreover, this pressure decrease is associated with the significant reduction in the number flux, as shown in Figure 5.16.

According to the right-column plots, it is seen that the pressure coefficient C_p basically follows a similar behavior as that presented by the number flux in the sense that, for the upstream face, surface S2, it is low at the shoulder, $Y'_H = 1$, and increases downward along the surface, reaching the maximum value at the bottom, station $Y'_H = 0$. In what follows, for the gap floor, surface S3, the pressure coefficient distribution relies on the gap L/H ratio. For the $L/H = 1$ case, C_p increases along the surface, and reaches the maximum value at the vicinity of the surface-S3/surface-S4 junction. Nevertheless, for $L/H < 1$ cases, the pressure coefficient is constant along the surface. Finally, along the downstream face, surface S4, the pressure coefficient behavior is in contrast to that observed along the surface S2 in the sense that C_p presents the lower value at the station $Y'_H = 0$, and increases monotonically upward along the surface, reaching the peak value at the shoulder, $Y'_H = 1$. It may be inferred in passing that this is an expected behavior since the flow within the gap is characterized by the appearance of a recirculation region. According to the flow topology, Figure 5.4, the streamline pattern shows that the flow is characterized by a primary vortex system for L/H ratio investigated, where a clockwise recirculation structure fills the entire gap for the $L/H = 1$ case. Conversely, for the $L/H < 1$ cases, the recirculation region does not reach the gap floor, surface S3.

For the present, it proves instructive to compare the maximum values for the pressure coefficient observed in the gaps with that for a smooth surface, i.e., a flat plate without a gap. As a basis of comparison, for the cases L/H of 1, 1/2, 1/3 and 1/4, the pick values for C_p is around 0.150 observed at the gap corner, surface-S4/surface-S5 junction, for all cases. Based on Figure 5.18, for the flat-plate case, the maximum value for C_p is around to 0.0392 at a station $23.9\lambda_\infty$ from the leading edge, along surface S1. Therefore, the C_p peak value for the gaps is around 3.8 times larger than the peak value for a smooth surface.
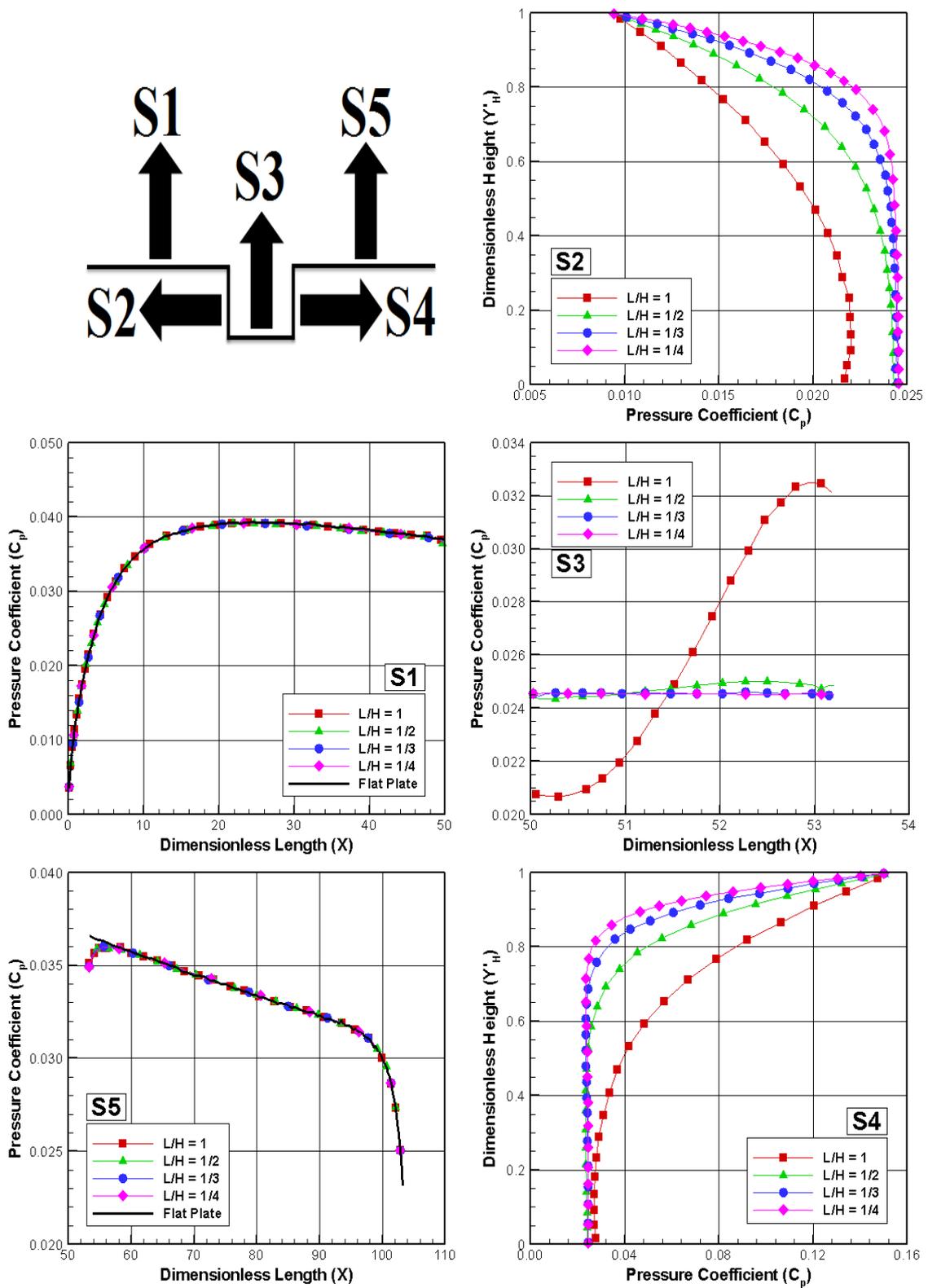
Figure 5.18 - Pressure coefficient (C_p) distribution along the gap surfaces as a function of the *L/H* ratio.

114

5.2.4 Skin Friction Coefficient

The skin friction coefficient c_f is defined as follows,

$$c_f = \frac{\tau_w}{\frac{1}{2}\rho_\infty U_\infty^2} \qquad (5.12)$$

Where the shear stress τ_w on the body surface is calculated by the sum of the tangential momentum fluxes of both incident and reflected molecules impinging on the surface at each time step by following expression,

$$\tau_w = \tau_i + \tau_r = \frac{1}{A\Delta t}\sum_{j=1}^{N}\{[(mu)_j]_i + [(mu)_j]_r\} \qquad (5.13)$$

where u is the velocity component of the molecule j in the surface tangential direction.

It is important to note that for the special case of diffuse reflection, the gas-surface interaction model adopted in present work, the reflected molecules have a tangential moment equal to zero, since the molecules essentially lose, on average, their tangential velocity components. In this fashion, the net tangential momentum flux is defined as follows,

$$\tau_w = \tau_i = \frac{1}{A\Delta t}\sum_{j=1}^{N}\{[(mu)_j]_i\} \qquad (5.14)$$

The effect of the gap L/H ratio on the skin friction coefficient C_f is depicted in Figure 5.19. According to the left-column plots in this figure, it is noted that the skin friction coefficient C_f follows a similar behavior of that presented by the heat transfer coefficient C_h. Along surface S1, it is seen that C_f reproduces the skin friction distribution for the flat-plate case. Along surface S5, similar to the heat transfer

coefficient, it is noticed that the skin friction coefficient C_f is larger than that for the flat-plate case, especially at the vicinity of the gap downstream corner, defined by the surface-S4/surface-S5 junction. Nevertheless, as the flow moves downstream along the surface S5, the skin friction coefficient C_f reaches the value observed for the flat-plate case. Finally, it should be mentioned that the peak values for the skin friction coefficient along surfaces S1 and S5 are larger than those observed for the pressure coefficient. As a result, tangential forces, associated with the shear stress, are larger than normal forces, related to the wall pressure.

Turning to the right-column plots in Fig. 5.19, for the upstream face, surface S2, the skin friction coefficient in general presents the peak value at the shoulder, $Y'_H = 1$, decreases along the upper half part of the surface, and basically reaches a negative constant value along the lower half part of the surface. In what follows, for the gap floor, surface S3, the skin friction coefficient is negative near the vicinity of the surface-S2/surface-S3 junction, and becomes positive at the vicinity of the surface-S3/surface-S4 junction. Nevertheless, as the L/H ratio increases, $C_f = 0$ is observed along the entire surface. Finally, along the downstream face, surface S4, the skin friction coefficient starts from zero at the vicinity of the surface-S3/surface-S4 junction and decreases negatively up to the minimum value at the shoulder, $Y'_H = 1$.

Usually, as C_f changes from positive to negative value, the condition $C_f = 0$ may indicate the presence of a backflow, an attachment or reattachment point in the flow. In the present account, these changes are directly related to the clockwise recirculation region inside the gaps. For the *L/H* ratios investigated, the flowfield structure inside the gaps was defined by only one vortex system. This is in contrast to the gap flowfield structure usually observed in the continuum flow regime. In this flow regime, the gap flow topology is defined by the development of a column of counter-rotating vortices within the gap caused by the main stream flow, where the number of vortices is approximately given by *H/L*. In addition, alternating hot spots are developed in the gap

116

when the vortices directionally align and impinge on the gap sidewall (EVERHART et al., 2006).
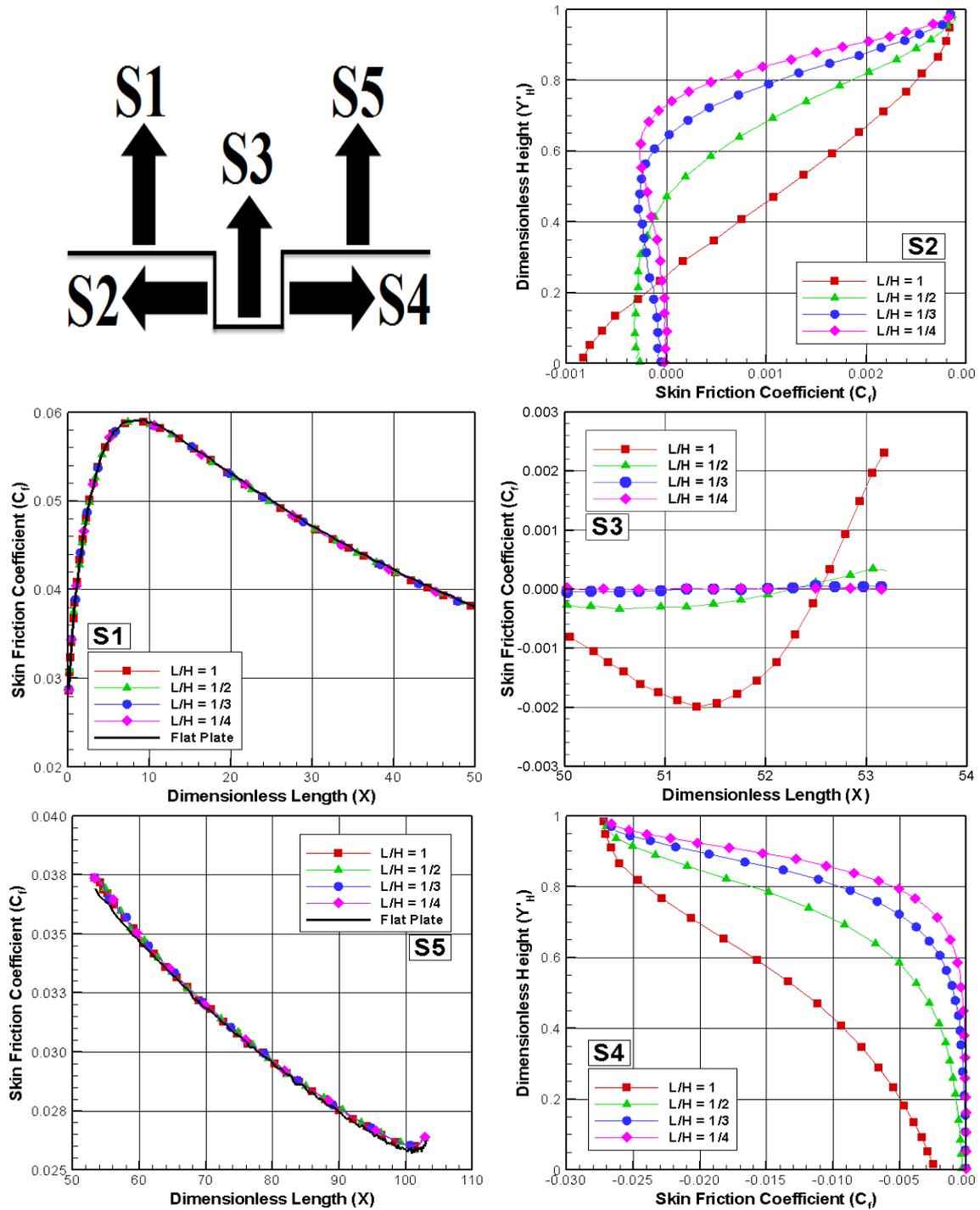
Figure 5.19 - Skin friction coefficient (C_f) distribution along the gap surfaces as a function of the L/H ratio.

6. CONCLUSIONS

6.1 Concluding Remarks

This study applies the Direct Simulation Monte Carlo (DSMC) method in order to investigate the flowfield structure and the aerodynamic surface quantities on hypersonic gap flow. The calculations provided information concerning the nature of the flow on gaps resulting from variations in the length-to-depth (*L/H*) ratio for the idealized situation of two-dimensional rarefied hypersonic flow. A very detailed description of the flowfield properties, such as velocity, density, pressure, and temperature, and aerodynamic surface quantities, such as number flux, heat transfer, pressure and skin friction, were presented separately outside and inside the gaps by a numerical method that properly accounts for non-equilibrium effects. Performance results for gaps, defined by *L/H* ratio of 1, 1/2, 1/3, and 1/4, were compared to those of a flat plate without gaps.

It was observed that the gap *L/H* ratio did not disturbed the flowfield far upstream and far downstream, as compared to the freestream mean free path, and the domain of influence along the upstream and downstream surfaces did not increased with increasing the *L/H* ratio.

One of the main findings of this research is related to the flow topology inside the gaps. The analysis showed that the recirculation region inside the gaps is a function of the *L/H* ratio. It was found that, for the *L/H* = 1 and 1/2 cases, the flow structure was characterized by a primary vortex system, with the recirculation region filling the entire gaps. For the *L/H* = 1/3 and 1/4 cases, it was observed that the recirculation region does not fill the entire gaps. In addition, as expected, the external stream does not reattach the bottom surface of the gaps. Moreover, it should be mentioned that the gap flow topology observed here in a rarefied environment differs from that usually observed in the continuum flow regime, as showed in Chapter 1.

119

Another issue that stimulated this study was the heat flux and pressure acting on the gap surfaces. Results showed that both depended on the *L/H* ratio. It was found that the peak values for the heat transfer coefficient C_h took place on the gap frontal face, and they were twice of the maximum value observed for a smooth surface, i.e., a flat plate without a gap. A similar behavior was found for the pressure loads. The peak value for the pressure coefficient C_p occurred at the gap frontal face, and it was around 3.8 times larger than the peak value for a smooth surface.

6.2   Future Work

The present work has described an initial investigation of a hypersonic rarefied flow over gaps in order to simulate discontinuities present on the surface of hypersonic space vehicles. Although this investigation has taken into account a representative range for the *L/H* ratio, a number of improvements to a realistic investigation on surface discontinuities is still desirable.

First on the list is to incorporate a new model for the gas-surface interaction. The diffuse reflection model employed in this research assumes that the molecules are reflected equally in all directions, quite independently of their incident speed and direction. Nevertheless, as a space flight vehicle is exposed to a rarefied environment over a considerable time, a departure from the fully diffuse model is observed, resulting from the colliding molecules that clean the surface of the vehicle, which becomes gradually decontaminated. Molecules reflected from clean surfaces show lobular distribution in direction. In this scenario, incomplete surface accommodation effects might provide more insight into the sensitivity of the aerothermodynamic surface quantities to gas-surface model.

The DSMC method has been used to assess the flowfield structure on gaps by considering constant wall temperature. In a realistic design, temperature not only

120

changes along the body surface but also inside the gaps. In this context, a more detailed analysis that includes the conjugate heat transfer problem seems to be challenge.

Finally, the Mach number effect, the angle-of-attack effect as well as the geometrical effect, i.e., the axisymmetric gap, might be included in this list.

REFERENCES

ABE, T. Rarefied gas flow analysis by direct simulation Monte Carlo method in body-fitted coordinate system. **Journal of Computational Physics**, v. 83, p. 424-432, 1989. 45

ABE, T. Generalized scheme of the no-time-counter scheme for the DSMC in rarefied gas flow analysis. **Computers Fluids**, v. 22, n. 2-3, p. 253-257, 1993. 23,27

ALDER, B. J.; WAINWRIGHT, T. E. Studies in molecular dynamics. **Journal of Chemical Physics**, v. 27, p. 1208-1209, 1957. 16

ALDER, B. J.; WAINWRIGHT, T. E. Molecular dynamics by electronic computers. In: PROGOGINE , I. (ed.). **Transport processes in statistical mechanics**. New York: Interscience, 1958. p. 97-131. 16

ALEXANDER, F. J.; GARCIA, A. J.; ALDER, B. J. A consistent Boltzmann algorithm. **Physical Review Letter**, v. 74, n. 26, p. 5212-5215, 1995. 17

ALEXANDER, F. J.; GARCIA, A. J.; ALDER, B. J. Cell size dependence of transport coefficients in stochastic particle algorithms. **Physics of Fluids**, v. 10, n. 6, p. 1540-1542, 1998. 19

ALEXANDER, F. J.; GARCIA, A. J.; ALDER, B. J. Erratum: Cell size dependence of transport coefficients in stochastic particle algorithms, **Physics of Fluids**, v. 12, n. 3, 731, 2000. 19,47

ANDERSON JR., J. D., In: MCGRAW-HILL. **Hypersonic and high temperature gas dynamics**. New York, 1989. 4

BECKER, M.; ROBBEN, F.; CATTOLICA, R. Velocity distribution function near the leading edge of a flat-plate. **AIAA Journal**, v. 12, n. 9, p. 1247-1253, 1974. 48, 57

BERTIN, J. J.; CUMMINGS, R. M. Critical hypersonic aerothermodynamic phenomena. **Annual Review of Fluid Mechanics**, v. 38, pp. 129-157, 2006. 3

BERTIN, J. J.; GOODRICH, W. D. Aerodynamic heating for gaps in laminar and transitional boundary layers. In: AIAA AEROSPACE SCIENCES MEETING AND EXHIBIT, 18., 1980, Pasadena. **Proceedings…** Pasadena: AIAA, 1980. 7, 10

BERTRAN, M. H.; WEINSTEIN, L. M.; CARY JR., A. M.; ARRINGTON, J. P. Heat transfer to wavy wall in hypersonic flow. **AIAA Journal**, v. 5, n. 10, pp. 1760-1767, 1967. 7

BERTRAM, M. H.; WIGGS, M. M. Effect of surface distortions on the heat transfer to a wing at hypersonic speeds. **AIAA Journal**, v. 1, n. 6, p. 1313-1319, 1963. 7

BIRD, G.A. Direct simulation and the Boltzmann equation. **Physics of Fluids**, v. 13, n. 11, p. 2676, 1970. 17

BIRD, G. A. **Molecular gas dynamics**. Oxford: Clarendon Press, 1976. 17, 23, 27, 28

BIRD, G. A. Monte-Carlo simulation in an engineering context**.** In: RAREFIED GAS DYNAMICS INTERNATIONAL SYMPOSIUM, 12., 1981, Charlottesville, VA. **Proceedings…** New York: AIAA, 1981. v. 74 Part I, p. 239-255. 26

BIRD, G. A. Definition of mean free path for real gases. **Physics of Fluids**, v. 26, n. 11, p. 3222-3223, 1983. 41

BIRD, G. A. Direct simulation of high-vorticity gas flow. **Physics of Fluids**, v. 30, n. 2, p. 364-366, 1987. 18

BIRD, G. A. **Rarefied gas dynamics:** theoretical and computational techniques: Perception of numerical method in rarefied gas dynamics. Washington, DC: Eds. E.P.Muntz and D.P.Weaver and D.H.Capbell, Progress in Astronautics and Aeronautics, AIAA, v. 118, p. 374-395, 1989. 23, 27, 41

BIRD, G. A. **Molecular gas dynamics and the direct simulation of gas flows**. Oxford: Clarendon Press, 1994. 17, 19, 21, 26, 27, 28, 36, 40, 42, 46, 96

BIRD, G. A. **The DS2G program user's guide**. Australia: G.A.B. Consulting Pty Ltda: N.S.W Killara, 1999. 48

BOGDONOFF, S. M.; KEPLER, C. E. Separation of a supersonic turbulent boundary layer. **Journal of the Aeronautical Sciences**, v. 22, pp. 414-430, 1955. 7

BORGNAKKE, C.; LARSEN, P. Statistical collision model for Monte Carlo simulation of polyatomic gas mixture. **Journal of Computational Physics**, v.18, p. 405-420, 1975. 34, 41

BOYD, I. D. Analysis of rotational nonequilibrium in standing shock waves of nitrogen. **AIAA Journal**, v. 28, n.11, p. 1997-1999, 1990. 35

BOYD, I. D. Monte Carlo study of vibrational relaxation process. In: INTERNATIONAL SYMPOSIUM ON RAREFIED GAS DYNAMICS, 17., 1990, Aachen. **Proceedings…** Aachen, Germany, 1990. p. 792-799. 35

BOYD, I. D. Rotational and vibrational nonequilibrium effects in rarefied hypersonic flow. **Journal of Thermophysics and Heat Transfer**, v. 4, n. 4, p. 478-484, 1990. 35

BOYD, I. D. Rotational-translational energy transfer in rarefied nonequilibrium flows. **Physics of Fluids**, v. A2, n. 3, p. 447-452, 1990. 36

BOYD, I. D. Analysis of vibrational-translational energy transfer using the direct simulation Monte Carlo method. **Physics of Fluids**, v. A3, n. 7, p. 1785-1791, 1991. 36

BOYD, I. D.; CHEN, G.; CANDLER, G. V. Prediction failure of the continuum fluid equations in the transition hypersonic flows. **Physics of Fluids**, v. 7, n. 1, p. 210-219, 1995. 15

BURNETT, D. The distribution of molecular velocities and the mean motion in a non-uniform gas. **Proceedings of the London Mathematical Society**, v. 40, p. 382-435, 1936. 15

CERCIGNANI, C. **The Boltzmann Equation and its Applications.** Springer-Verlag, New York, 1988. 16, 40

CERCIGNANI, C.; FREZZOTTI, A. Numerical simulation of supersonic rarefied gas flows past a flat-plate: effects of the gas-surface interaction model on the flow field. In: E. P. Muntz, D. P. Weaver and D. H. Campbell (eds.). **Rarefied gas dynamics:** theoretical and computational techniques, progress in astronautics and aeronautics: [S.l.]: Amer Inst of Aeronautics, 1989. v. 118, p. 552-566. 49. 57, 64

CHAPMAN, S; COWLING, T. G. **The mathematical theory of non-uniform gases.** London: Cambridge University press, 1970. 15

CHARBONNIER, J.; BOERRIGTER, H. Contribution to the study of gap induced boundary layer transition in hypersonic flow. In: AIAA/DGLR INTERNATIONAL AEROSPACE PLANES AND HYPERSONICS TECHNOLOGIES CONFERENCE, 5., 1993, Munich. **Proceedings…** Munich: AIAA, 1993. 7

CHARWAT, A. F.; DEWEY, C. F.; ROOS, J. N; HITZ, J. A. An investigation of separated flows – part I: The pressure field. **Journal of Aerospace Sciences**, v. 28, n. 6, pp. 457-470, 1961. 7, 8

CHARWAT, A. F.; DEWEY, C. F.; ROOS, J. N; HITZ, J. A. An investigation of separated flows – part II: Flow in the cavity and heat transfer. **Journal of Aerospace Sciences,** v. 28, n. 7, pp. 513-527, 1961. 7, 8

CHEN, G.; BOYD, I. D. Statistical error analysis for the direct simulation Monte Carlo technique. **Journal of Computational Physics**, v. 126, p. 434-448, 1996. 19

CHENG, H. K.; EMMANUEL, G. Perspective on hypersonic nonequilibrium flows. **AIAA Journal**, v. 33, n. 3, p. 385-400, 1995. 16

CHEW Y. T.; SHU C.; MAO X. H. Particle number per cell and scaling factor effect on accuracy of DSMC simulation of micro flows. **International Journal of Numerical Methods of Heat & Fluid Flow**, v. 15, n. 8, p. 827-841, 2005. 19, 21

COMEAUX, K. A.; MACCORMACK, R. W.; CHAPMAN, D. R. An analysis of the Burnett equations based on the second law of thermodynamics. **33rd AIAA Aerospace Science Meeting and Exhibit**, AIAA pp. 95-0415, Reno, NV, January 9-12, 1995. 15, 16

CYBYK, B. Z.; ORAN, E. S.; BORIS, J. P.; ANDERSON JR., J. D. Combining the monotonic lagrangian grid with direct simulation Monte Carlo Model. **Journal of Computational Physics**, v. 122, p. 323-334, 1995. 23

DIETRICH, S. Efficient computation of particle movement in 3-d DSMC calculations on structured body-fitted grids. In: INTERNATIONAL SYMPOSIUM ON RAREFIED GAS DYNAMICS, 17., 1990, Aachen, Germany. **Proceedings…** Aachen, Germany: [s.n], 1990. p. 745-752. 21

DUNAVANT, J. C.; THROCKMORTON, D. A. Aerodynamic heat transfer to RSI tile surfaces and gap intersections. **Journal of Spacecraft and Rockets**, v. 11, pp. 437-440, 1974. 7

EMERY, A. F.; SADUNAS, J. A.; LOLL, M. Heat transfer and pressure distribution in open cavity flow. **Journal of Heat Transfer**, pp. 103-108, 1967. 7

EVERHART, J. L. Supersonic/Hypersonic laminar heating correlations for rectangular and impact-induced open and closed cavities. **Journal of Spacecraft and Rockets**, v. 46, n. 3, pp. 545-560, 2009. 7

EVERHART, J. L.; ALTER, S. J.; MERSKI, N. R.; WOOD, W. A. Pressure gradient effects on hypersonic flow heating. In: AIAA AEROSPACE SCIENCES MEETING AND EXHIBIT, 44., 2006, Reno, **Proceedings…** Reno, Nevada: AIAA, 2006. p. 2006-0185. 6, 7, 8, 39, 116

EVERHART, J. L.; GREENE, F. A. Turbulent supersonic/hypersonic heating correlations for open and closed cavities. **Journal of Spacecraft and Rockets**, v. 47, n. 4, pp. 545-553, 2010. 7

FALLAVOLLITA, M. A.; BAGANOFF, D.; MCDONALD, J. D. Reduction of simulation cost and error for particle simulations of rarefied flows. **Journal of Computational Physics**, v. 109, p. 30-36, 1993. 19, 47

FISCKO, K. A.; CHAPMAN, D. R. Hypersonic shock structure with Burnett terms in the viscous stress and heat transfer. In: AIAA THERMOPHYSICS, PLASMADYNAMICS AND LASERS CONFERENCE, 1988, San Antonio, texas. **Proceedings…** San Antonio: AIAA, 1988. p. 88-2733. 15

FISCKO, K. A.; CHAPMAN, D. R. Comparison of Burnett, Super-Burnett and Monte Carlo solutions for hypersonic shock structure. In: E. P. Muntz, D. P. Weaver; D. H. Capbell (eds.). **Rarefied gas dynamics:** theoretical and computational techniques. Washington, DC: AIAA, 1989. v. 118, p. 374-395. 15

GADD, G. E. A theoretical investigation of laminar separation in supersonic flow. **Journal of the Aeronautical Sciences**, v. 24, n. 10, pp. 759-784, 1957. 7

GAI, S.; MILTHORPE, J. F. Hypersonic high-enthalpy flow over a blunt-stepped cone. In: INTERNATIONAL SYMPOSIUM ON SHOCK WAVES, 20., 1995, Pasadena, CA. **Proceedings…** Pasadena, CA: [s.n], 1995**. v**. 1, p. 234-244. 6, 7, 39

GROTOWSKY, I. M. G.; BALLMANN, J. Numerical investigation of hypersonic step-flows. **Shock Waves**, v. 10, pp. 57-72, 2000. 7, 39

GUPTA, R. N.; SCOTT, C. D.; MOSS, J. N. Surface-slip equations for low Reynolds number multicomponent air flow. In: H. F. Nelson(ed.). **Rarefied gas dynamics:** thermal design of aeroassisted orbital transfer vehicles, progress in astronautics and aeronautics. New York: AIAA. 1985. v. 96, 465-490. 98

HAMMERSLEY, J.M.; HANDSCOMB, D.C. **Monte Carlo methods.** London: Chapman and Hall, 1979. 18

HARVEY, J. K. Direct simulation Monte Carlo method and comparison with experiment. In: J. N. Moss; C. D. Scott (eds.). **Rarefied gas dynamics:** thermophysical aspect of re-entry flows. Wasgington: aIAA, 1986. v. 103, p. 25-43. 18

HARVEY, J. K. A review of a validation exercise on the use of the DSMC method to compute viscous/inviscid interaction in hypersonic flow. In: AIAA THERMOPHYSICS CONFERENCE, 36., 2003, Orlando. **Proceedings…** AIAA, 2003. p. 2003-3643. 18

HARVEY, J. K.; GALLIS, M. A. Review of code validation studies in high-speed low-density flows. **Journal of Spacecraft and Rockets**, v. 37, n. 1, p. 8-20, 2000. 18

HASH, D. B.; MOSS, J. N.; HASSAN, H. A. Direct simulation of diatomic gases using the generalized hard sphere model**. Journal of Thermophysics and Heat Transfer**, v. 8, n. 4, p. 758-764, 1994. 27

HASH, D.B; HASSAN, H. A. Direct simulation with vibration-dissociation coupling. **Journal of Thermophysics and Heat Transfer**, v. 7, n. 4, p. 680-686, 1993. 36

HASSAN, H. A.; HASH, D. B. A generalized hard-sphere model for Monte Carlo simulation. **Physics of Fluids**, v. A5, n. 3, p. 738-744, 1993. 27

HAVILAND, J. K.; LAVIN, M. L. Application of Monte Carlo method to heat transfer in rarefied gases. **Physics of Fluids**, v. 5, p. 1399-1405, 1962. 16

HERMINA, W. L. Monte Carlo simulation of rarefied flow along a flat-plate. **Journal Thermophysics and Heat Transfer**, v. 3, n. 1, p. 7-12, 1989. 49, 57, 58, 64

HIGDON, J. J. L. Stokes flow in arbitrary two-dimensional domains: Shear flow over ridges and cavities. **Journal of Fluid Mechanics**, v. 159, pp. 195-226, 1985. 7

HINDERSKS, M.; RADESPIEL, R. Investigation of hypersonic gap flow of a reentry nosecap with consideration of fluid structure interaction. In: **AIAA Aerospace Sciences Meeting and Exhibit**, 44., 2006, Reno, NEVADA. **Proceedings…** Reno: AIAA, 2006. p. 2006-0188. 1, 7, 39

HINDERKS, M.; RADESPIEL, R.; GULHAN, A. Simulation of hypersonic gap flow with consideration of fluid structure interaction. In: AIAA FLUID DYNAMICS CONFERENCE AND EXHIBIT, 34., Portland, OR. **Proceedings…** Portland: AIAA, 2004. p. 2004–2238. 7, 10

HOLDEN M.S.; WADHAMS T. P. A review of experimental studies for DSMC and Navier-Stokes code validation in laminar regions of shock/shock and shock/boundary layer interaction including real gas effects in hypervelocity flows. In: AIAA Thermophysics Conference, 36., 2003, Orlando. **Proceedings…** Orlando: AIAA, 2003. p. 2003-3641. 17

HOZUMI, K.; KOYAMA, T.; HIRABAYASHI, N. Experimental study on hypersonic heating characteristics of cavity wake flow. In: International Congress of the Aeronautical Sciences, 24., 2004, Yokohama. **Proceedings…** Yokohama, 2004. 39

IVANNOV, M. S.; GIMELSHEIN, S. F. Computational hypersonic rarefied flows. **Annual Review of Fluid Mechanics**, v. 30, p. 469-505, 1998. 18

JACKSON, A. P.; HILLIER, R.; SOLTANI, S. Experimental and computational study of laminar cavity flows at hypersonic speeds. **Journal of Fluid Mechanics**, v. 427, p. 329-358, 2001. 7, 39

JAKUBOWSKI, A. K.; LEWIS, C. H. Experimental study of supersonic laminar base flow with and without suction. **AIAA Journal**, v. 11, n. 12, p. 1670-1677, 1973. 7

KANNENBERG, K. C.; BOYD, I. Strategies for efficient particle resolution in the direct simulation Monte Carlo method. **Journal of Computational Physics**, v.157, p. 727-745, 2000. 47

KEON-YOUNG Y.; AGARWAL R. K.; BALAKRISHNAN R. Beyond Navier-Stokes: Burnett equations for flows in the continuum-transition regime. **Physics of Fluids**, v. 13, n. 10, p. 3061-3086, 2001. 15

KOURA, K. Null-Collision technique in the direct-simulation Monte Carlo method, **Physics of Fluids**, v. 29, n. 11, p. 3509-3511, 1986. 23

KOURA, K.; MATSUMOTO, H. Variable soft sphere molecular model for inverse-power-law of Lennard-Jones potential. **Physics of Fluids**, v. A3, n. 10, p. 2459-2465, 1991. 26

KOURA, K.; MATSUMOTO, H. Variable soft sphere molecular model for air species. **Physics of Fluids**, v. A4, n. 5, p. 1083-1085, 1992. 27

KUNC, J. A.; HASSAN, H. A.; HASH, D. B. The GHS interaction model for strong attractive potentials. **Physics of Fluids**, v. 7, n. 3, p. 1173-1175, 1995. 26

LAUX, M. Optimization and parallelization of the DSMC method on unstructured grids. In: AIAA THERMOPHYSICS CONFERENCE, 32., 1997, Atlanta. Proceedingd… Atlanta: AIAA, 1997. p. 97-2512. 21

LEE, C. J. Unique determination of solutions to the Burnett equations. **AIAA Journal**, v. 32, n. 5, p. 985-990, 1994. 15

LIU, N.; YIN-KWEE NG, E. The impacts of the-step size in the application of the direct simulation Monte Carlo method to ultra thin gas film lubrication. **Journal of Micromechanics and Microengineering**, v. 12, p. 567-573, 2002. 20

LORD, R. Application of the Cercignani-Lampis scattering kernel to direct simulation Monte Carlo method. In: INT. SYMPOSIUM ON RAREFIED GAS DYNAMICS, 17., 1991, Aachen. **Proceeedings…** Aachen, Germany, 1991. p. 1427-1433. 38

LORD, R. Rarefied gas dynamics: space science and engineering, progress in astronautics and aeronautics: In: B. D. Shizgal; D. P. Weaver (eds.). **Direct simulation of rarefied hypersonic flow over a flat-plate with incomplete surface accommodation**. Oxford: University Press, 1994. v. 160, p. 221-228. 38, 49, 57, 62, 65

LUMPKIN III, F. E.; CHAPMAN, D. R. Accuracy of the Burnett equations for hypersonic real gas flows. **Journal of Thermophysics and Heat Transfer**, v. 6, n. 3, p. 419-425, 1992. 15

LUMPKIN III, F. E.; HAAS, B. L.; BOYD, I. D. Resolution of differences between collision number definitions in particle and continuum simulations. **Physics of Fluids**, v. A3, n. 9, p. 2282-2284, 1991. 35

MAZAHERI, A.; WOOD, W. A., Heating augmentation for short hypersonic protuberances. **Journal of Spacecraft and Rockets**, v. 46, n. 2, pp. 284-291, 2009. 7

MEIBURG, E. Comparison of the molecular dynamics method and the direct simulation Monte Carlo technique for flows around simple geometries. **Physics of Fluids**, v. 29, n. 10**,** p. 3107-3113, 1986. 18

MORGENSTERN JR., A.; CCHOKANI, N. Hypersonic flow past open cavities, **AIAA Journal**, v. 32, n. 12, pp. 2387-2393, 1994. 7

MOSS, J. N.; PRICE, J. M.; DOGRA, V. K.; HASH, D. B. Comparison of DSMC and experimental results for hypersonic external flows. IN: AIAA THERMOPHYSICS CONFERENCE, 30., 1995, San Diego. **Proceedings…** San Diego: AIAA, p. 95-2028. 17

NANBU, K. **Rarefied gas dynamics:** theoretical basis of the direct simulation Monte Carlo method. Stuttgard, Germany: Eds. V. Boffi and C. Cercignani, v. 1, p. 369-383, 1986. 23, 27

NANCE, R. P.; WILMOTH, R. G.; HASSAN, H. A. Comparison of grid-definition schemes for Monte Carlo simulations. **Journal of Thermophysics and Heat Transfer**, v. 11, n. 2, p. 296-303, 1997. 21, 46

NESTLER, D. E., An experimental study of hypersonic cavity flow. **Journal of Spacecraft and Rockets**, v. 19, n. 3, p. 195-196, 1982. 7

NESTLER, D. E.; SAYDAH, A. R.; AUXER, W. L. Heat transfer to steps and cavities in hypersonic turbulent flow. **AIAA Journal**, v. 7, n. 7, p. 1368-1370, 1969. 7

OLYNICK, D. P.; MOSS, J. N.; HASSAN, H. A. Grid generation and adaptation for the direct simulation Monte Carlo method. **Journal of Thermophysics and Heat Transfer**, v. 3, n. 4, p. 368-373, 1989. 45

PALMER, G. E.; PULSONETTI, M.; WOOD, W. A.; ALTER, S.; GNOFFO, P.; TANG, C. Computational assessment of thermal protection system damage experienced during STS-118. **Journal of Spacecraft and Rockets**, v. 46, n. 6, p. 1110-1116, 2009. 3

PETLEY, D. H.; SMITH, D. M.; EDWARDS, C. L. W.; CARLSON, A. B.; HAMILTON II, H. H. Surface step induced gap heating in the shuttle thermal protection system. **Journal of Spacecraft and Rockets**, v. 11, n. 2, p. 156–161, 1984. 7

PITTS, W. C.; MURBACH, M. S. Flight measurements of tile gap heating on the space shuttle. AIAA/ASME 3rd Joint Thermophysics, **Fluids, Plasma and Heat Transfer Conference**, AIAA pp. 82–0840, St. Louis, MO, 1982. 7

PULLIN, D. I.; HARVEY, J. K., Direct simulation calculations of the rarefied flow past a forward-facing step. **AIAA Journal**, v. 15, n. 1, p. 124–126, 1977. 7

RAULT, D. F. G. Aerodynamic of the shuttle orbiter at high altitude. **Journal of Spacecraft and Rockets**, v. 31, n. 6, p. 944-952, 1994. 45

RIEFFEL, M. A. A method for estimating the computational requirements of DSMC simulations. **Journal of Computational Physics**, v. 149, p. 95-113, 1999. 47

ROM, J.; SEGINER, A. Laminar heat transfer to a two-dimensional backward facing step from the high-enthalpy supersonic flow in the shock tube. **AIAA Journal**, v. 2, n. 2, p. 251-255, 1964. 7

SCOTT, C. D.; MARAIA, R. J. Gap heating with pressure gradients. In: AIAA THERMOPHYSICS CONFERENCE, 14., 1979, Orlando. **Proceedings…** Orlando: AIAA, 1979. p. 79–1043. 1, 7, 9

SMITH, D. M.; PETLEY, D. N.; EDWARDS, C. L. W.; PATTEN, A. B. An investigation of gap heating due to stepped tiles in zero pressure gradient regions of the Shuttle orbiter thermal protection system. In: AIAA AEROSPACE SCIENCES MEETING AND EXHIBIT, 21., Reno, Nevada. **Proceedings… Reno:** AIAA, 1983. p. 83-0120. 7

TANNEHILL, J. C.; EISLER, G. R. Numerical computation of the hypersonic leading edge problem using the Burnett equations. **Physics of Fluids**, v. 19, n. 1, p. 09-15, 1976. 15

TRAINEAU, J.C.; THIVET, F.; GULHAN, A.; COSSON, E.; SMITH, A.; MARRAFFA, L. Synthesis of the gap heating analysis of the hyflex flight. In: EUROPEAN SYMPOSIUM ON AEROTHERMODYNAMICS FOR SPACE VEHICLES, 5., 2005, Cologne. **Proceedings…** Cologne, 2005. 7, 10

WAGNER, W. A Convergence proof for Bird's direct simulation Monte Carlo method for the Boltzmann equation. **Journal of Statistical Physics**, v. 66, n. 3-4, p. 1011-1045, 1992. 17

WILMOTH, R. G.; LEBEAU, G. J.; CARLSON, A. B. DSMC grid methodologies for computing low-density, hypersonic flows about reusable launch vehicles. **31st AIAA Thermophysics Conference**, AIAA pp. 96-1812, New Orleans, Lousiana, June 17-20 1996. 21, 46

YEN, S. M. Monte Carlo solutions of nonlinear Boltzmann equation for problems of heat transfer in rarefied gases. **Int. J. of Heat and Mass Transfer**, v. 14, p. 1865-1869, 1971. 17

YEN, S. M. Numerical solution of the nonlinear Boltzmann equation for nonequilibrium gas flow problems. **Annual Review of Fluid Mechanics**, v. 16, p. 67-97, 1984. 17

ZHONG, X.; MCCORMACK, R. W.; CHAPMAN, D. R. Stabilization of the Burnett equations and application to hypersonic flows. **AIAA Journal**, v. 31, n. 6, p. 1036-1043, 1993. 15